NTNU – Trondheim
Norwegian University of
Science and Technology

Design of an experimental setup for measurements of the aerodynamic properties of bridge decks

Lars Halvor Kaasa

Master of Science in Engineering and ICT
Submission date: June 2012
Supervisor: Ole Andre Øiseth, KT
Co-supervisor: Ragnar Sigbjørnsson, KT

Norwegian University of Science and Technology
Department of Structural Engineering

NTNU
Institutt for konstruksjonsteknikk

Masteroppgave våren 2012 for stud. techn. Lars Halvor Kaasa:

Utvikling av en rigg for måling av aerodynamiske egenskaper til brokonstruksjoner

Design of an experimental setup for measurements of the aerodynamic properties of bridge decks

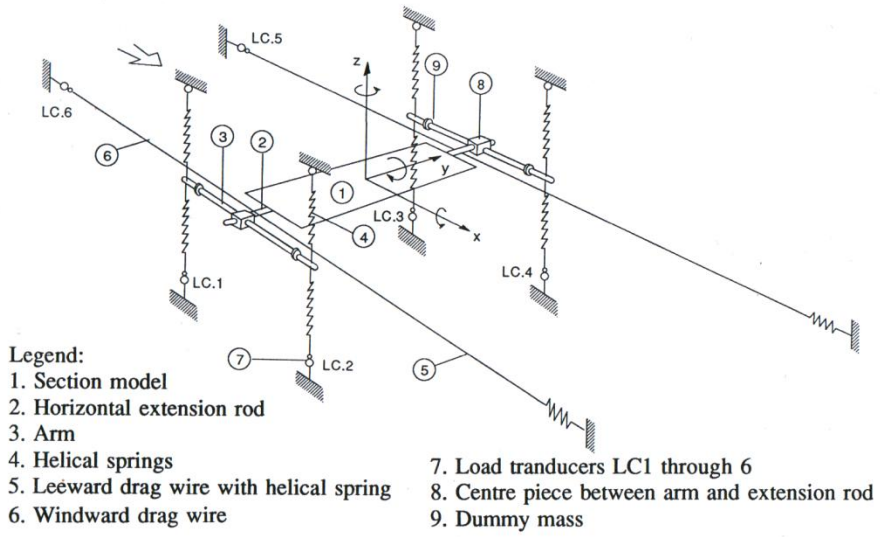

Figur: E. Hjorth-Hansen (1992). Section model tests. Aerodynamics of large bridges.

Statens vegvesen planlegger en ombygning av E39 slik at det blir mulig å reise fra Trondheim til Kristiansand ferjefritt. Dette innebærer at det skal bygges en rekke brokonstruksjoner. Enkelte av disse vil bli meget slanke slik at vindindusert dynamisk respons blir en sentral del av prosjekteringen. For å bestemme de aerodynamiske egenskapene til brokonstruksjoner er det vanlig å teste en seksjonsmodell i en vindtunnel. Seksjonsmodellen kan som oftest bevege seg vertikalt og vri seg langs broaksen. Når brokonstruksjonene blir ekstremt lange kan også horisontalbevegelsen bli viktig i bestemmelsen av de aerodynamiske deriverte. Det er derfor ønskelig at det utvikles en rigg som også tillater horisontal bevegelse.

Oppgavens formål er å:

- Utvikle en rigg som har en horisontal-, vertikal- og torsjonsfrihetsgrad.
- Teste riggen og bestemme dens dynamiske egenskaper ved hjelp av systemidentifikasjon

Løsningen av oppgaven bør inneholde følgende:

- abaqus modell av riggen med en seksjonsmodell.
- Grunnleggende teori om systemidentifikasjon.
- Bestemmelse av lengden på strengene for å minimalisere ikke-lineære effekter.
- Bestemme masse og fjærstivheter slik at svingeformene blir lette å identifisere.
- Målinger på riggen i laboratoriet for å verifisere dens egenskaper ved hjelp av systemidentifikasjon.

Oppgaven skal utføres i henhold til retningslinjer for utførelse av prosjektoppgave ved institutt for konstruksjonsteknikk (se instituttets hjemmeside).

Faglærer: Ole Andre Øiseth

Veiledere: Ragnar Sigbjörnsson

Besvarelsen skal leveres til Institutt for konstruksjonsteknikk innen 11. juni 2012.

Ole Andre Øiseth
Faglærer

Sammendrag

Ettersom moderne brodesign sikter mot lenger og slankere broer, er det nødvendig å kunne bestemme de aerodynamiske egenskapene til slike konstruksjoner med stor nøyaktighet. Den horisontale frihetsgraden har tradisjonelt sett blitt ansett som uinteressant, og aerodynamiske egenskaper har blitt bestemt ved seksjonsmodelltester som kun involverer en vertikal og en torsjonal frihetsgrad. Likevel, for veldig lange broer kan det vise seg at den horisontale frihetsgraden utgjør en forskjell.

Denne oppgaven tar for seg en rigg basert på den tradisjonelle opphengsriggen, men som i tillegg til vertikal og torsjonal bevegelse også tillater horisontal bevegelse. En prototype beregnet for eksperimenter i stille luft har blitt designet, bygd og testet.

Ved å introdusere en horisontal frihetsgrad blir stivheten til systemet ikke-lineær med hensyn på bevegelse av seksjonsmodellen. For å bedre forstå modellens oppførsel i riggen, har det blitt utviklet en element-modell og en analytisk stivhetsmodell.

To typer systemidentifikasjonsmetoder ble brukt for å bestemme de dynamiske egenskapene til prototypen. *Covariance Block Hankel Matrix* (CBHM)-metoden har tidligere blitt brukt til å bestemme aerodynamiske egenskaper til flere kjente broer, blant annet Hardangerbrua, mens *Subspace State Space System Identification* (N4SID)-metoder er en nyere type metoder som er kjent for robusthet, nøyaktighet og enkelhet i bruk. Det viser seg at N4SID-metoden som er brukt i denne oppgaven gir langt bedre dempingsestimater enn CBHM-metoden.

Den foreslåtte riggen virker lovende for videre forskning og utvikling, selv om den har enkelte ulemper og begrensinger.

Abstract

As modern bridge design continuously aims for longer and slender bridges, it is necessary to be able to determine aerodynamic properties of such structures with a high degree of accuracy. The horizontal degree of freedom has traditionally been considered uninteresting, and aerodynamic properties have been determined by section model tests involving a vertical and a torsional degree of freedom only. However, for very long bridges, horizontal motion may prove to be important.

This thesis has focused on an experimental setup based on the traditional suspension rig, but in addition to vertical and torsional motion, it also allows horizontal motion. A prototype intended for still air experiments has been designed, built and tested.

Introducing a third degree of freedom renders the stiffness of the system non-linear with respect to motion of the section model. To better understand the model's behaviour in the rig, a FE-model and an analytical stiffness model have been developed.

Two types of system identification methods were utilised to determine the dynamic properties of the prototype. The *Covariance Block Hankel Matrix* (CBHM) method have over the years been used to determine aerodynamic properties of several well-known bridges, e.g. the Hardanger Bridge, while *Subspace State Space System Identification* (N4SID) methods is a newer family of methods well known for their robustness, accuracy and ease to use. It turns out that the N4SID method used in this thesis produces far better damping estimates than the CBHM method.

The proposed experimental setup seems promising for further research and development, although it has several drawbacks and limitations.

Preface

This thesis constitutes the result of the final semester of my master's degree program at the Norwegian University of Science and Technology (NTNU), Trondheim, Norway. The work has been carried out at the Faculty of Engineering Science and Technology, Department of Structural Engineering, under the supervision of Associate Professor Ole Andre Øiseth and Professor Ragnar Sigbjörnsson.

It has been interesting to work on a problem where I was able to compare theory with practice. It was also motivating that the experimental setup investigated during this work have not been (successfully) developed earlier.

I found it particularly interesting to learn some of the basic theory behind system identification, which I was completely unfamiliar with at the beginning of this work.

Lars Halvor Kaasa Trondheim, June 2011

Acknowledgements

This work was financially supported by a grant from the Norwegian Public Roads Administration, which I greatly appreciate. They also provided technical information about the Hardanger Bridge.

I would like to express my gratitude to my main supervisor, Associate Professor Ole Andre Øiseth, for his motivation, support and guidance of this work, and for allowing me to drop by his office with questions whenever I needed to. I am also grateful for the support of my co-supervisor Ragnar Sigbjörnsson.

I also wish to thank Associate Professor Anders Rönnquist for his encouragement and positive attitude, which not only inspired me during my work, but also made me specialise in structural dynamics in the first place.

Finally, I would like to thank the laboratory staff at the Department of Structural Engineering, which has been helpful during my work of building a prototype of the suspension rig. Particularly, I would express my gratitude to Senior Engineer Odd Kristian Nerdahl, who guided and supported me during preparations, and Paul Brekka Rike, who helped me set up the load cells.

Contents

List of figures

List of tables

1 Introduction

1.1 Background

As modern bridge design continuously aims for longer and slender bridges, it is necessary to be able to determine aerodynamic properties of such structures with a high degree of accuracy. The loads induced on a structure subjected to wind are a result of a complex interaction between the flow of air and the structure itself, rendering analytical and computational simulations computationally challenging [37]. Hence, prediction of response of a structure subjected to wind usually implies model scale experiments in a wind tunnel, whereon the results are interpreted and extrapolated to the full scale structure. These experiments provide valuable information about the aerodynamic and aeroelastic behaviour of a bridge deck that would otherwise be hard to obtain. To achieve additional insight, experiments may be enhanced by *computational fluid dynamic* (CFD) analyses [10], but this is computationally expensive and not common at present.

Traditional section model testing in wind tunnel was first used by Scanlan and Tomko [41]. A section model is a stiff, shape-wise representative segment of a full scale structure [15]. The testing has traditionally been performed in a suspension rig that allows vertical and rotational motion only, as shown in Figure 1.1. The motivation for the restraining of

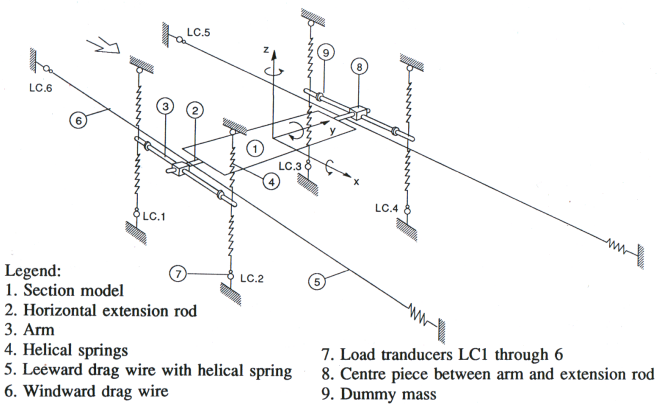

Figure 1.1: Sketch of a traditional suspension rig [15].

horizontal motion is mainly an issue of practical considerations that arise by introducing additional degrees of freedom into the system; the setup itself is likely to lack the simplicity of the two-degree-of-freedom-setup and the motion of the section model become more complex – hence it becomes harder to obtain accurate identifications of the aerodynamic derivatives [10]. Finally, the horizontal motion has traditionally been considered to be of less importance.

A section model exposed to a wind field may be used to perform a direct comparison of different bridge deck configurations. More importantly, loads exerted by the wind flow may be extracted and characteristic aerodynamic quantities such as static load coefficients, admittance functions and aerodynamic derivatives may be obtained as functions of the reduced velocity. These properties may then be used to predict dynamic response of the full scale structure. Since *flutter*, i.e. coupling of the fundamental vertical and torsional mode, usually is the critical instability phenomenon for bridges [49], it is traditionally assumed that the horizontal motion does not affect the aerodynamic properties associated with the vertical and torsional motion. The aerodynamic derivatives associated with horizontal motion has either been estimated by quasi-static values or chosen by experience [49].

Given the lower stiffness and increased horizontal motion of longer and slender bridges, these simplifications may significantly decrease accuracy of response and flutter predictions. The importance of the horizontal degree of freedom on coupled aeroelastic effects has been emphasised by e.g. Katsuchi et al. [23] and Mishra et al. [33]. Hence it is desirable to design an experimental setup that allows a horizontal degree of freedom. It is also necessary to implement a system identification method capable of extracting the aerodynamic derivatives, including those related to horizontal motion.

1.2 State of the art experimental setups

There has only been developed a few setups allowing for a horizontal degree of freedom that have been described in the literature. The most frequently encountered concept was developed and tested by Sarkar and Chowdhury [10,37], and is shown in Figure 1.2. Unlike traditional setups, the section model is not suspended in wires, but rather supported by pneumatic bushings that glide along polished steel shafts. This not only allows independent motion in both horizontal, vertical and torsional degrees of freedom, but also makes it possible to restrain motion in one or more directions. Hence, it possible to isolate and test the response of a single mode, and more importantly, to investigate coupling effects between any combination of two modes. This is favourable, because it was found that system identification based on motion involving three degrees of freedom tends to be less accurate.

Singh et al. [22, 42] used this setup to determine lateral aerodynamic derivatives of various bridge decks. Their main findings indicate that theoretical expressions of the

Figure 1.2: Rig allowing three degrees of freedom [10, 37].

aerodynamic derivatives associated with horizontal motion may give a good approximation in one case, but a rather crude approximation in another – the accuracy is highly dependent on the shape of the bridge deck. Furthermore, the theoretical values are not always conservative. In some cases there are also trends of structural stiffening effects due to the interaction between the horizontal motion and the flow of air, and hence modification of frequencies associated with this motion. This may be of significance in understanding wind-induced motion of large bridges.

1.3 Scope of present work

The drawback of the system described above, is that it require expensive components and precision machined parts to avoid excessive (frictional) damping. It is therefore desirable to develop a simple suspension rig, based on a traditional wire setup, that allows horizontal motion in addition to vertical and torsional motion.

The goal of the work presented herein is to *develop a suspension rig with a horizontal, a vertical and a torsional degree of freedom that is suitable for determination of aerodynamic derivatives in the wind tunnel at NTNU.*

The problem comprises three parts:

1. Design, build and test a suspension rig prototype to be used in still air, i.e. not in the wind tunnel.
2. Implement and test system identification methods that are suitable to determine dynamic properties of the section model.
3. Investigate non-linear effects due to the introduction of a horizontal degree of freedom.

The section model mounted in the rig will be based on the Hardanger Bridge. Due to time considerations, wind tunnel testing is not possible, and hence aerodynamic derivatives will not be determined.

As the setup may be used for further research, effort will be made to provide user-friendly tools to assist the design process of new section models, including a FE-model for dynamic simulation in Abaqus/CAE, Microsoft Excel spreadsheets and MATLAB code for system identification.

2 Basic theory

To ensure that the design of the suspension rig is well suited for measurements of the aerodynamic properties of bridge decks, it is important to understand relevant theory. This chapter will focus on theory of model scale experiments, aerodynamic derivatives and methods of system identification. A brief part concerning signal processing is also presented.

2.1 Model scale experiments

Model scale experiments can provide useful information about structural problems where full scale measurements are not feasible. This may be because the model experiments are a part of the design process of a structure that do not yet exist, or because it is difficult and/or expensive to carry out experiments on it.

In general, a scale model is used to predict physical characteristics of a full scale system, such as displacements, velocities, accelerations and forces [57]. Physical characteristics are often described by relevant (dimensionless) parameters capable of representing the full scale system, which in turn can be used to ensure proper scaling of the model.

In wind engineering, *aeroelastic* simulations are capable of providing information on the overall wind induced mean and dynamic loads and responses of a structure [7]. Aeroelasticity comprises the interaction between aerodynamic, elastic and inertial forces. One of the most common ways to perform aeroelastic simulations, is by section model tests.

2.1.1 Section models

A section model is a rigid model of a typical section of a slender, line-like structure, e.g. a bridge. It is more or less impossible to represent features such as cables and hangers correctly on an aeroelastic section model [15], and hence they are usually not included in the setup. The section model is dynamically mounted, traditionally by springs and wires (see Figure 1.1), where the setup is configured to achieve certain dynamic properties,

e.g. natural frequencies and damping ratios. It is often orientated perpendicular to the air stream, consequently ignoring any three-dimensional effects along the longitudinal axis of the structure [12]. Since only a part of the structure is examined, the geometric scale can be relatively large, typically in the range between 1:10 and 1:100.

The main use of section model tests lies in the detection of unstable motion [49], which for bridges usually is the phenomenon of *flutter*, i.e. a coupling of two or more modes, often associated with vertical and torsional motion. This coupling occur at high mean wind velocities due to motion induced changes in the effective structural stiffness. These changes are governed by the *aerodynamic derivatives*, described in detail in section 2.2. The aerodynamic derivatives can be determined by systematic testing involving a suitable range of reduced velocities. *Static load coefficients* and *aerodynamic admittance functions*, for use in calculations of buffeting response, can also be determined.

Section model tests are of major importance during the design process of e.g. a bridge, since the deck profile can be aerodynamically optimised. Such optimisation may involve reshaping the deck profile to increase critical (flutter) velocity, and installation of guide vanes to minimise response due to vortex shedding and buffeting [50].

2.1.2 Similitude

To obtain results representative for the full scale structure, it is important that the model is correctly scaled.

A scale model is said to have *complete similitude* with the full scale structure if they are geometric, kinematic and dynamic similar. According to Buckingham's π-theorem [5], any physically meaningful equation involving n variables can be rewritten to an equation of $n - m$ dimensionless parameters, where m is the number of fundamental dimensions, e.g. mass, length and time, used to rewrite the equation. Thus, a series of relevant dimensionless parameters of the full scale structure should be duplicated in the model and the wind field. However, complete duplication of these parameters is impractical. As a matter of fact, the requirements can only be satisfied exactly when the model and the full scale structure are identical [51]. Hence, only the important parameters should be satisfied, rendering a model having *partial similitude* with the full scale structure.

The most important parameters are briefly outlined below.

2.1.2.1 Similarity of wind

The simulation of natural wind in a wind tunnel can be considered in two categories. The *near field* simulation considers topographical conditions in the vicinity of the structure, while the *far field* simulation preserves the average characteristics of the turbulent boundary layer air flow. The former may require installation of geometrically scaled surroundings in the wind tunnel, while the latter concerns preservation of wind parameters,

particularly regarding turbulence. Section model tests of bridges usually emphasise far field simulation, as long bridges often spans above a flat water surface.

The most important turbulence parameters are *turbulence intensities* and *turbulence integral length scales*, together with spectral densities of fluctuating wind components and spatial correlations of these [51]. Spectral densities and corresponding co-spectra are usually encountered in a *reduced* (dimensionless) form. Scaling of mean wind velocity distributions is usually not important for section model tests of bridges [7, 15].

Details about the parameters mentioned above are outside the scope of this paper, but can be found in e.g. [49].

2.1.2.2 Aeroelastic similarity of section model

To achieve aeroelastic similarity, the following dimensionless parameters should (theoretically) be equal in full scale and model scale:

Reynolds number can be defined as the ratio of the fluid inertia force to the fluid viscous force [51].

$$\mathrm{Re} = \frac{F_i}{F_v} = \frac{\rho_a L^3 V^2/L}{\mu_a L V} = \frac{\rho_a L V}{\mu_a} \tag{2.1}$$

where ρ_a is the density of air, μ_a is the dynamic viscosity of air, L is a relevant characteristic linear dimension and V is the short term mean wind velocity. It is often impossible to maintain the Reynolds number in wind tunnel experiments, but the consequences are small if the model only has sharp corners. On the other hand, flow pattern around rounded corners and circular cylinders are very sensitive to the Reynolds number, and care should be taken if the section model contains such elements [15, 51].

Density ratio is the ratio of the structural material density to air density [51]. However, to maintain dynamic characteristics, it is enough to maintain the *mass ratio* in an overall way. By assuming an effective density ρ_{eff}, we get

$$\frac{\rho_{\mathrm{eff}}}{\rho_a} = \frac{\rho_{\mathrm{eff}} L^3/L}{\rho_a L^2} = \frac{m}{\rho_a L^2} \tag{2.2}$$

where m is mass per unit length of the structure. Similarly, in torsional problems, the ratio is based on moment of inertia per unit length of structure, m_I, giving the ratio

$$\frac{m_I}{\rho_a L^4}$$

Froude number is the ratio of fluid inertia force to gravitational force [51]:

$$\mathrm{Fr} = \frac{F_i}{F_g} = \frac{\rho_a L^3 V^2/L}{\rho_a L^3 g} = \frac{V^2}{gL} \tag{2.3}$$

where g is the acceleration of gravity. Consequently, Froude numbers become important for wind-induced response of cable-supported structures like suspension bridges, where geometric stiffness due to gravity is a dominant factor. However, as long as full scale displacements are small and the geometric stiffness is nearly invariant with respect to mean wind velocity, literal Froude-scaling is not necessary [15].

Cauchy number is defined as the ratio of elastic force to fluid inertia force [51]:

$$\mathrm{Ca} = \frac{F_e}{F_i} = \frac{E_{\mathrm{eff}} L^2}{\rho_a L^3 V^2 / L} = \frac{E_{\mathrm{eff}}}{\rho_a V^2} \tag{2.4}$$

where E_{eff} is the effective bulk modulus of elasticity, depending on the type of model. Considering the natural frequency of the structure,

$$\omega = \sqrt{\frac{E_{\mathrm{eff}} I}{m}}$$

this ratio can be rewritten to

$$\mathrm{Ca} = \frac{E_{\mathrm{eff}} I / L^2}{\rho_a V^2 / L^2} = \left(\frac{\omega L}{V}\right)^2 \frac{m}{\rho_a L^2} = \frac{1}{\hat{V}^2} \frac{m}{\rho_a L^2} \tag{2.5}$$

where

$$\hat{V} = \frac{V}{\omega L} \tag{2.6}$$

is the *reduced velocity* and $m/\rho_a L^2$ is the mass ratio derived above.

It is seen that the Cauchy number is maintained if the reduced velocity and mass ratio is equal in model scale and full scale. For a section model, it is maintained in an overall way, by pooling all straining and gravitational (geometric) stiffness into $E_{\mathrm{eff}} I$ [15].

As structural response depends on frequency content, mean wind velocity and geometric scaling, it is common to analyse it as a function of reduced velocity.

Modal damping ratio is an important parameter in the prediction of structural response [51]. It is, however, very difficult, if not impossible, to measure the damping of a structure, not to say a structure that not yet exist. To simulate worst case conditions, it is common to assume as low damping as possible, but additional damping could be introduced by letting vanes connected to the model shear through e.g. silicone oil [15].

In addition to the dimensionless quantities described above, the *Scruton number*, which relates mass and damping of bluff and round sections, and the *Strouhal number*, which is related to vortex shedding, is worth mentioning. However, these numbers will not be focused on in the present work.

2.1.3 Scaling

Based on the scaling laws described above, it is evident that Reynold numbers can not be preserved. It is also seen that it is impossible to maintain Froude numbers, since it is important to investigate the behaviour of the section model under various mean wind velocities. Finally, modal damping ratios are hard to scale correctly. Instead, they are usually chosen as small as possible, i.e. no additional damping is introduced into the suspension rig.

What then remains, are the requirements regarding wind similarity, geometric scaling, mass ratio and reduced wind velocity. Hence, the following full-scale quantities are needed for designing the model and suspension rig [15]:

- Geometrical shape.
- Equivalent constant mass per unit length of span, calculated to give correct modal mass if the distribution is non-uniform.
- Equivalent constant moment of inertia per unit length of span, calculated to give correct modal moment of inertia if the distribution is non-uniform.
- Range of relevant mean wind velocities.
- Natural frequencies (and possibly modal damping ratios) of relevant modes.
- Turbulence properties of the wind, i.e. intensities, integral length scales, reduced auto-spectra and normalised co-spectra of all components.

After deciding on a geometric scale factor λ and a wind velocity scale factor ν, the target model properties are found by Table 2.1.

Quantity	Full scale	Scale factor	Model scale
Length	L_{fs}	λ	$L_{\text{ms}} = \lambda \cdot L_{\text{fs}}$
Mass per unit length	m_{fs}	λ^2	$m_{\text{ms}} = \lambda^2 \cdot m_{\text{fs}}$
Moment of inertia per unit length	$m_{I,\text{fs}}$	λ^4	$m_{I,\text{ms}} = \lambda^4 \cdot m_{I,\text{fs}}$
Mean wind velocity	V_{fs}	ν	$V_{\text{ms}} = \nu \cdot V_{\text{fs}}$
Natural frequencies	$f_{k,\text{fs}}$	ν/λ	$f_{k,\text{ms}} = \nu/\lambda \cdot f_{k,\text{fs}}$
Modal damping ratios	$\zeta_{k,\text{fs}}$	1	$\zeta_{k,\text{ms}} = \zeta_{k,\text{fs}}$
Turbulence intensities	$I_{n,\text{fs}}$	1	$I_{n,\text{ms}} = I_{n,\text{fs}}$
Integral length scales	${}^{s}L_{n,\text{fs}}$	λ	${}^{s}L_{n,\text{ms}} = \lambda \cdot {}^{s}L_{n,\text{fs}}$
Reduced turbulence auto-spectra	$\hat{S}_{n,\text{fs}}$	1	$\hat{S}_{n,\text{ms}} = \hat{S}_{n,\text{fs}}$
Normalised turbulence co-spectra	$\hat{C}o_{nn,\text{fs}}$	1	$\hat{C}o_{nn,\text{ms}} = \hat{C}o_{nn,\text{fs}}$

Table 2.1: Scaling of full scale quantities, where k is mode number, n refer to turbulence component and s refer to flow direction.

2.1.4 Limitations

Results obtained by model tests will never be better than the model's ability to represent the full scale structure and the load conditions applied to it. Hence, the results from section model tests are only directly applicable to a full scale structure with geometry, frequency ratios, mode shapes, damping, modal mass and moment of inertia etc. equivalent to that of the model [50], which for all practical purposes do not coincide with the actual full scale properties.

Given that the scaling of the model is performed adequately, there is still one major difference between a section model and the corresponding full scale structure. The dimensionless shape-wise similarity ψ of two modes a and b is defined by

$$\psi_{ab} = \frac{\int_{L_{exp}} \phi_a \phi_b \, \mathrm{d}x}{\int_L \phi_a^2 \, \mathrm{d}x} \cdot \frac{\int_{L_{exp}} \phi_a \phi_b \, \mathrm{d}x}{\int_L \phi_b^2 \, \mathrm{d}x} \tag{2.7}$$

where ϕ_a and ϕ_b represent the mode shapes of mode a and b, respectively. Here, $\psi_{ab} = 1$ indicates that the modes match perfectly, i.e. they are shape-wise similar, and $\psi_{ab} = 0$ indicates that they are shape-wise dissimilar [19].

Section models are practically rigid, implying that the more or less flexible modes of the full scale structure must be represented by the rigid modes of the model. That is, the mode shapes in model scale and full scale are not equal, and the shape-wise similarity between all symmetric modes of the section model will be 1 – perfectly similar. On the other hand, the Hardanger Bridge, for instance, has a shape-wise similarity of the symmetric vertical and torsional mode shapes of $\psi_{z\theta} = 0.57$ [19]. This implies that flutter most likely will occur at a lower reduced wind speed for the section model tests than for the full scale bridge, and thus gives conservative estimates on critical wind velocity. Further, since aerodynamic parameters can not be identified beyond the critical velocity, they have to be extrapolated to estimate the true critical velocity of the full scale bridge. Finally, it also implies that a section model can represent the full scale structure aerodynamically, but not dynamically.

There are also other important limitations of section model tests. First, only a section of the bridge deck is modelled; features like suspension cables and hangers are ignored. Second, it is nearly impossible to have the flow of air in the wind tunnel accurately representing the natural wind that acts on the full scale bridge structure, and the response tends to be extremely sensitive to a change in wind direction [51]. End effects may also disturb the results, particularly if the section model is short. The latter may, however, be reduced by attaching end plates, parallel to the flow, to each side of the section model.

For further information about wind tunnel testing, the reader is referred to [15] and the manual prepared by the American Society of Civil Engineers [7].

2.2 Aerodynamic derivatives

Even though determination of aerodynamic derivatives (ADs) itself is outside the scope of this work, it is important to understand how they are identified, since it is the main use of the suspension rig.

2.2.1 Definition

The concept of aerodynamic derivatives was introduced by Scanlan and Tomko [41] in 1971. They considered frequency dependency of response calculations by introducing six frequency dependent coefficients: H_i^* and A_i^*, i =1-3. Singh et al. [42] extended the analysis procedure described by Scanlan and Jones [40] to include the entire complement of 18 aerodynamic derivatives: P_i^*, H_i^* and A_i^*, where i =1-6.

The three degrees of freedom relevant for determination of ADs are the horizontal deflection p, the vertical deflection h and the rotation α about the local shear centre. The corresponding drag D, lift L and overturning moment M per unit span can be represented by

$$D = D_b + D_{ae} \tag{2.8a}$$

$$L = L_b + L_{ae} \tag{2.8b}$$

$$M = M_b + M_{ae} \tag{2.8c}$$

where the subscripts b and ae refer to *buffeting* and *aeroelastic* quantities, respectively. The motion induced forces can be represented completely by

$$D_{ae} = \frac{1}{2}\rho_a V^2 B \left[\hat{\omega} P_1^* \frac{\dot{p}}{V} + \hat{\omega} P_2^* \frac{B\dot{\alpha}}{V} + \hat{\omega}^2 P_3^* \alpha + \hat{\omega}^2 P_4^* \frac{p}{B} + \hat{\omega} P_5^* \frac{\dot{h}}{V} + \hat{\omega}^2 P_6^* \frac{h}{B}\right] \tag{2.9a}$$

$$L_{ae} = \frac{1}{2}\rho_a V^2 B \left[\hat{\omega} H_1^* \frac{\dot{h}}{V} + \hat{\omega} H_2^* \frac{B\dot{\alpha}}{V} + \hat{\omega}^2 H_3^* \alpha + \hat{\omega}^2 H_4^* \frac{h}{B} + \hat{\omega} H_5^* \frac{\dot{p}}{V} + \hat{\omega}^2 H_6^* \frac{p}{B}\right] \tag{2.9b}$$

$$M_{ae} = \frac{1}{2}\rho_a V^2 B^2 \left[\hat{\omega} A_1^* \frac{\dot{h}}{V} + \hat{\omega} A_2^* \frac{B\dot{\alpha}}{V} + \hat{\omega}^2 A_3^* \alpha + \hat{\omega}^2 A_4^* \frac{h}{B} + \hat{\omega} A_5^* \frac{\dot{p}}{V} + \hat{\omega}^2 A_6^* \frac{p}{B}\right] \tag{2.9c}$$

where ρ_a is the air density, V is the mean wind velocity, B is the section model deck width and $\hat{\omega}$ is the *reduced circular frequency*, defined by

$$\hat{\omega} = \frac{B\omega}{V} = \frac{1}{\hat{V}}$$

where the reduced velocity $\hat{V}$ is defined in (2.6).

A modal dynamic system may be expressed by

$$\mathbf{M}_0\ddot{\mathbf{y}}(t) + \mathbf{C}_{\text{eff}}\dot{\mathbf{y}}(t) + \mathbf{K}_{\text{eff}}\mathbf{y}(t) = \mathbf{p}(t) \tag{2.10}$$

where

$$\mathbf{y}(t) = \begin{bmatrix} p & h & \alpha \end{bmatrix}^{\mathrm{T}} \tag{2.11a}$$

$$\mathbf{p}(t) = \begin{bmatrix} D_b & L_b & M_b \end{bmatrix}^{\mathrm{T}} \tag{2.11b}$$

$$\mathbf{C}_{\text{eff}} = \mathbf{C}_0 + \mathbf{C}_{ae} \tag{2.11c}$$

$$\mathbf{K}_{\text{eff}} = \mathbf{K}_0 + \mathbf{K}_{ae} \tag{2.11d}$$

and where $\mathbf{M}_0$, $\mathbf{C}_0$ and $\mathbf{K}_0$ are the mass, damping and stiffness matrix, respectively, in still air. The coefficients contained in $\mathbf{C}_{ae}$ and $\mathbf{K}_{ae}$ are functions of the frequency of motion, the mean wind velocity and the type of cross section, as well as the turbulence properties and angle of incidence of the oncoming flow [49].

By comparing (2.11) with (2.8) and (2.9), the following is obtained:

$$\mathbf{C}_{ae} = -\frac{1}{2}\rho_a B^2 \omega \hat{\mathbf{C}}_{ae} \tag{2.12a}$$

$$\mathbf{K}_{ae} = -\frac{1}{2}\rho_a B^2 \omega^2 \hat{\mathbf{K}}_{ae} \tag{2.12b}$$

where

$$\hat{\mathbf{C}}_{ae} = \begin{bmatrix} P_1^* & P_5^* & BP_2^* \\ H_5^* & H_1^* & BH_2^* \\ BA_5^* & BA_1^* & B^2A_2^* \end{bmatrix} \tag{2.13a}$$

$$\hat{\mathbf{K}}_{ae} = \begin{bmatrix} P_4^* & P_6^* & BP_3^* \\ H_6^* & H_4^* & BH_3^* \\ BA_6^* & BA_4^* & B^2A_3^* \end{bmatrix} \tag{2.13b}$$

and the aerodynamic derivatives are given by

$$\begin{bmatrix} P_1^* & H_1^* & A_1^* \\ P_2^* & H_2^* & A_2^* \\ P_3^* & H_3^* & A_3^* \\ P_4^* & H_4^* & A_4^* \\ P_5^* & H_5^* & A_5^* \\ P_6^* & H_6^* & A_6^* \end{bmatrix} = -\frac{2}{\rho_a B^2 \omega^2} \begin{bmatrix} \omega\left(C_{11}^{\text{eff}} - C_{11}^0\right) & \omega\left(C_{22}^{\text{eff}} - C_{22}^0\right) & \frac{\omega}{B}\left(C_{32}^{\text{eff}} - C_{32}^0\right) \\ \frac{\omega}{B}\left(C_{13}^{\text{eff}} - C_{13}^0\right) & \frac{\omega}{B}\left(C_{23}^{\text{eff}} - C_{23}^0\right) & \frac{\omega}{B^2}\left(C_{33}^{\text{eff}} - C_{33}^0\right) \\ \frac{1}{B}\left(K_{13}^{\text{eff}} - K_{13}^0\right) & \frac{1}{B}\left(K_{23}^{\text{eff}} - K_{23}^0\right) & \frac{1}{B^2}\left(K_{33}^{\text{eff}} - K_{33}^0\right) \\ \left(K_{11}^{\text{eff}} - K_{11}^0\right) & \left(K_{22}^{\text{eff}} - K_{22}^0\right) & \frac{1}{B}\left(K_{32}^{\text{eff}} - K_{32}^0\right) \\ \omega\left(C_{12}^{\text{eff}} - C_{12}^0\right) & \omega\left(C_{21}^{\text{eff}} - C_{21}^0\right) & \frac{\omega}{B}\left(C_{31}^{\text{eff}} - C_{31}^0\right) \\ \left(K_{12}^{\text{eff}} - K_{12}^0\right) & \left(K_{21}^{\text{eff}} - K_{21}^0\right) & \frac{1}{B}\left(K_{31}^{\text{eff}} - K_{31}^0\right) \end{bmatrix} \tag{2.14}$$

It is assumed that the ADs evolve as functions of the reduced velocity, i.e.

$$P_i^* = P_i^*(\hat{V}), \quad H_i^* = H_i^*(\hat{V}), \quad A_i^* = A_i^*(\hat{V}), \quad i = 1\text{-}6$$

which implies an assumption of perfectly harmonic modal motion [12].

2.2.2 Determination by section model tests

Equation (2.14) shows that the aerodynamic derivatives are determined by subtracting the damping and stiffness matrix in still air from the corresponding matrices determined under wind exposure.

Over the years, numerous methods have been developed to extract ADs from section model tests in wind tunnels, see e.g. [3,10,13,21,38,41,42]. In general, ADs are obtained by identifying the damping and stiffness matrix for a suitable range of reduced velocities, possibly also for various angles of incident and frequency configurations. Although the technical implementation varies, all methods either involve free vibration tests or forced vibration tests [36].

Both approaches have their advantages. Free vibration tests do not force any prescribed motion on the model, but rather allow the fluid-structure interaction to drive the motion. The disadvantage is that the aerodynamic damping may be onerous for large reduced velocities, rendering only a few cycles of oscillations before the motion is damped out – making it difficult to obtain good estimates of the effective damping and stiffness. The more technically demanding method of forced vibration, on the other hand, does not dampen out, and can obtain the structural matrices even for large reduced velocities – however at the cost of prescribed motion, which may distort modal coupling effects.

2.2.3 Limitations and error sources

Aerodynamic derivatives represent a linear form of the non-linear aerodynamic forces, so they are approximations, at best [36]. Moreover, it is assumed that the ADs are dependent on reduced velocity alone, but there is reason to suspect that they also are amplitude dependent [39].

Further, Sarkar et al. have performed a comparative study [36], where inter-laboratory data has been analysed. The study clearly shows presence of non-negligible dependence on the laboratory equipment and operational conditions, as well as on the method used to extract the ADs. It also emphasises the importance of uncertainty analysis of experimentally extracted ADs in the context of aeroelastic simulations [6].

Error in the extracted ADs can depend on many sources, including number of degrees of freedom, upstream turbulence, type of bridge section, sampling rate and sampling duration [36]. The effect of sampling rate and duration will be investigated in section 4.3.2.

2.3 System identification

System identification is the process of estimating the parameters of a mathematical model based on measured input and output. It may be thought of as the dynamic extent of curve fitting [54].

System identification methods can be considered in two categories: parametric and non-parametric methods. Parametric methods are performed on a model with a certain structure and which contains a parameter vector, while models determined by non-parametric methods are given by functions, curves or tables [17].

There is a wide range of methods available, but this thesis focuses on two parametric methods: the *covariance block Hankel matrix* (CBHM) method and an implementation of a subspace (N4SID) method. The *Iterative Least Squares* (ILS) method presented in [10] was implemented and tested, but the estimation of damping produced poor results; hence, it will not be focused on in the following. In addition, a preliminary analysis using non-parametric methods is described.

The CBHM method is a so-called *stochastic realisation method*, and is chosen because it has been extensively tested and successfully applied to relevant problems, i.e. determination of aerodynamic derivatives, by Jakobsen [20]. It is also being used by *Svend Ole Hansen ApS*, a Danish company that has performed several wind tunnel tests for the Norwegian Public Roads Administration, see e.g. [50]. Finally, the N4SID method is chosen because of it's robustness and ease to use – and because it is implemented in the *System Identification Toolbox* in MATLAB. Hence, it serves as a control for the CBHM method.

2.3.1 Mathematical models

Mathematical models represents reality in an idealised way, and should never be considered to be the truth. However, by careful modelling and understanding of a problem, mathematical models can provide valuable insight and information.

There are two different approaches of modelling [29]. *Tailor-made models* are constructed from basic physical principles, and the unknown parameters have, at least in principle, a physical interpretation. *Ready-made models*, or *black-box models*, are families of flexible models of general applicability. The parameters of these models do not necessarily have physical interpretations, but only describe the input-output relationships of the system. The model parameters are estimated by system identification of data from experimentation. The two approaches may very well be combined to enhance the understanding of the problem and confidence in the models.

The parameters of a model may be classified according to [29]:

Constants Quantities in the model that do not vary with time.

- *System parameter*: A constant that is given by the system.
- *Design parameter*: A constant that can be varied in order to give the system different properties.

Variables/signals Quantities in the model that vary with time.

- *Output*: A variable whose behaviour is the primary interest. Denoted by y.
- *External signal*: A variable that affects the system without being affected by the system's other variables.
- *Input*: An external signal in the system whose time variations can be chosen. Denoted by u.
- *Disturbance signal/noise*: An external signal in the system that cannot be influenced. Denoted by w.
- *Internal variable*: A variable in the system that is neither an output nor an external signal.

The block diagram of a basic model is shown in Figure 2.3.

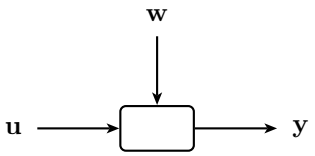

Figure 2.3: Basic model.

2.3.1.1 Transfer function models

A well-known family of ready-made dynamic models are the so-called *transfer function models*. They are parametric models constructed by assuming a rational transfer function G of the input, and a rational function H of the disturbance signal:

$$G(q,\theta) = \frac{B(q)}{F(q)} \tag{2.15a}$$

$$H(q,\theta) = \frac{C(q)}{D(q)} \tag{2.15b}$$

Here, q is the *time shift operator*, and B, C, D and F are polynomials that comprises the parameters θ of the model. By setting one or more of the polynomials equal to unity, different model classes are defined. The *Box-Jenkins* (BJ) and the *auto-regressive, moving average* (ARMA) models are frequently encountered examples of such classes.

2.3.1.2 State space models

In the present work, a different family of parametric models will be used. Since dynamic systems have memory, i.e. the output depends on all earlier input values, it is not possible to calculate the output $y(t)$ for $t > t_0$ – even if the input $u(t)$ for $t > t_0$ is known. It is necessary to know the *state* of the system at time t_0. The state at any given time t is described by *state variables* stored in the *state vector* $\mathbf{x}(t)$, and is in general dependent not only on the dynamic properties of the system, but on all earlier input values. The *model order*, the number of state variables in the model, should contain enough information to describe the system unambiguously, i.e. to calculate the output $y(t)$ for $t > t_0$ when the corresponding input is known.

A linear, time-invariant state space model in continuous time is described by the following set of equations:

$$\dot{\mathbf{x}}(t) = \mathbf{A}_c\mathbf{x}(t) + \mathbf{B}_c\mathbf{u}(t) + \mathbf{w}_c(t) \tag{2.16a}$$

$$\mathbf{y}(t) = \mathbf{C}\mathbf{x}(t) + \mathbf{D}\mathbf{u}(t) + \mathbf{v}(t) \tag{2.16b}$$

while the discrete-time counterpart is described by:

$$\mathbf{x}_{k+1} = \mathbf{A}_d\mathbf{x}_k + \mathbf{B}_d\mathbf{u}_k + \mathbf{w}_{d,k} \tag{2.17a}$$

$$\mathbf{y}_k = \mathbf{C}\mathbf{x}_k + \mathbf{D}\mathbf{u}_k + \mathbf{v}_k \tag{2.17b}$$

where $\mathbf{u}_k = \mathbf{u}(t_k)$, $\mathbf{x}_k = \mathbf{x}(t_k)$, $\mathbf{y}_k = \mathbf{y}(t_k)$, $\mathbf{v}_k = \mathbf{v}(t_k)$ and $t_k = k\Delta t$, assuming equidistant time spacing Δt. Quantities that differ in continuous and discrete time are subscripted with c and d, respectively. To obtain the relation between these two versions of the model, the solution of the first order differential equation in continuous time (2.16a), with initial conditions $\mathbf{x}(t_0)$, is considered:

$$\mathbf{x}(t) = e^{\mathbf{A}_c(t-t_0)}\mathbf{x}(t_0) + \int_{t_0}^{t} e^{\mathbf{A}_c(t-\tau)}\left(\mathbf{B}_c\mathbf{u}(\tau) + \mathbf{w}_c(\tau)\right)\,\mathrm{d}\tau \tag{2.18}$$

Comparison with the discrete-time version (2.17a) gives

$$\mathbf{A}_d = e^{\mathbf{A}_c\Delta t} \tag{2.19a}$$

$$\mathbf{B}_d = \mathbf{B}_c \int_0^{\Delta t} e^{\mathbf{A}_c(\Delta t-\tau)}\,\mathrm{d}\tau \tag{2.19b}$$

$$\mathbf{w}_{d,k} = \mathbf{w}_c(k\Delta t) \int_0^{\Delta t} e^{\mathbf{A}_c(\Delta t-\tau)}\,\mathrm{d}\tau \tag{2.19c}$$

To get a better understanding of the model, an introduction to the terms of the discrete-time version, stated by Van Overschee and De Moor [54], is briefly summarised below.

The vectors $\mathbf{u}_k \in \mathbb{R}^m$ and $\mathbf{y}_k \in \mathbb{R}^n$ are the measurements of respectively m inputs and n outputs of a process at a given time instant k, and it is assumed that $\mathbf{u}_k$ is available without measurement noise. The vector $\mathbf{x}_k \in \mathbb{R}^l$ is the state vector of the process, and contains the values of l state variables at time instant k. The state variables do not necessarily have a direct physical interpretation.

The stochastic vectors $\mathbf{w}_k \in \mathbb{R}^l$ and $\mathbf{v}_k \in \mathbb{R}^n$ contains the unmeasurable input and output noise, respectively, and are assumed to be zero mean, stationary, white noise vector sequences. This implies that instantaneous correlation between the input and output noise may occur, but the covariance is zero for any time lag $\tau > 0$:

$$\mathrm{E}\left[\begin{bmatrix}\mathbf{w}_p \\ \mathbf{v}_p\end{bmatrix}\begin{bmatrix}\mathbf{w}_q^{\mathrm{T}} & \mathbf{v}_q^{\mathrm{T}}\end{bmatrix}\right] = \begin{bmatrix}\mathbf{C_{ww}}(p,q) & \mathbf{C_{wv}}(p,q) \\ \mathbf{C}_{\mathbf{wv}}^{\mathrm{T}}(p,q) & \mathbf{C_{vv}}(p,q)\end{bmatrix}\delta_{pq} \geq 0, \quad \delta_{pq}\begin{cases}1 & \text{if } p = q \\ 0 & \text{if } p \neq q\end{cases} \tag{2.20}$$

where E is the expectation value operator, δ_{pq} is the Kronecker delta, and $\mathbf{C_{ww}} \in \mathbb{R}^{l\times l}$, $\mathbf{C_{wv}} \in \mathbb{R}^{l\times n}$ and $\mathbf{C_{vv}} \in \mathbb{R}^{n\times n}$ are the covariance matrices of the noise sequences.

The dynamic system matrix $\mathbf{A}_d \in \mathbb{R}^{l\times l}$ completely describes the dynamics of the system, which is characterised by its eigenvalues. The input matrix $\mathbf{B}_d \in \mathbb{R}^{l\times m}$ represents a linear transformation which describes how the next state is influenced by the deterministic input, while the output matrix $\mathbf{C} \in \mathbb{R}^{n\times l}$ describes the transformation of the internal state to the output measurements $\mathbf{y}_k$. The *direct feedthrough*-matrix $\mathbf{D} \in \mathbb{R}^{n\times m}$ represents any direct coupling between inputs and outputs of the system. In continuous systems this is usually not the case, but it may be present in discrete systems due to the sampling.

The matrix pair $\{\mathbf{A}_d, \mathbf{C}\}$ is assumed to be observable, which implies that *all modes* in the system can be observed, and thus identified, in the stochastic output $\mathbf{y}_k$. The matrix pair $\left\{\mathbf{A}_d, \begin{bmatrix}\mathbf{B}_d & \mathbf{Q^{1/2}}\end{bmatrix}\right\}$ is assumed to be controllable, which in turn implies that *all modes* of the system are excited by either the deterministic input $\mathbf{u}_k$ or the stochastic input $\mathbf{w}_k$. The concepts of observability and controllability are briefly discussed below.

Figure 2.4 illustrates the discrete state space model. The symbol $\boldsymbol{\Delta}$ represents a delay, and the feedback via the matrix $\mathbf{A}_d$ represents the dynamics of the system.

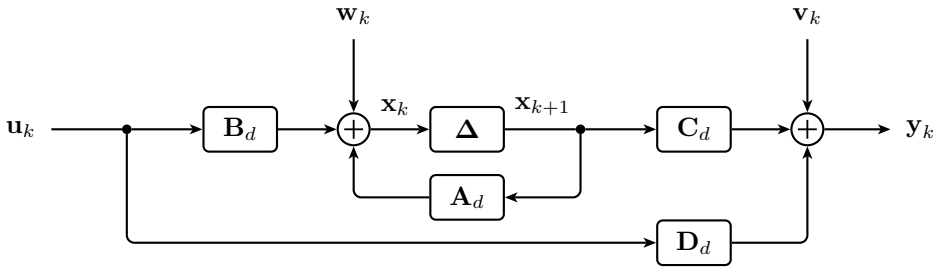

Figure 2.4: Discrete state space model [54].

2.3.1.3 Observability and controllability

The concepts of *observability* and *controllability*, introduced above, are defined more precisely by Chen [8].

Observability studies the possibility of estimating the state from the output, given that $\mathbf{A}$, $\mathbf{B}$, $\mathbf{C}$ and $\mathbf{D}$ are known. The state equation is said to be observable if for any unknown initial state $\mathbf{x}_0$, the knowledge of the input $\mathbf{u}$ and the output suffices to determine uniquely the initial state $\mathbf{x}_0$ in a finite time. If the state equation is observable, the *observability matrix*

$$\mathbf{Q}_o = \begin{bmatrix} \mathbf{C} & \mathbf{CA} & \mathbf{CA}^2 & \cdots & \mathbf{CA}^{l-1} \end{bmatrix}^{\mathrm{T}} \tag{2.21}$$

where $\mathbf{Q}_o \in \mathbb{R}^{nl \times l}$, n being the number of outputs and l the number of state variables, has full rank.

The concept of controllability is dual to that of observability. Hence, the state equation is said to be controllable if for any initial state $\mathbf{x}_0$ and any final state $\mathbf{x}_1$, there exists an input that transfers $\mathbf{x}_0$ to $\mathbf{x}_1$ in a finite time. If the state equation is observable, the *controllability matrix*

$$\mathbf{Q}_c = \begin{bmatrix} \mathbf{B} & \mathbf{AB} & \mathbf{A}^2\mathbf{B} & \cdots & \mathbf{A}^{l-1}\mathbf{B} \end{bmatrix} \tag{2.22}$$

where $\mathbf{Q}_c \in \mathbb{R}^{l \times ml}$, m being the number of inputs and l the number of state variables, has full rank. When describing a transfer from the zero state, controllability is often referred to as *reachability*.

2.3.1.4 Similarity transformation

A similarity transformation of the state space system may be introduced by a linear transformation of the state vector [20, 43], such that

$$\mathbf{x}_k^* = \mathbf{T}\mathbf{x}_k \tag{2.23}$$

where the number of state variables in the transformed system is the same as in the original system, i.e. $\mathbf{T}$ is a square matrix. This renders the system matrices of the transformed system:

$$\mathbf{A}^* = \mathbf{TAT}^{-1} \tag{2.24a}$$
$$\mathbf{B}^* = \mathbf{TB} \tag{2.24b}$$
$$\mathbf{C}^* = \mathbf{CT}^{-1} \tag{2.24c}$$
$$\mathbf{D}^* = \mathbf{D} \tag{2.24d}$$

It can be shown that eigenvalues are unaffected by a similarity transformation [43].

2.3.2 Model of a dynamic structural system

2.3.2.1 State space model

A damped structural dynamic system of n degrees of freedom exposed to a stochastic load, e.g. from a turbulent wind field, may be described by a system of n coupled second order linear differential equations:

$$\mathbf{M}_0\ddot{\mathbf{y}}(t) + \mathbf{C}_{\text{eff}}\dot{\mathbf{y}}(t) + \mathbf{K}_{\text{eff}}\mathbf{y}(t) = \mathbf{p}(t) \tag{2.25}$$

where $\mathbf{y}(t) \in \mathbb{R}^n$ contains the modal degrees of freedom, $\mathbf{p}(t) \in \mathbb{R}^n$ is the time varying load vector of the system, $\mathbf{M}_0 \in \mathbb{R}^{n\times n}$ is the modal mass matrix, $\mathbf{C}_{\text{eff}} \in \mathbb{R}^{n\times n}$ is the effective viscous damping matrix and $\mathbf{K}_{\text{eff}} \in \mathbb{R}^{n\times n}$ is the effective stiffness matrix. The modal mass matrix is assumed to be constant, while the effective damping and stiffness matrix vary with motion induced wind forces, discussed in section 2.2.

The above system of second order differential equations can be rewritten to a system of $2n$ first order differential equations [17, 20]:

$$\begin{bmatrix}\dot{\mathbf{y}}(t)\\ \ddot{\mathbf{y}}(t)\end{bmatrix} = \begin{bmatrix}\mathbf{0} & \mathbf{I}\\ -\mathbf{M}_0^{-1}\mathbf{K}_{\text{eff}} & -\mathbf{M}_0^{-1}\mathbf{C}_{\text{eff}}\end{bmatrix}\begin{bmatrix}\mathbf{y}(t)\\ \dot{\mathbf{y}}(t)\end{bmatrix} + \begin{bmatrix}\mathbf{0}\\ \mathbf{M}_0^{-1}\end{bmatrix}\mathbf{p}(t) \tag{2.26}$$

The rewritten system may now be interpreted as a continuous-time state space model:

$$\dot{\mathbf{x}}(t) = \mathbf{A}_c\mathbf{x}(t) + \mathbf{B}_c\mathbf{p}(t) \tag{2.27a}$$
$$\mathbf{y}(t) = \mathbf{C}\mathbf{x}(t) + \mathbf{v}(t) \tag{2.27b}$$

where

$$\mathbf{x}(t) = \begin{bmatrix}\mathbf{y}(t)\\ \dot{\mathbf{y}}(t)\end{bmatrix} \tag{2.28a}$$
$$\mathbf{A}_c = \begin{bmatrix}\mathbf{0} & \mathbf{I}\\ -\mathbf{M}_0^{-1}\mathbf{K}_{\text{eff}} & -\mathbf{M}_0^{-1}\mathbf{C}_{\text{eff}}\end{bmatrix} \tag{2.28b}$$
$$\mathbf{B}_c = \begin{bmatrix}\mathbf{0}\\ \mathbf{M}_0^{-1}\end{bmatrix} \tag{2.28c}$$
$$\mathbf{C} = \begin{bmatrix}\mathbf{I} & \mathbf{0}\end{bmatrix} \tag{2.28d}$$

and $\mathbf{v} \in \mathbb{R}^n$ contains the stochastic output noise. From the description of state space models above, it is now readily seen that $\mathbf{x}(t) \in \mathbb{R}^{2n}$ is the state vector, $\mathbf{A}_c \in \mathbb{R}^{2n\times 2n}$ is the dynamic system matrix, $\mathbf{B}_c \in \mathbb{R}^{2n\times n}$ is the input matrix and $\mathbf{C}_c \in \mathbb{R}^{n\times 2n}$ is the output matrix. There is no direct feedthrough in the model. The load vector $\mathbf{p}(t) \in \mathbb{R}^n$ has replaced the deterministic input $\mathbf{u}(t)$ and the stochastic noise $\mathbf{w}(t)$ in (2.16a). In wind engineering, it is common to assume that the fluctuating wind load $\mathbf{p}(t)$ is a Gaussian, zero mean, stationary white noise process [49].

For all practical purposes, records of inputs and outputs are obtained by sampling a continuous-time process, and hence a discrete-time model has to be applied:

$$\mathbf{x}_{k+1} = \mathbf{A}_d \mathbf{x}_k + \mathbf{B}_d \mathbf{p}_k \tag{2.29a}$$

$$\mathbf{y}_k = \mathbf{C}\mathbf{x}_k + \mathbf{v}_k \tag{2.29b}$$

If it is assumed that the recorded signal $\mathbf{y}$ has zero mean value, i.e. only contains the fluctuating part of the dynamic response, the model in (2.29) describes a system driven by a white noise process $\mathbf{p}$. It also takes into account that the response is corrupted by white measurement noise $\mathbf{v}$, possibly instantaneously correlated with the excitation process $\mathbf{p}$, such that

$$\mathrm{E}\left[\begin{bmatrix}\mathbf{p}_k \\ \mathbf{v}_l\end{bmatrix}\begin{bmatrix}\mathbf{p}_k^{\mathrm{T}} & \mathbf{v}_l^{\mathrm{T}}\end{bmatrix}\right] = \begin{bmatrix}\mathbf{C}_{\mathbf{pp}}(k,l) & \mathbf{C}_{\mathbf{pv}}(k,l) \\ \mathbf{C}_{\mathbf{pv}}^{\mathrm{T}}(k,l) & \mathbf{C}_{\mathbf{vv}}(k,l)\end{bmatrix}\delta_{kl} \geq 0 \tag{2.30}$$

2.3.2.2 Impulse response

Successive application of (2.29a) relates sample k and $k+m$ of the state vector:

$$\mathbf{x}_{k+m} = \mathbf{A}_d^m \mathbf{x}_k + \sum_{s=k}^{k+m-1} \mathbf{A}_d^{k+m-s-1} \mathbf{B}_d \mathbf{p}_s \tag{2.31}$$

and the output becomes

$$\mathbf{y}_{k+m} = \mathbf{C}\mathbf{A}_d^m \mathbf{x}_k + \sum_{s=k}^{k+m-1} \mathbf{C}\mathbf{A}_d^{k+m-s-1} \mathbf{B}_d \mathbf{p}_s + \mathbf{v}_{k+m} \tag{2.32}$$

The matrix product under the summation sign is the impulse-response matrix:

$$\mathbf{R}(k+m, s) = \mathbf{C}\mathbf{A}_d^{k+m-s-1}\mathbf{B}_d \tag{2.33}$$

which gives the response of the system at the time instant $(k+m)\Delta t$ due to the load at the instant $s\Delta t$, where $s = k, k+1, \ldots, k+m-1$. The influence of the load history $\mathbf{p}_s$ for $s = 1, 2, \ldots, k-1$ is contained in the state vector $\mathbf{x}_k$. $\mathbf{R}(k+m, s)$ is called the *Markov parameters* of the system [17, 20].

2.3.2.3 Eigenvalues and eigenvectors

The eigenvalues of the asymmetric continuous-time matrix $\mathbf{A}_c$ appears as complex conjugate pairs [17]:

$$\lambda_{A_c} = -\xi\omega_0 \pm i\omega_0\sqrt{1-\xi^2} \tag{2.34}$$

where ω_0 are undamped natural frequencies of the system, and ξ the accompanying modal damping ratios. The eigenvectors $\mathbf{V}_{A_c}$ appears as complex conjugate pairs of mode shapes, containing displacement and velocity amplitudes and phase angles.

The relationship between continuous-time and discrete-time models, established in equation (2.19), relates eigenvalues of $\mathbf{A}_c$ to eigenvalues of $\mathbf{A}_d$ by

$$\lambda_{A_c} = \frac{1}{\Delta t} \ln \lambda_{A_d} \tag{2.35}$$

The eigenvectors $\mathbf{V}_{A_c}$ are identical to $\mathbf{V}_{A_d}$.

2.3.2.4 Similarity transformation

As stated in section 2.3.1.4, the system can be transformed by a linear transformation of the state vector, i.e. a shift in basis. This implies that matrices recovered by identification only are one out of infinitely many possible solutions. Hence, if a system is represented by $\mathbf{A}_c^*$, $\mathbf{B}_c^*$ and $\mathbf{C}^*$, where * indicates one of infinitely many realisations of the system, corresponding matrices with the specific structure of $\mathbf{A}_c$ and $\mathbf{C}$ given in (2.27) can be found by a similarity transformation.

As stated in 2.3.1.2, the matrix pair $\{\mathbf{A}_c, \mathbf{C}\}$ is assumed to be observable, and when applied in (2.27), it has a minimum number of parameters. That is, it represents an *observability canonical realisation*, where the observability matrix equals the identity matrix:

$$\mathbf{Q}_o = \begin{bmatrix} \mathbf{C} \\ \mathbf{C}\mathbf{A}_c \end{bmatrix} = \mathbf{I} \tag{2.36}$$

If $\mathbf{A}_c^*$ and $\mathbf{C}^*$ are system matrices of a similar system, this renders

$$\mathbf{Q}_o = \begin{bmatrix} \mathbf{C}^* \\ \mathbf{C}^*\mathbf{A}_c^* \end{bmatrix} \mathbf{T} = \mathbf{I} \tag{2.37}$$

and the transformation matrix becomes

$$\mathbf{T}^{-1} = \begin{bmatrix} \mathbf{C}^* \\ \mathbf{C}^*\mathbf{A}_c^* \end{bmatrix} \tag{2.38}$$

It is here assumed that $\mathbf{A}_c^* \in \mathbb{R}^{2n \times 2n}$ and $\mathbf{C}^* \in \mathbb{R}^{n \times 2n}$, i.e. that $\mathbf{T}$ is a square matrix. Finally, the particular set of system matrices becomes

$$\mathbf{A}_c = \mathbf{T}^{-1}\mathbf{A}^*\mathbf{T} \tag{2.39a}$$

$$\mathbf{B}_c = \mathbf{T}^{-1}\mathbf{B}^* \tag{2.39b}$$

$$\mathbf{C} = \mathbf{C}^*\mathbf{T} \tag{2.39c}$$

$$\mathbf{D} = \mathbf{D}^* \tag{2.39d}$$

It can be shown that similarity transformation does not change the system estimate obtained by system identification [27].

Based on the expressions derived above, it is clear that identification of the continuous-time system matrix $\mathbf{A}_c$ gives the undamped natural frequencies, modal damping ratios and damped mode shapes. If the modal mass matrix $\mathbf{M}_0$ is known, the modal damping and stiffness matrix can also be recovered.

2.3.2.5 Normalisation

Excitation amplitudes of different modes in a system may vary with orders in magnitude, either because of loading, initial conditions or simply because of difference in physical units. Matrices containing elements widely spread in magnitude are often poorly conditioned with respect to the numerical operations performed by the identification methods [17]. Thus, a normalisation of the response data would be beneficial.

Normalisation may be introduced by the *normalisation matrix* $\mathbf{N} \in \mathbb{R}^{2n \times 2n}$, such that (2.29b) can be written

$$\tilde{\mathbf{y}}_k = \mathbf{N}\mathbf{y}_k = \mathbf{N}\mathbf{C}\mathbf{x}_k + \mathbf{N}\mathbf{v}_k \tag{2.40}$$

where $\tilde{\mathbf{y}}_k$ is the normalised response. If $\tilde{\mathbf{C}}$ is the output matrix identified based on the normalised response, the correct output matrix are then found by

$$\mathbf{C} = \mathbf{N}^{-1}\tilde{\mathbf{C}} \tag{2.41}$$

Hence, the transformation matrix given in (2.38) becomes

$$\mathbf{T}^{-1} = \begin{bmatrix} \mathbf{N}^{-1}\mathbf{C}^* \\ \mathbf{N}^{-1}\mathbf{C}^*\mathbf{A}_c^* \end{bmatrix} \tag{2.42}$$

and the correct system matrices are found by (2.39).

Hoen [17] suggest to normalise the response to zero mean and unit standard deviation, which also was adopted in identification performed in subsequent chapters.

2.3.3 Preliminary analysis

2.3.3.1 Spectral analysis

As a first step in the identification procedure, spectral analysis is a non-parametric method that may produce valuable information about the system [17]. The *power spectral density* $S(\omega)$ describes how the power of a signal time series is distributed with frequency. For a discrete signal with N samples, sampled at a rate f_s,

$$y_k = y(k/f_s), \quad k = 0, 1, 2, 3, \ldots, N \tag{2.43}$$

the double-sided power spectrum is given by

$$S(\pm f) = |Y(\pm f)|^2 \tag{2.44}$$

where the discrete Fourier transform Y is defined by [24]:

$$Y(f) = \frac{1}{N}\sum_{k=0}^{N-1} y_k e^{-i2\pi fk/N} \tag{2.45}$$

The total power of the signal is now given by

$$P = \int_{-\infty}^{\infty} S(\pm f)\,\mathrm{d}f = \int_{0}^{\infty} S(f)\,\mathrm{d}f \tag{2.46}$$

Since the double-sided spectrum $S(\pm\omega)$ is symmetric about $\omega = 0$, the single-sided spectrum $S(\omega)$ is given by

$$S(f) = 2S(\pm f) \tag{2.47}$$

It should be noted that the *DC component* of the spectral density, where $k = 0$, is unique and should not be multiplied by 2.

Figure 2.5 shows a noisy displacement record made up by three sine waves at 0.3, 0.7 and 1 Hz, sampled at 100 Hz. It is easy to see that the power spectrum provides useful information about the frequency characteristics of a system, as both the number of modes and natural frequencies are identified by the peaks of the spectrum.

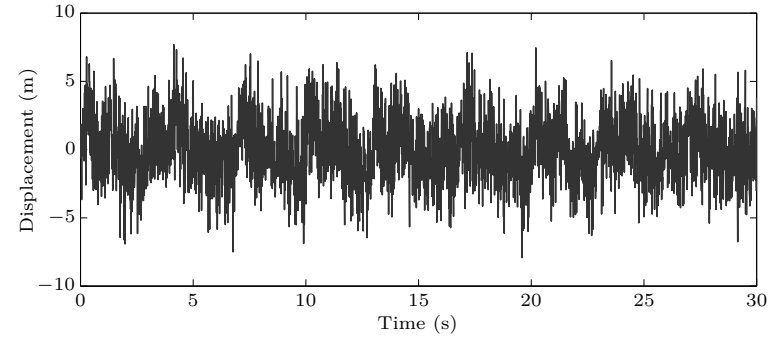

(a) Noisy displacement record

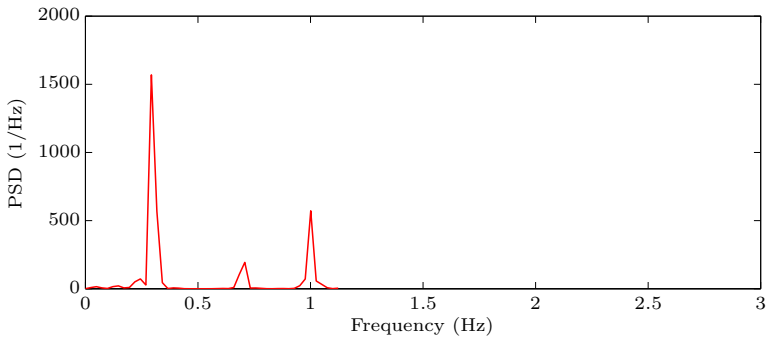

(b) Single-sided power spectrum

Figure 2.5: Power spectral density of noisy displacement record.

2.3.3.2 Logarithmic decrement

An estimate of the modal damping ratio is found by investigating the *logarithmic decrement* of the displacement record. Logarithmic decrement is the natural logarithm of the ratio of the amplitudes of two successive peaks:

$$\delta = \frac{1}{n} \ln \frac{y_k}{y_{k+n}} \tag{2.48}$$

where y_k is the amplitude of peak number k and y_{k+n} is the amplitude of the peak n periods away. The modal damping ratio is now given by

$$\zeta = \frac{1}{\sqrt{1 + \left(\frac{2\pi}{\delta}\right)^2}} \tag{2.49}$$

2.3.4 Covariance Block Hankel Matrix (CBHM) identification

The *covariance block Hankel matrix* method is a parametric system identification method based on the *Markov block Hankel matrix* (MBH) method, developed through the work of Ho and Kalman [16], Staar [46], Moore [34] and Gawronski and Natke [11], who considered the case where both the excitation and response data are available.

Aoki [2] and Henriksen [14] developed a modification of the MBH method, where the Markov parameters were replaced by response covariance estimates. Hoen [17] extensively tested the CBHM method by analysing both simulated and measured response data of a deep-water offshore platform to obtain modal frequencies and damping ratios. Jakobsen [20] extended the work of Hoen to recover full structural system matrices of a structure exposed to natural wind.

The derivation of the method presented in the following is based on the work of Jakobsen and Hoen. The expression

$$\mathbf{C}_{yy}(k+m,k) = \frac{1}{N} \sum_{k=1}^{N-k} \mathbf{y}_{k+m} \mathbf{y}_k^{\mathrm{T}} \tag{2.50}$$

where N is the number of output samples, is a consistent but biased estimate of the output covariance matrix $\mathbf{C}_{yy}(k+m,k)$ [20] at time lag m, defined by

$$\mathbf{C}_{\mathbf{yy}}(k+m,k) = \mathrm{E}\left[\mathbf{y}_{k+m} \mathbf{y}_k^{\mathrm{T}}\right] \tag{2.51}$$

where $\mathbf{C}_{\mathbf{yy}}(k+m,k) \in \mathbb{R}^{n \times n}$. For the system described in (2.29), which is driven by a white noise process, the following expression is obtained by inserting (2.32) into (2.51):

$$\mathbf{C}_{yy}(k+m,k) = \mathbf{C}\mathbf{A}_d^{m-1} \left[\mathbf{A}_d \mathbf{C}_{\mathbf{xx}}(k,k)\mathbf{C}^{\mathrm{T}} + \mathbf{B}_d \mathbf{C}_{\mathbf{pv}}(k,k)\right] \tag{2.52}$$

where $\mathbf{C_{xx}}(k,k) \in \mathbb{R}^{2n\times 2n}$ is the state vector covariance matrix and $\mathbf{C_{pv}}(k,k) \in \mathbb{R}^{n\times n}$ is the load-measurement noise cross-covariance matrix defined in (2.30). It is in the following assumed that $\mathbf{p}$ and $\mathbf{v}$ are stationary processes, i.e.

$$\mathbf{C_{xx}}(k,k) = \mathbf{C_{xx}} \quad \text{and} \quad \mathbf{C_{pv}}(k,k) = \mathbf{C_{pv}}$$

By introducing

$$\mathbf{M} = \mathbf{A}_d\mathbf{C_{xx}}\mathbf{C}^{\mathrm{T}} + \mathbf{B}_d\mathbf{C_{pv}} \tag{2.53}$$

into (2.52), we get

$$\mathbf{C}_{yy}(k+m,k) = \mathbf{C}\mathbf{A}_d^{m-1}\mathbf{M} \tag{2.54}$$

Hence, the identification consists of a suitable decomposition of the covariance estimate $\mathbf{C}_{yy}(k+m,k)$. The decomposition is performed indirectly on a *block Hankel* matrix, where the blocks are the covariance estimates given above. Introducing the simplified notation $\mathbf{C}_{\mathbf{y}(k)}(m)$ to replace $\mathbf{C_{yy}}(k+m,k)$, the covariance block Hankel matrix is given by

$$\mathbf{H}_1(l) = \begin{bmatrix} \mathbf{C}_{\mathbf{y}(k)}(1) & \mathbf{C}_{\mathbf{y}(k)}(2) & \cdots & \mathbf{C}_{\mathbf{y}(k)}(l) \\ \mathbf{C}_{\mathbf{y}(k)}(2) & \mathbf{C}_{\mathbf{y}(k)}(3) & \cdots & \mathbf{C}_{\mathbf{y}(k)}(l+1) \\ \vdots & \vdots & \ddots & \vdots \\ \mathbf{C}_{\mathbf{y}(k)}(l) & \mathbf{C}_{\mathbf{y}(k)}(l+1) & \cdots & \mathbf{C}_{\mathbf{y}(k)}(2l-1) \end{bmatrix} \tag{2.55}$$

where $\mathbf{H}_1(l) \in \mathbb{R}^{nl\times nl}$, and the number of covariance lags l corresponds to the maximum order of the state space model. Therefore, the number of lags should be large enough to encompass the largest realistic dimension of the state vector, i.e. $l \geq 2n$ – and in any case the number of lags should correspond to at least one period of oscillation [17]. The procedure outlined in the following is also valid when the covariance matrices are replaced by the Markov parameters defined in (2.33) [17].

Inserting (2.54) into (2.55) gives

$$\mathbf{H}_1(l) = \begin{bmatrix} \mathbf{C}\mathbf{M} & \mathbf{C}\mathbf{A}_d\mathbf{M} & \cdots & \mathbf{C}\mathbf{A}_d^{l-1}\mathbf{M} \\ \mathbf{C}\mathbf{A}_d\mathbf{M} & \mathbf{C}\mathbf{A}_d^{2}\mathbf{M} & \cdots & \mathbf{C}\mathbf{A}_d^{l}\mathbf{M} \\ \vdots & \vdots & \ddots & \vdots \\ \mathbf{C}\mathbf{A}_d^{l-1}\mathbf{M} & \mathbf{C}\mathbf{A}_d^{l}\mathbf{M} & \cdots & \mathbf{C}\mathbf{A}_d^{2l-2}\mathbf{M} \end{bmatrix} \tag{2.56}$$

A block Hankel matrix can be expressed as a product of two matrices:

$$\mathbf{H}_1(l) = \mathbf{Q}_o(l)\mathbf{Q}_c(l) \tag{2.57}$$

where $\mathbf{Q}_o(l)$ is the observability matrix and $\mathbf{Q}_c(l)$ is the controllability matrix of the system:

$$\mathbf{Q}_o(l) = \begin{bmatrix} \mathbf{C} & \mathbf{C}\mathbf{A}_d & \mathbf{C}\mathbf{A}_d^2 & \cdots & \mathbf{C}\mathbf{A}_d^{l-1} \end{bmatrix}^{\mathrm{T}} \tag{2.58}$$

$$\mathbf{Q}_c(l) = \begin{bmatrix} \mathbf{M} & \mathbf{A}_d\mathbf{M} & \mathbf{A}_d^2\mathbf{M} & \cdots & \mathbf{A}_d^{l-1}\mathbf{M} \end{bmatrix} \tag{2.59}$$

An m-shifted version of the block Hankel matrix is defined by

$$\mathbf{H}_m(l) = \begin{bmatrix} \mathbf{C}_{\mathbf{y}(k)}(m) & \mathbf{C}_{\mathbf{y}(k)}(m+1) & \cdots & \mathbf{C}_{\mathbf{y}(k)}(m+l-1) \\ \mathbf{C}_{\mathbf{y}(k)}(m+1) & \mathbf{C}_{\mathbf{y}(k)}(m+2) & \cdots & \mathbf{C}_{\mathbf{y}(k)}(m+l) \\ \vdots & \vdots & \ddots & \vdots \\ \mathbf{C}_{\mathbf{y}(k)}(m+l-1) & \mathbf{C}_{\mathbf{y}(k)}(m+l) & \cdots & \mathbf{C}_{\mathbf{y}(k)}(m+2l-2) \end{bmatrix} \tag{2.60}$$

The shifted version can also be expressed in terms of the observability and controllability matrices:

$$\mathbf{H}_m(l) = \mathbf{Q}_o(l)\mathbf{A}_d^{m-1}\mathbf{Q}_c(l) \tag{2.61}$$

Another decomposition of $\mathbf{H}_1(l)$ is also possible:

$$\mathbf{H}_1(l) = \mathbf{P}\mathbf{R} \tag{2.62}$$

where $\mathbf{P} \in \mathbb{R}^{nl \times r}$ and $\mathbf{R} \in \mathbb{R}^{r \times nl}$, r being the rank of $\mathbf{H}_1(l)$. The corresponding pseudoinverse of $\mathbf{H}_1(l)$ is given by

$$\mathbf{H}_1^+(l) = \mathbf{P}^+\mathbf{R}^+ \tag{2.63}$$

where $\mathbf{P}^+\mathbf{P} = \mathbf{I}$ and $\mathbf{R}^+\mathbf{R} = \mathbf{I}$. Gawronski and Natke [11] proved the following decomposition of a m-shifted block Hankel matrix:

$$\mathbf{H}_m(l) = \mathbf{P}\left[\mathbf{P}^+\mathbf{Q}_o(l)\mathbf{A}_d\mathbf{Q}_c(l)\mathbf{R}^+\right]^{m-1}\mathbf{R} \tag{2.64}$$

Introducing the mask matrix

$$\mathbf{E}_n = \begin{bmatrix} \mathbf{I}_n & \mathbf{0} & \mathbf{0} & \cdots & \mathbf{0} \end{bmatrix}^{\mathrm{T}} \tag{2.65}$$

where $\mathbf{E}_n \in \mathbb{R}^{nl \times n}$, enables the extraction of the covariance matrix $\mathbf{C}_{\mathbf{y}(k)}(m)$:

$$\mathbf{C}_{\mathbf{y}(k)}(m) = \mathbf{E}_n^{\mathrm{T}}\mathbf{P}\left[\mathbf{P}^+\mathbf{Q}_o(l)\mathbf{A}_d\mathbf{Q}_c(l)\mathbf{R}^+\right]^{m-1}\mathbf{R}\mathbf{E}_n \tag{2.66}$$

Comparison with (2.54) and (2.64) now renders

$$\mathbf{A}_d = \mathbf{P}^+\mathbf{H}_2(l)\mathbf{R}^+ \tag{2.67a}$$

$$\mathbf{C} = \mathbf{E}_n^{\mathrm{T}}\mathbf{P} \tag{2.67b}$$

$$\mathbf{M} = \mathbf{R}\mathbf{E}_n \tag{2.67c}$$

According to (2.67), only $\mathbf{H}_1(l)$ and $\mathbf{H}_2(l)$ are needed to estimate the matrices $\mathbf{A}_d$, $\mathbf{C}$ and $\mathbf{M}$, but $\mathbf{H}_1(l)$ still has to be factorised according to (2.62). One possibility, suggested by e.g. Aoki [2] and Hoen [17], is the robust *singular value decomposition* (SVD):

$$\mathbf{H}_1(l) = \mathbf{U}\boldsymbol{\Gamma}^2\mathbf{V}^{\mathrm{T}} \tag{2.68}$$

where $\mathbf{U} \in \mathbb{R}^{nl \times nl}$ and $\mathbf{V} \in \mathbb{R}^{nl \times nl}$ are orthogonal matrices, such that $\mathbf{U}\mathbf{U}^{\mathrm{T}} = \mathbf{I}$ and $\mathbf{V}^{\mathrm{T}}\mathbf{V} = \mathbf{I}$. If $\mathbf{P}$ and $\mathbf{R}$ are chosen as

$$\mathbf{P} = \mathbf{U}\boldsymbol{\Gamma}, \quad \mathbf{P}^{+} = \boldsymbol{\Gamma}^{-1}\mathbf{U}^{\mathrm{T}} \tag{2.69a}$$

$$\mathbf{R} = \boldsymbol{\Gamma}\mathbf{V}^{\mathrm{T}}, \quad \mathbf{R}^{+} = \mathbf{V}\boldsymbol{\Gamma}^{-1} \tag{2.69b}$$

and a suitable number of singular values are included in the decomposition, an *internally balanced realisation* is recovered [17,20]. An internally balanced realisation is a minimal realisation which is equally controllable and observable. The number of singular values to include, and hence the choice of model order, is discussed in section 2.3.6.

The matrices given in (2.67) now become

$$\mathbf{A}_d^* = \boldsymbol{\Gamma}^{-1}\mathbf{U}^{\mathrm{T}}\mathbf{H}_2(l)\mathbf{V}\boldsymbol{\Gamma}^{-1} \tag{2.70a}$$

$$\mathbf{C}^* = \mathbf{E}_n^{\mathrm{T}}\mathbf{U}\boldsymbol{\Gamma} \tag{2.70b}$$

$$\mathbf{M}^* = \boldsymbol{\Gamma}\mathbf{V}^{\mathrm{T}}\mathbf{E}_n \tag{2.70c}$$

where the asterisk stress that this is one of infinitely many solutions; i.e. they are only determined up to a similarity transformation. Eigenvalues are invariant with respect to similarity transformations, and an eigendecomposition of $\mathbf{A}_d^*$ gives

$$\mathbf{A}_d^* = \mathbf{V}_{\mathbf{A}_d^*}\boldsymbol{\Lambda}_{\mathbf{A}_d^*}\mathbf{V}_{\mathbf{A}_d^*}^{-1} \tag{2.71}$$

The eigenvalues of $\mathbf{A}_c^*$ are now given by (2.35):

$$\lambda_{\mathbf{A}_c^*} = \frac{1}{\Delta t}\ln\lambda_{\mathbf{A}_d^*} \tag{2.72}$$

and since $\mathbf{V}_{\mathbf{A}_c^*} = \mathbf{V}_{\mathbf{A}_d^*}$, a matrix similar to the particular matrix $\mathbf{A}_c$ is given by

$$\mathbf{A}_c^* = \mathbf{V}_{\mathbf{A}_d^*}\boldsymbol{\Lambda}_{\mathbf{A}_c^*}\mathbf{V}_{\mathbf{A}_d^*}^{-1} \tag{2.73}$$

Finally, the linear, time-invariant state space system matrix in continuous time is found by (2.39) and (2.42):

$$\mathbf{A}_c = \mathbf{T}^{-1}\mathbf{A}_c^*\mathbf{T}, \quad \mathbf{T}^{-1} = \begin{bmatrix} \mathbf{N}^{-1}\mathbf{C}^* \\ \mathbf{N}^{-1}\mathbf{C}^*\mathbf{A}_c^* \end{bmatrix} \tag{2.74}$$

It should be noted that if the order of the estimated state space model, here represented by $\mathbf{A}_c^*$, is higher than $2n$, this transformation is not a true similarity transformation. It is rather a similarity transformation of a *truncated* internally balanced realisation, where state variables corresponding to orders higher than $2n$ have been discarded [17]. This corresponds to truncation of the SVD, which will be further discussed in section 2.3.6.

2.3.5 Subspace State Space System Identification (N4SID)

Subspace identification methods constitute a fairly new class of parametric identification methods. The mathematical framework, as we know it today, was mainly established by Van Overschee and De Moor [52–54], where both deterministic and stochastic estimation algorithms were unified by applying general mathematical tools. Larimore [25, 26], Verhaegen [55] and Verhaegen and Dewilde [56] and also developed related ideas in their work on the combined deterministic-stochastic identification problem. It has been used by e.g. Boonyapinyo and Janesupasaeree [3] to identify aerodynamic derivatives.

Subspace methods translate the constructions of stochastic realisation theory into procedures for model building which work on measured data. The basic objects which are constructed in the algorithms are subspaces generated by the data, and mathematical geometric operations, such as orthogonal and oblique projections, are all that is needed to estimate the system parameters, i.e. the system matrices [9].

There are several important differences between subspace methods and more classical identification methods. First, the only parameter provided by the user is the model order, which can be determined by inspection of the singular values from the SVD performed by the method. Choice of model order is discussed in detail in the next section. Second, subspace methods do not require iterative optimisation, only simple and robust tools of linear algebra, like QR and SVD decompositions, are used. Hence, there are no convergence problems.

If a subspace identification method is applied to a system driven by a stochastic process, the estimation algorithm is essentially similar to the *covariance-driven* CBHM method described above [4]. The major difference is that the covariance estimates are replaced by a projection of the row space of future outputs onto the row space of past outputs, computed by QR-factorisation [3]. Thus, it is a so-called *data-driven* method. Another important difference is the introduction of left and right weighting matrices in the SVD [27]. In terms of the CBHM method, this corresponds to a pre- and post-multiplication of $\mathbf{H}_1(l)$, such that

$$\mathbf{H}_1(l) = \mathbf{W}_1^{-1}\mathbf{U}\boldsymbol{\Gamma}^2\mathbf{V}^{\mathrm{T}}\mathbf{W}_2^{-1} \tag{2.75}$$

where $\mathbf{W}_1$ and $\mathbf{W}_2$ are the left and right weighting matrix, respectively. This renders

$$\mathbf{P} = \mathbf{W}_1^{-1}\mathbf{U}\boldsymbol{\Gamma}, \quad \mathbf{P}^{+} = \boldsymbol{\Gamma}^{-1}\mathbf{U}^{\mathrm{T}}\mathbf{W}_1 \tag{2.76a}$$

$$\mathbf{R} = \boldsymbol{\Gamma}\mathbf{V}^{\mathrm{T}}\mathbf{W}_2^{-1}, \quad \mathbf{R}^{+} = \mathbf{W}_2\mathbf{V}\boldsymbol{\Gamma}^{-1} \tag{2.76b}$$

The weighting matrices is the main factor that differentiates various implementation of the method.

The subspace algorithm will not be derived in this paper, as it's complex theoretical background are outside the scope of work. It is, however, a powerful and robust class of identification methods, and the *N4SID* algorithm by Van Overschee and De Moor [53]

implemented in the *System Identification Toolbox* [28, 32] in MATLAB will be used for enhanced confidence in the identification results.

The MATLAB implementation gives the system matrix $\mathbf{A}_c^*$ and the output matrix $\mathbf{C}^*$. To obtain the system matrix structure given in (2.29), the now familiar transformation

$$\mathbf{A}_c = \mathbf{T}^{-1}\mathbf{A}_c^*\mathbf{T}, \quad \mathbf{T}^{-1} = \begin{bmatrix} \mathbf{N}^{-1}\mathbf{C}^* \\ \mathbf{N}^{-1}\mathbf{C}^*\mathbf{A}_c^* \end{bmatrix} \tag{2.77}$$

is applied. As noted in 2.3.4, any state variable corresponding to orders higher than $2n$ is truncated.

2.3.6 Model order

For parametric identification methods, the model order plays an important role.

The singular values γ of the block Hankel matrix $\mathbf{H} \in \mathbb{R}^{nl \times nl}$ gives information about the effective rank of the system. If, for some order $r < nl$, the singular values are such that $\gamma_r \gg \gamma_{r+1}$, then the state variables $x_i, i = r+1, r+2, \ldots, nl$ of the balanced system are either almost not observable, almost not controllable or almost neither observable nor controllable at the same time [17]. Therefore, the system can be reduced to order r by deleting the state variables $x_i, i = r+1, r+2, \ldots, nl$, resulting in a model with state variables that are equally observable and controllable.

The singular values of the system estimated by using a filtered version of the noisy displacement signal from Figure 2.5, is plotted in Figure 2.6. Filtering of signals will be treated in section 2.4. From the plot in Figure 2.6a, the model order is not evident, but the plot of relative singular values in Figure 2.6b makes it clear that an equally observable and controllable state space model should be of order six. This agrees well with the power spectrum in Figure 2.5, where it is evident that the displacement comprises three modes. Since the state vector contains both displacement and velocities, this gives an order of six.

To gain further confidence in the choice of order, estimated natural frequencies can be plotted against model order. This is done in Figure 2.7, where the frequencies found by spectral analysis in Figure 2.5 are indicated by vertical lines. The importance of selecting the correct order is emphasised, as frequencies are missing and/or incorrect for lower orders, and spurious frequencies occur for higher orders.

2.4 Signal processing

To enhance system identification based on experimental recordings, it may be beneficial to preprocess the data. All data processing, in the following referred to as *signal*

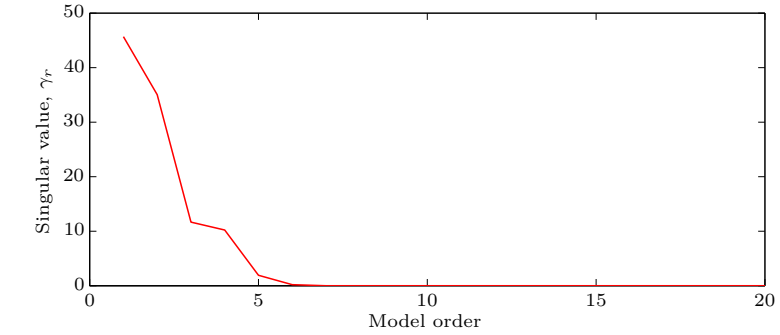

(a) Singular values

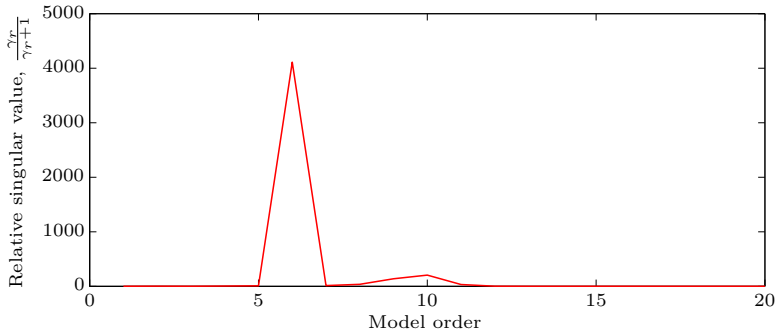

(b) Relative singular values

Figure 2.6: Singular values obtained by the CBHM method.

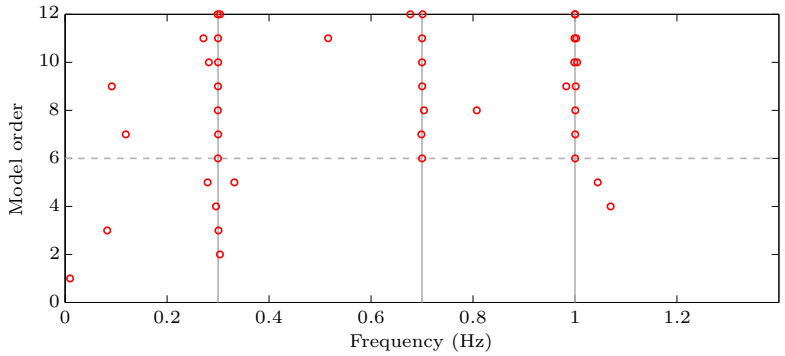

Figure 2.7: Natural frequencies estimated by the CBHM method for increasing model order.

processing, is in the context of this work performed with MATLAB [30]. The reader is referred to e.g. [35], [45] and [18] for further studies on the subject.

2.4.1 Noise and disturbances

Noise is random fluctuations more or less inherent in any electrical signal. It may stem from many sources, ranging from fundamental electrical sources on molecule level to mechanical sources on macro level. The sources of electrical noise are outside the scope of this work, but an important mechanical disturbance source is resonance in secondary components of the experimental setup, e.g. springs and load cells.

Throughout this paper, an assumption of stationary Gaussian white measurement noise is adopted, which implies that the noise has zero mean, no autocorrelation and a flat power spectrum. Since the frequency content of a signal does not comprise frequencies higher than the sampling rate, sampling rate of recorded measurements should be high enough to justify this assumption. However, if e.g. spring resonance is present, the noise may be *coloured* by mechanical disturbances, i.e. the power spectrum is not flat. This is circumvented by low-pass filtering, discussed below.

A common measure of noise is the *signal-to-noise ratio* (SNR), which is defined as the ratio of signal power to the noise power:

$$\text{SNR} = \frac{P_{\text{signal}}}{P_{\text{noise}}} \tag{2.78}$$

where P is the average power. For a discrete-time signal

$$\mathbf{y} = \begin{bmatrix} y_1 & y_2 & y_3 & \cdots & y_N \end{bmatrix}^{\text{T}}$$

power is defined as energy per sample [44], i.e.

$$P_y = \frac{1}{N}\mathbf{y}^{\text{T}}\mathbf{y} \tag{2.79}$$

In this paper, the counterpart of SNR, *noise-to-signal ratio* (RNS), will be used as a measure of noise:

$$\text{SNR} = \frac{P_{\text{noise}}}{P_{\text{signal}}} \tag{2.80}$$

A clean signal contaminated with noise to obtain 10 % RNS is shown in Figure 2.8. The sampling rate is 100 Hz.

2.4.2 Detrending

In most cases, only the fluctuations of a signal is interesting. Detrending is simply to subtract the mean or a best fit line from the signal, to ensure that it has zero mean.

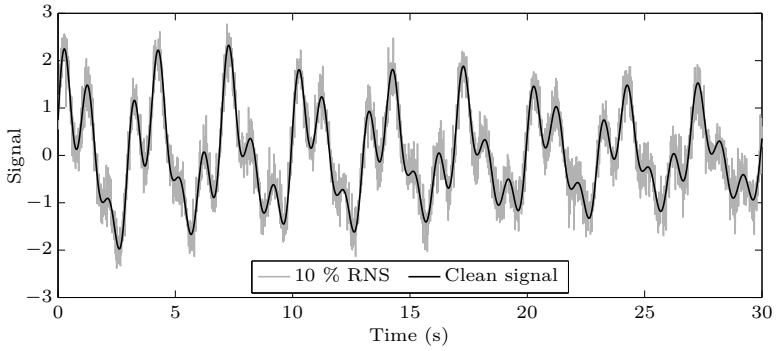

Figure 2.8: Signal with 10 % RNS.

In the context of structural response to wind, the static part of the response renders a non-zero mean (trend) of the signal. However, linear trends may also stem from e.g. sensor drift.

The system identification methods presented herein only produce correct results if the signal has zero mean.

2.4.3 Low-pass filtering

The vibration frequencies of structural systems focused on in this paper are low; usually only a small fraction of the Nyquist frequency. Hence, applying a low pass filter with an appropriate cutoff frequency will cancel a major part of the (high frequency) noise, including any resonance in secondary components. Even though the white noise assumption no longer will be valid, the remaining noise will be negligible for most practical purposes. However, care must always be taken when manipulating experimental data.

A low-pass filter attenuates the frequency content above a *cutoff frequency*, the *stopband*, while the frequency content below it, the *passband*, ideally stays unchanged. The cutoff frequency is determined based on e.g. spectral analysis, as described in section 2.3.3. There are several types of low-pass filters available, but some of the most common are Butterworth filters and Chebyshev filters. Both are recursive filters, for which the filtering process is defined by

$$\begin{aligned} y_k = a_0 x_k + a_1 x_{k-1} + a_2 x_{k-2} + a_3 x_{k-3} + \cdots \\ + b_1 y_{k-1} + b_2 y_{k-2} + b_3 y_{k-3} + \cdots \end{aligned} \tag{2.81}$$

where y_k is sample number k of the filtered signal and x_k is sample number k of the original signal [45]. The filter itself is simply a set of a and b-coefficients. The order of the filter, n, is the number of time shifts included in the recursive process. Hence, the coefficients written out in (2.81) constitutes a third order filter.

The frequency response of Butterworth filters is maximally flat in the passband, i.e. there are no ripples, but the *roll-off* is quite slow and the gain is -3 dB at the cutoff frequency. The Chebyshev Type I filters, however, allow ripples in the passband to achieve a faster roll-off near the cutoff frequency [45], illustrated in Figure 2.9.

It is obvious that the low ripple Chebyshev Type I filter is well suited if a sharp transition between the passband and the stopband is desired. However, in some cases it may not be desirable, and a Butterworth filter may be more suitable.

The phase response is also important, as non-zero phase response shifts and distorts the filtered signal. Hoen [17] emphasises that introduction of different phase distortion in different response channels can cause trouble in the interpretation of a system identification. Figure 2.10 shows that the phase response of the filters indeed are non-zero, but this problem is neatly overcome by filtering the signal twice; first forwards and then backwards. The magnitude of the frequency response is the same in both directions, but phases are of opposite sign. Thus, when the two directions are combined, the phase shifts cancel to zero and the frequency response is squared, effectively doubling the order of the filter [45].

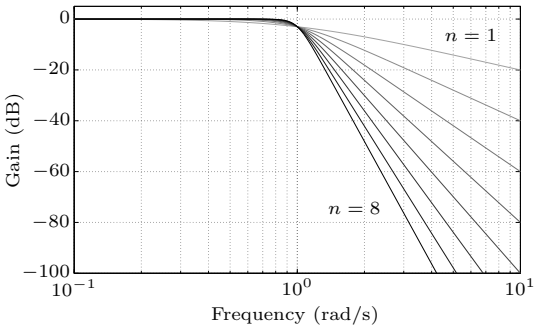

(a) Butterworth filter

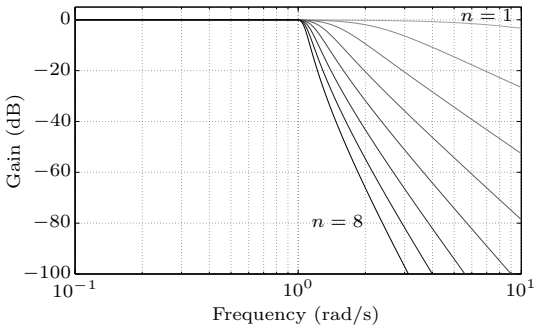

(b) Chebyshev Type I filter (0.05 dB ripple)

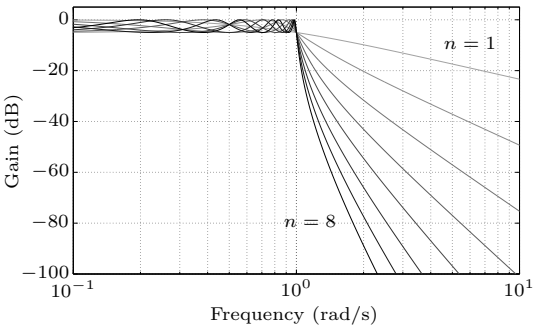

(c) Chebyshev Type I filter (5 dB ripple)

Figure 2.9: Magnitude of transfer functions of Butterworth and Chebyshev Type I filters of order 1-6, with a cutoff frequency of 1 rad/s.

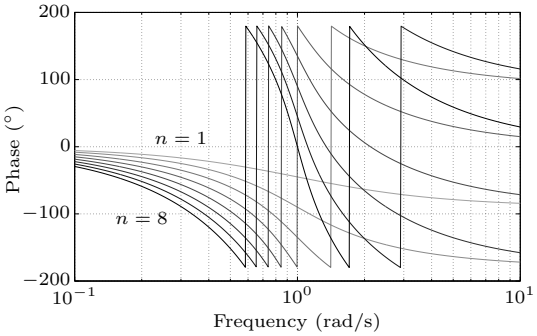

(a) Butterworth filter

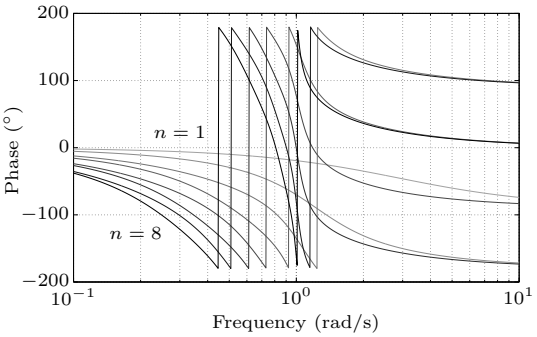

(b) Chebyshev Type I filter (0.05 dB ripple)

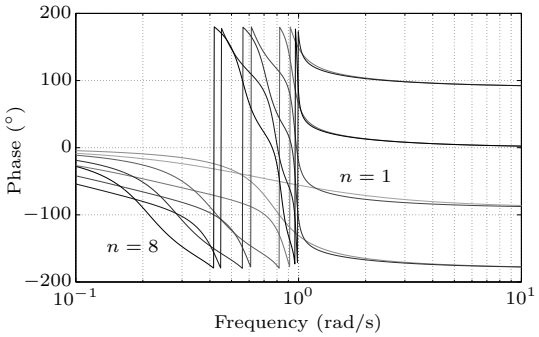

(c) Chebyshev Type I filter (5 dB ripple)

Figure 2.10: Phase response of Butterworth and Chebyshev Type I filters of order 1-6, with a cutoff frequency of 1 rad/s.

Bidirectional zero-phase filtering is compared to conventional filtering in Figure 2.11. The input signal is the contaminated signal from Figure 2.8. Several important aspects should be noted. First of all, the signal is heavily shifted by conventional filtering, and second, edge effects are evident. This is because the MATLAB procedure used to filter the signal assumes that all values before and after the given time series are zero. Edge effects might be overcome by applying a "windowing" method, where only a portion of the time series is retained after filtering. Finally, it is observed that even though the cutoff frequency is as low as 1.1 Hz, the attenuation of the harmonic at 1 Hz is negligible.

The details of the filters are outside the scope of this paper, but may be studied further in e.g. [45] and [35].

2.4.4 Resampling

For most identification methods, it is important that the sampling rate is optimal with respect to the dynamic content of the response. If the signal has no significant compo-

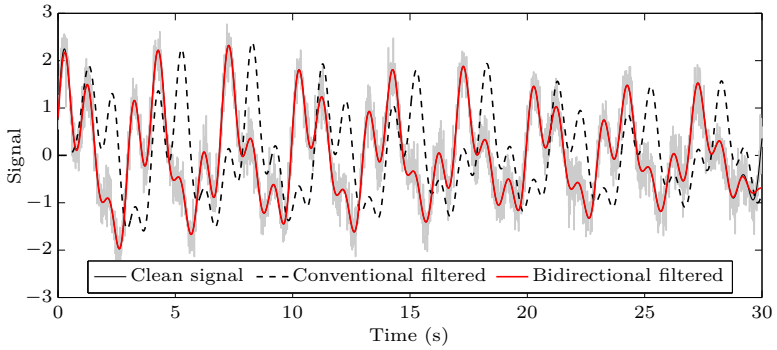

Figure 2.11: Bidirectional filtering vs. conventional filtering with a Chebyshev Type I filter with an effective order of 8 and a cutoff frequency of 1.1 Hz.

nents above a frequency that is an integer factor of the Nyquist frequency, the signal should be *decimated*, i.e. resampled to a lower frequency [17]. The reason for this is that only two samples per period are necessary to completely determine an harmonic component; more samples do not enhance identification of high-frequency components, but may distort estimation of low-frequency components because of numerical problems, model over-fitting and high sensitivity during conversion of discrete poles to continuous poles [27]. However, in the same way a cutoff frequency must be carefully chosen, a new sampling rate must also be chosen with care.

A proper decimation is a two-step process which comprises low-pass filtering and down-sampling. The default decimation implementation in the *Signal Processing Toolbox* in MATLAB R2012a applies an 8^{th} order Chebyshev Type I filter with 0.05 dB passband ripple through bidirectional filtering, implying an effective order of 16, before the signal is resampled by discarding samples from the smoothed signal. The cutoff frequency of the low-pass filter is 40 % of the new sampling frequency [31].

Decimation of the noisy signal from Figure 2.8 is shown in Figure 2.12. The original sampling rate is 100 Hz, giving a Nyquist frequency of 50 Hz, and the highest frequency component of the signal is 1 Hz. Decimation to 5 Hz then implies a cutoff frequency of 2 Hz, while decimation to 10 Hz implies a cutoff frequency of 4 Hz. It is seen that the decimated signals are approximately equal to the original signal, i.e. periods are preserved and no phase shift is present.

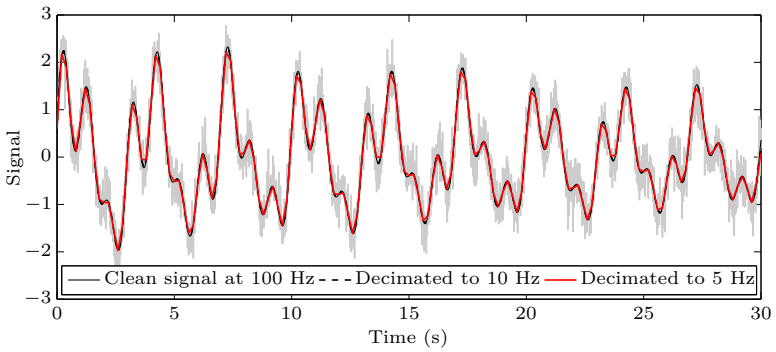

(a) Decimated signal

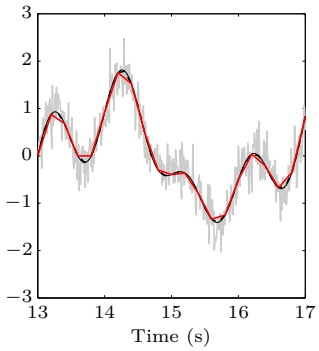

(b) Small "window" of signal

Figure 2.12: Decimation of signal

3 Design and experimental setup

The prototype of the suspension rig is based on a traditional setup where the section model is suspended in wires. It is designed for testing in still air, rather than in a wind tunnel, since the present work focus on investigation of non-linear effects due to the horizontal degree of freedom.

Since no aerodynamic properties are to be determined, it is not strictly necessary to use a correctly scaled model. Nevertheless, to ensure short transition to wind tunnel testing, a scale model of the Hardanger Bridge was made.

3.1 Model scaling

3.1.1 Geometry

Information about the geometric shape of the Hardanger Bridge is found in the design basis [48]; see Figure 3.13 and Table 3.2. The geometric scale is set to $\lambda = 1/50$, since it is the scale used in the wind tunnel report that was prepared during the design process of the bridge [50].

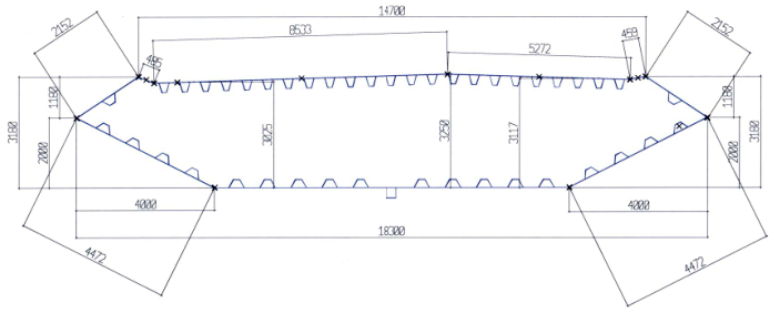

Figure 3.13: Geometry of the Hardanger Bridge [48].

Quantity		Full scale	Model scale (λ=1/50)
Full length	L_{full}	1310 m	26.2 m
Cross section width	B	18.3 m	0.366 m
Cross section depth	D	3.25 m	0.065 m
Centre of gravity	CG_z	1.953 m	0.039 m
Shear centre	SC_z	1.759 m	0.035 m

Table 3.2: Basic geometry dimensions of the Hardanger Bridge. The positions of CG and SC are given by distance from the bottom of the cross section, and their x-coordinates are approximately in the middle.

Drag	C_D	0.69
Lift	C_L	-0.20
Moment	C_M	-0.02
Drag slope at $\alpha = 0°$	$\mathrm{d}C_D/\mathrm{d}\alpha$	0.00
Lift slope at $\alpha = 0°$	$\mathrm{d}C_L/\mathrm{d}\alpha$	4.30
Moment slope at $\alpha = 0°$	$\mathrm{d}C_M/\mathrm{d}\alpha$	1.45

Table 3.3: Static load coefficients of the Hardanger Bridge. Coefficient slopes are determined as the largest slope in the incident angle interval $-6°$ to $6°$.

The static load coefficients of are also found in the design basis, but are there modified to include the effect of hangers and suspension cables – which are not included in the section model. However, they are based on the coefficients provided by the wind tunnel report, which will be adopted herein. More specifically, the adopted coefficients, given in Table 3.3, are obtained without vortex mitigation devices, and with the cycle path downstream.

The section model in the present study will not include all features that was included in the wind tunnel tests, e.g. railings and mitigation devices, but the coefficients should still be representative. Their use is in any case restricted to Monte Carlo simulations of the buffeting response (see Appendix B).

3.1.2 Mass

Equivalent distributed modal mass and moment of inertia of the bridge are given in [47, 48, 50], however with minor differences in the values. Since the natural frequencies will be taken from the ALVSAT report [47], the mass data given in Table 3.4 has also been taken from this report.

Quantity	Full scale	Model scale (λ=1/50)
Distributed mass	13,100 kg/m	5.240 kg/m
Distributed moment of inertia	434,000 kg·m^2/m	0.0694 kg·m^2/m

Table 3.4: Equivalent distributed mass and moment of inertia of the Hardanger Bridge.

3.1.3 Natural frequencies

The natural frequencies given in Table 3.5 are taken from the ALVSAT report, and corresponds to the lowest *symmetric* horizontal, vertical and torsional modes.

Scaling of frequencies depends on both geometric scaling and scaling of wind velocities. The critical (flutter) mean wind velocity reported in [50] is $V_{cr} \approx 70$ m/s. Thus, by setting the velocity scale factor $\nu = 1/4$, this corresponds to a mean wind velocity of 17.5 m/s in the wind tunnel, which is a suitable velocity in the tunnel at NTNU.

At high wind velocities, motion induced aerodynamic stiffness alters the natural frequencies of the section model. If two or more frequencies are closing in on each other, the corresponding modes begin to couple, possibly leading to instability of the system (e.g. flutter). To model this effect correctly, it is important to maintain the ratios between relevant frequencies. Even so, to understand the system's sensitivity to frequency ratios, it would be beneficial to determine the properties for a deviations in the estimated ratios.

Mode		Full scale	Model scale (λ=1/50, $\nu = 1/4$)
Horizontal	f_p	0.0506 Hz	0.6325 Hz
Vertical	f_h	0.1416 Hz	1.7700 Hz
Torsional	f_α	0.3510 Hz	4.3875 Hz

(a) Natural frequencies

Modes	Ratio
Torsional to vertical	2.48
Torsional to horizontal	6.94
Vertical to horizontal	2.80

(b) Frequency ratios

Table 3.5: Natural frequencies of the lowest symmetric modes of the Hardanger Bridge.

3.2 Prototype design

The prototype is intended for measuring free vibration response of the section model in still air, and will not be installed in a wind tunnel. It will, however, be designed to allow a potential installation in the wind tunnel at NTNU to be as simple as possible.

The design turned out to be an iterative process, because the choice of one design parameter often affect several others. Particularly, the selection of springs constituted a challenge, as each spring has to match a set of criteria depending on other springs used in the model. Hence, changing one spring may render the choice of other springs incorrect.

Findings regarding this and other important parameters are discussed in the following.

3.2.1 Conceptual sketch

A sketch of the final suspension rig setup is shown in Figure 3.14. The section model, including a setup at each end to allow attachment of wires, is suspended in wires attached to one or two extension springs in series. A wire and the corresponding spring series will in the following be referred to as a *suspension*. All together, there are twelve suspensions, which may be grouped into six suspension *pairs*; four vertical and two horizontal. Each pair is attached to a load cell at one end, and a hook at the other end. The load cell measure the tensile force in the spring attached to it, which may be used to estimate the deflection of the suspension. The motion of the section model can then be obtained by simple calculations.

The torsional stiffness of the section model can easily be altered changing the distance between the vertical wires.

3.2.2 Practical considerations

3.2.2.1 Wind tunnel

Considering future work with the experimental setup developed in this thesis, it is important that the suspension rig can be installed and tested in the wind tunnel at NTNU. The largest wind tunnel in the Aerodynamic Laboratory has a test section of 2.7 m width, 1.8 m height and 11 m length, and a maximum velocity of 30 m/s. There are currently no system to generate turbulence. The exterior of the tunnel is shown in Figure 3.15, where the orange part is the test section. The wooden frame attached to the test section, shown in Figure 3.15b, has previously been used to mount a traditional two-degree-of-freedom suspension setup, but is currently not being used. Installation of the setup investigated herein would require a new, considerably larger frame to reduce

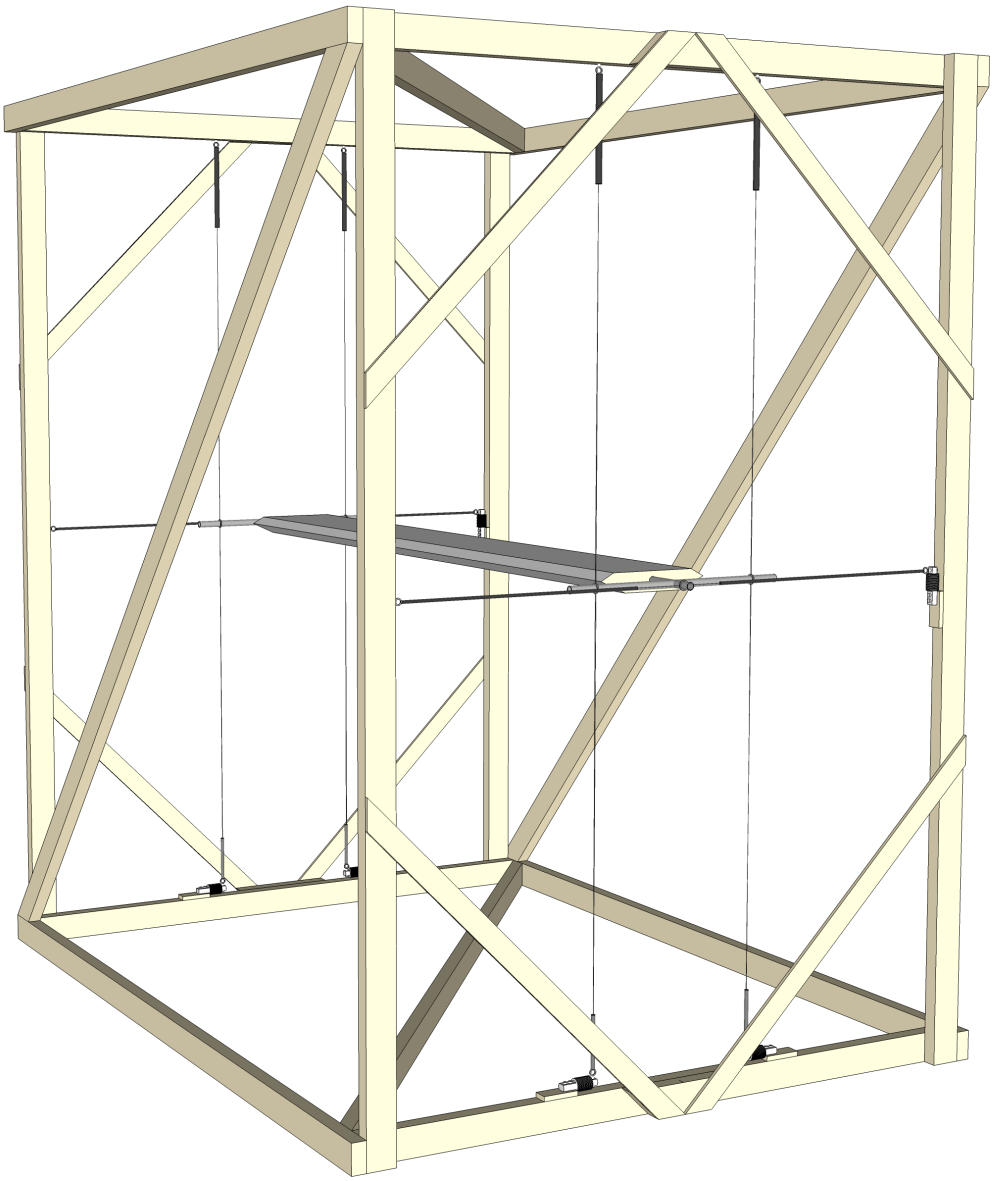

Figure 3.14: Sketch of the suspension rig.

(a) Front side *(b)* Back side

Figure 3.15: Wind tunnel at NTNU.

non-linear effects. It should be noted that the floor and the upper air feed tunnel make up definite boundaries for the height of the frame.

3.2.2.2 Springs

The choice of springs does not depend on stiffness alone. When the section model is oscillating, the springs must allow enough deflection, both in extension and contraction. Extension is limited by a maximum deflection recommendation from the spring manufacturer, while contraction is limited by the *pretension length* of the spring, i.e. it's extension when the section model is at rest. If a spring has no extension, it does not contribute to the stiffness of the system, and the estimated motion of the section model will be distorted. Hence, it is important that the maximum permitted extension of each spring is long enough to allow the necessary pretension length – which, according to the manufacturer, should not exceed 60 % of the permitted extension.

The springs should be as light as possible, particularly to ensure that the suspensions stays as straight as possible during motion, but also to reduce non-linear effects on the mass matrix. That is, if the vertical springs have high mass, they will contribute to the horizontal inertia, and opposite. Springs with large coil diameters also increase the damping of the system [37].

According to the spring manufacturer, Lesjöfors AB, the springs can be considered bi-linear, i.e. they must be loaded with an initial force before any deflection occurs, and this force is approximately constant regardless of deflection.

3.2.2.3 Geometric stiffness

A major part of the "horizontal stiffness", i.e. stiffness of the horizontal mode, stems from geometric stiffness due to tension in the vertical suspensions. This inherent stiffness may impose a severe constraint on the natural frequency of the horizontal mode. Hence, the initial force and pretension lengths of the vertical springs should be selected as low as possible.

3.2.3 Frame

The frame of the rig should be as high as possible to reduce non-linear effects when the section model is displaced laterally, but to allow future installation inn the wind tunnel, the height is restricted to approximately 3-3.5 m. Therefore, it is in the following assumed a height of 3 m. The width is less important with respect to non-linear effects, and is in the following assumed to be 2 m.

3.2.4 Section model

The size of the wind tunnel restricts the length of the section model to $L = 2.640$ m. To make the setup flexible, i.e. easy to reconfigure, it is in general desirable to make the section model itself as light as possible. That way, extra masses can easily be added to obtain the desired mass and moment of inertia.

A local tinsmith suggested to make the section model by using two 1.5 mm thick aluminium plates; one shaped to constitute the upper part of the profile, and the other one to constitute the lower part. The plates were supposed to be welded together. However, when the profile was to be manufactured, 1.5 mm plates were not available, so thicker 2 mm plates had to be used instead. This made the model considerably heavier (33 %) than the original design. Also, rivets had to be used to connect the upper and lower parts of the profile, as the plates warped during welding. This caused a small shape distortion, as it had to be made a little wider.

Figure 3.16 shows the section model, including the extension and rotation arms, modelled in Abaqus/CAE [1]. Figure 3.17 shows a drawing of the final profile, and exact positions of arms and wire brackets are shown in Figure 3.18. The extension arms are attached to the section model profile through pieces of wood attached at each end of it. The distance from vertical wire brackets to the torsional rotation axis was chosen to achieve the desired torsional frequency. The longitudinal axis of the extension arm is attached approximately at the shear centre, 35 mm above the bottom of the profile.

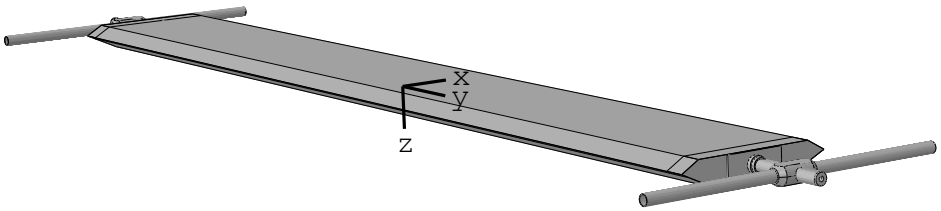

(a) Section model setup and axis definitions

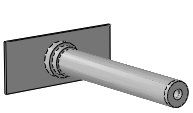

(b) Extension arm

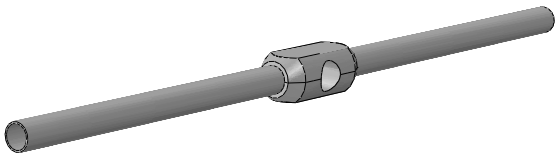

(c) Rotation arm

Figure 3.16: Section model setup modelled in Abaqus/CAE.

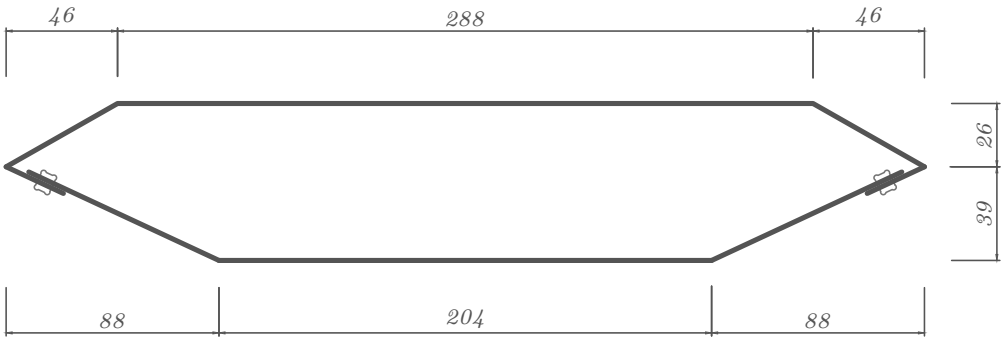

Figure 3.17: Section model profile. Dimensions are given in millimetres.

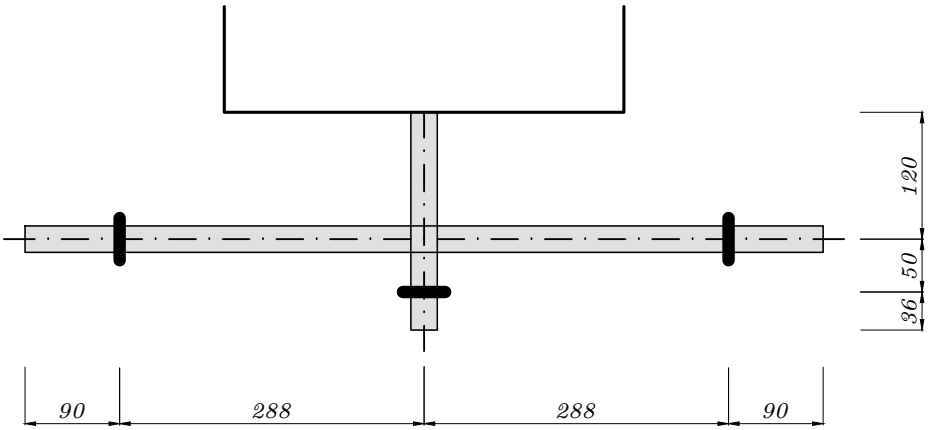

Figure 3.18: Details of the section model setup. Wire brackets are represented by thick black lines. Dimensions are given in millimetres.

3.2.5 Springs

After the section model itself, the main design decision is that of selecting springs. To maintain elastic symmetry of the model, all vertical springs (or spring series) should have approximately equal effective stiffness, and the same applies to horizontal springs.

It is desirable to achieve the target frequencies from Table 3.5, but geometric stiffness due to high tension in the vertical suspensions makes it difficult to maintain the ratio of the horizontal to vertical frequency. The geometric stiffness stems from two parts; pretensioning of vertical springs and weight of the section model. Thus, the problem can be overcome by raising the vertical frequency, however at the cost of a stiffer system and with lower maximum reduced velocity.

The wind tunnel report prepared for the Hardanger Bridge [50] indicates that the amplitude of the vertical mode can be approximately as large as the height of the bridge deck when flutter occurs, and torsional rotation can be up to 10°. Assuming that the vertical wires are attached 288 mm from the torsional rotation axis, the maximal deflection of the vertical springs becomes $65 + 288\sin(10°) = 115$ mm. Hence, the lower vertical springs should be pretensioned at least by this length. Since the upper vertical springs must balance tension in the lower suspensions in addition to the weight of the section model, they are automatically pretensioned enough to allow the required contraction. The important issue is rather to allow enough extension.

By relaxing the deflection length requirement for the lower vertical springs, it was enough with one small spring per suspension in place of two larger springs. Therefore, to save mass and money, this alternative was chosen.

The horizontal springs should have as low stiffness as possible, since geometric stiffness already contributes more than desirable. Low stiffness in general allow large deflections, so this is not an issue in the horizontal direction. However, the springs need still to have enough stiffness to provide a measurable change in force for a small change in deflection, since this is used to estimate horizontal movement of the model. The horizontal springs should be pretensioned as much as possible to avoid vertical deflections due to gravity.

To achieve the target frequencies, it was assumed correctly scaled mass and moment of inertia, and springs were chosen based on the simplified expressions given in (A.135) in Appendix A. However, due to manufacturing issues, the actual mass of the section model ended up higher than expected, which implied that the chosen spring stiffness was too low to achieve target frequencies.

Table 3.6 shows the properties, including chosen pretension lengths, of the three different spring configurations used on the prototype. It also gives the maximum permitted deflection of the springs after they have been mounted in the rig. It should be noted that the *recommended* permitted deflections are smaller than the desired values, but there was no problem with spring damage related to this during the laboratory tests.

	Spring 1	Spring 2	Series	
Cat.no. (Lesjöfors AB)	3363	3363	-	
Stiffness	20.0	20.0	10.0	N/m
Free length	0.160	0.160	0.320	m
Permitted extension	0.438	0.438	0.876	m
Initial force	1.8	1.8	1.8	N
Mass	0.019	0.019	0.038	kg
Pretension length			0.530	m
Permitted deflection after installation			0.346	m

(a) Horizontal spring series

	Spring 1	Spring 2	Series	
Cat.no. (Lesjöfors AB)	9602	9863	-	
Stiffness	440.0	410.0	212.2	N/m
Free length	0.100	0.100	0.200	m
Permitted extension	0.167	0.167	0.323	m
Initial force	10.5	10.5	10.5	N
Mass	0.046	0.045	0.091	kg
Pretension length			0.235	m
Permitted deflection after installation			0.088	m

(b) Upper vertical spring series

	Spring 1	Spring 2	Series	
Cat.no. (Lesjöfors AB)	9565	-	-	
Stiffness	210.0	-	210.0	N/m
Free length	0.090	-	0.090	m
Permitted extension	0.168	-	0.168	m
Initial force	6.5	-	6.5	N
Mass	0.020	-	0.020	kg
Pretension length			0.090	m
Permitted deflection after installation			0.078	m

(c) Lower vertical spring series

Table 3.6: Spring configurations used on the prototype. Specifications are given by manufacturer.

3.2.6 Mass and moment of inertia

The target mass and moment of inertia of the section model is given in Table 3.7.

	Per unit length (kg/m)	Total (kg)
Target mass	$m_{ms} = 5.240$	$M_{ms} = L \cdot m_{ms} = 13.834$
Target moment of inertia	$m_{I,ms} = 0.0694$	$I_{yy,ms} = L \cdot m_{I,ms} = 0.1833$

Table 3.7: Target mass and moment of inertia. $L = 2.640$ m.

If the mass and/or moment of inertia of the section is lower than the target mass, this can be accurately corrected by mounting weights to the rotation arm. However, since the actual mass of the section model ended up higher than the target mass, no additional weights were needed in the present setup.

The effective mass of springs is assumed to be the theoretical one third of the actual mass. It is also assumed that a spring only contributes to the inertia of the system along it's longitudinal axis. Moment of inertia of the section model, extension arm and rotation arm was determined by accurate modelling in Abaqus/CAE, and verified by hand calculations and experiments in the laboratory.

Mass and moment of inertia about all axes are given in Table 3.8.

3.2.7 Mathematical models

To enhance the design process, two mathematical models have been developed: a FE-model modelled in Abaqus/CAE [1] and a tailor-made, analytical model.

3.2.7.1 FE-model

To verify the dynamic properties of the section model, the whole rig was modelled as a finite element model in Abaqus/CAE.

The section model, extension arms and rotation arms are modelled as beams are constituting a rigid body, giving a minimum number of DOFs and thereby allowing effective simulations. Spring stiffness is modelled by linear spring elements and constant (initial) spring forces are introduced to the section model through *slip ring connectors*, which ensures that a force always follows the spring orientation. Mass and moment of inertia are based on Table 3.8, and are specified as point inertias. Effective spring masses are applied through the same connectors as the constant spring forces, ensuring that they only contribute to inertia along their longitudinal axis.

Quantity	Mass (kg)	Moment of inertia (kg·m^2)		
		I_{xx}	I_{yy}	I_{zz}
Section model	12.234	7.990	0.164	8.140
Extension arm	0.477	0.002	0.000	0.002
Rotation arm	0.508	0.000	0.010	0.010
Wire bracket, horizontal wire	0.020	-	-	-
Wire bracket, vertical wire	0.017	-	-	-
Horizontal spring	0.038	-	-	-
Upper vertical spring	0.091	-	-	-
Lower vertical spring	0.020	-	-	-

(a) Mass and and moment of inertia about local centre of gravity of all parts involved in the setup.

Quantity	Mass (kg)	Moment of inertia (kg·m^2)		
		I_{xx}	I_{yy}	I_{zz}
Section model	12.234	7.990	0.164	8.140
Extension arms	0.954	1.982	0.000	1.982
Rotation arms	1.016	2.107	0.019	2.126
Wire brackets, horizontal wire	0.040	0.089	-	0.089
Wire brackets, vertical wire	0.068	0.141	0.006	0.141
Horizontal springs	0.025*	-	-	0.056
Upper vertical springs	0.121*	0.252	0.010	-
Lower vertical springs	0.027*	0.055	0.002	-
Mass of section model setup	14.312			
Effective horizontal mass	14.337			
Effective vertical mass	14.460			
Effective moment of inertia		12.616	0.201	12.534
Target values	13.834	-	0.183	-

(b) Total mass and and moment of inertia of the section model setup. Spring masses are marked with * to indicate effective mass, i.e. a third of the actual mass.

Table 3.8: Mass and moment of inertia of the section model setup. Axis definitions are given in Figure 3.16. The large deviations from the target values are due to manufacturing issues with the section model.

The Abaqus/CAE model file is designed to enhance modifications for future work. To learn about the details of the model and how it can be modified, see Appendix C.

The rigid body modes of the system are illustrated in Figure 3.19. It is seen that there are three uninteresting modes inherent in the model, "longitudinal translation", "horizontal rotation" and "vertical rotation". Simulations of response to a turbulent wind field accompanied with video of wind tunnel tests of the Hardanger Bridge, indicates that the rotational modes will be present during tests, but the longitudinal translation mode is not likely to get excited. If it is, it should be possible to constrain it with strings. Thus, from now on, the mode concerning longitudinal translation will not be considered.

3.2.7.2 Analytical model

To be able to immediately evaluate the effect of a change of one or more design parameters, it was necessary to develop an analytical model. Essentially, the model is all about computing the mass and stiffness matrix of the system, including non-linear effects of displacements, which then yields undamped natural frequencies and modes. The mass matrix of this model is straightforward from Table 3.8b, but the stiffness matrix is very complex. The derivation of the stiffness matrix is given in Appendix A. Calculations are performed in MATLAB.

3.2.8 Natural frequencies

The natural frequencies of the model (at rest) serve as a measure of the scaling of stiffness. It is seen from Table 3.9 that the values produced by the prototype design deviates significantly from the target frequencies. However, it should be noted that the torsional frequency has been adjusted to maintain the important frequency ratio related to flutter.

3.2.8.1 Sensitivity to design parameters

The effect of changes in several design parameters are illustrated in Figure 3.20. It is clear that the ratio between vertical and horizontal frequencies can be increased by adjusting several of these parameters, but only increase of vertical stiffness would be feasible in practice. It is also possible to decrease the horizontal frequency by removing the horizontal springs, although that would require lasers or position transducers to obtain measurements of horizontal displacements. This alternative has not been considered in the present work, as the necessary equipment was not was available.

Figure 3.21 shows that an increase of vertical spring stiffness to approximately 300 N/m would give correct frequency ratios. However, at the time springs had to be ordered, it was focused on obtaining natural frequencies as close to the target frequencies as

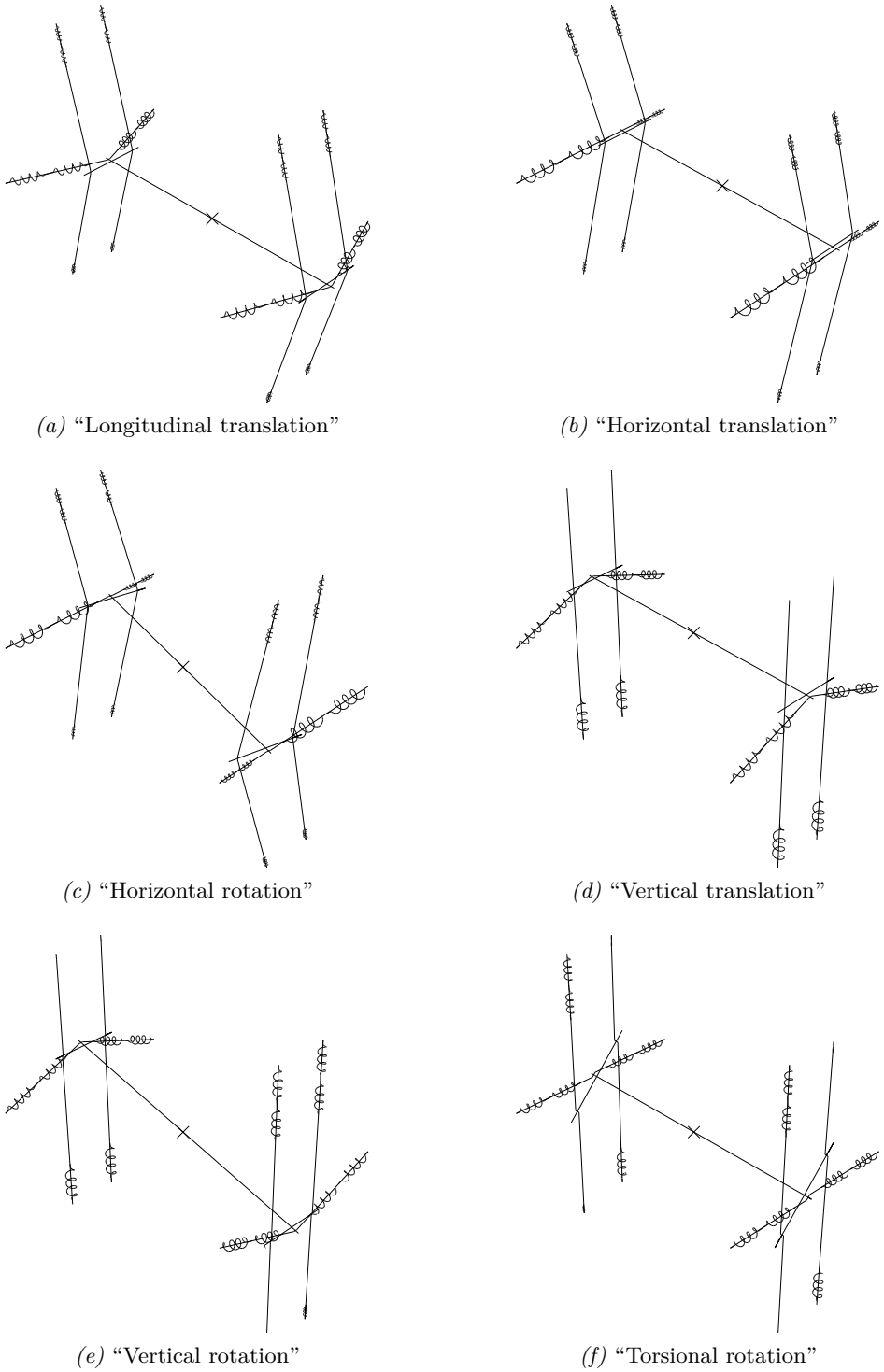

(a) "Longitudinal translation"

(b) "Horizontal translation"

(c) "Horizontal rotation"

(d) "Vertical translation"

(e) "Vertical rotation"

(f) "Torsional rotation"

Figure 3.19: Rigid body modes of the section model.

Mode	Target (Hz)	Abaqus/CAE (Hz)	Analytical (Hz)
Longitudinal translation	-	0.6566	-
Horizontal translation	0.6325	0.6710	0.6724
Horizontal rotation	-	1.0548	1.0529
Vertical translation	1.7700	1.7017	1.7017
Vertical rotation	-	2.6272	2.6235
Torsional rotation	4.3800	4.2151	4.2112

(a) Natural frequencies

Modes	Target	Design	Deviation
Torsional rotation to vertical translation	2.48	2.48	0 %
Torsional rotation to horizontal translation	6.94	6.28	-9.5 %
Vertical translation to horizontal translation	2.80	2.53	-9.6 %

(b) Frequency ratios

Table 3.9: Natural frequencies of the section model.

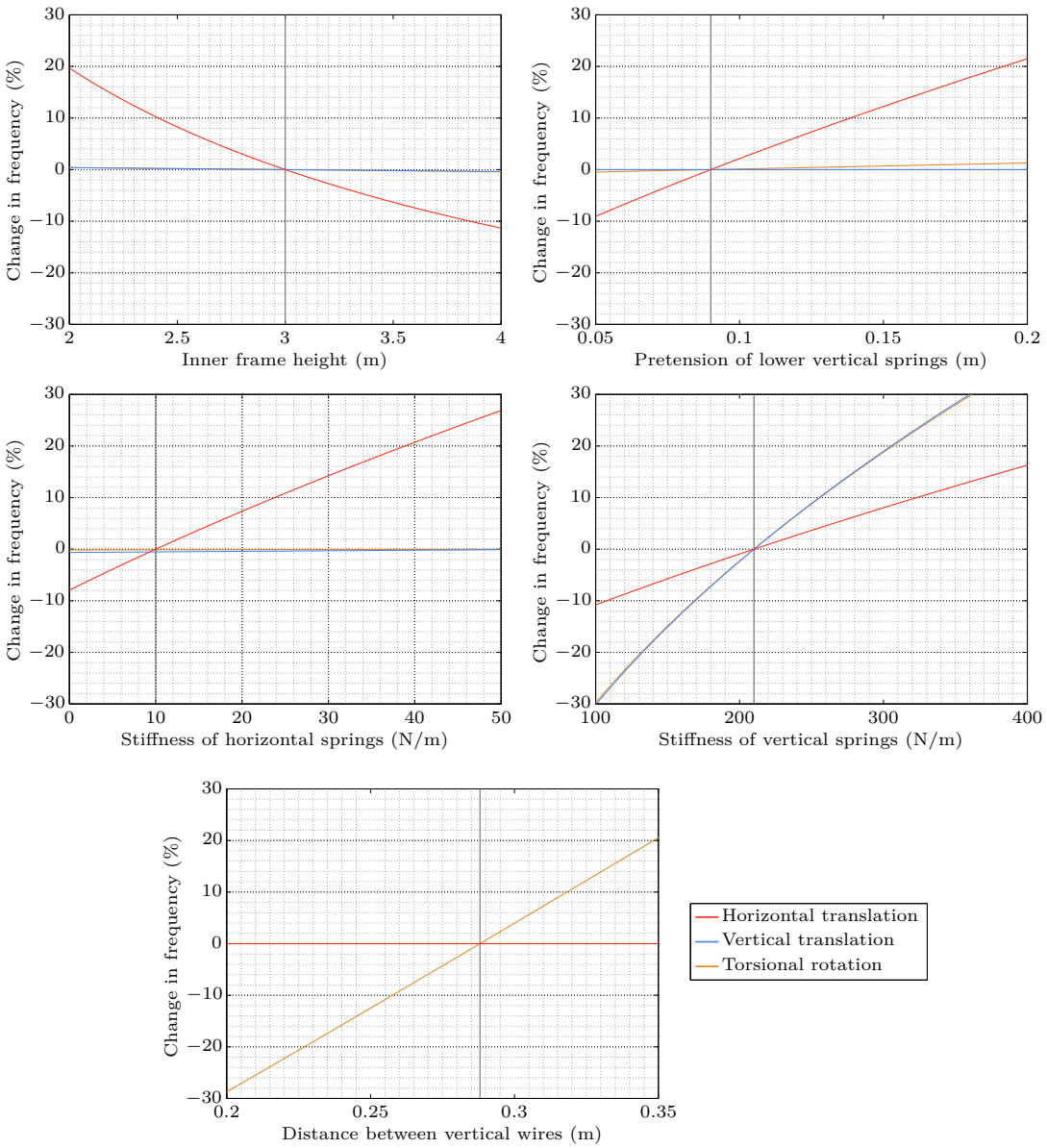

Figure 3.20: Change in natural frequencies as function of important design parameters. The torsional rotation curve is approximately equal to that of vertical translation in all but the last figure.

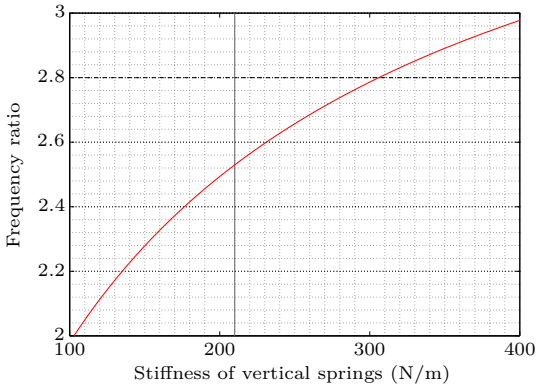

Figure 3.21: Ratio of vertical to horizontal translational frequencies. The selected stiffness is indicated by a vertical line, and the target ratio is indicated by a dashed horizontal line.

possible. Therefore, it was decided to go for lower stiffness – even though, in retrospect, it still should have been higher, since the mass turned out to be larger than expected.

The effect of the pretension length of vertical springs also shows that a major part of the horizontal stiffness stems from geometric stiffness due to tensile force in the vertical wires. In fact, approximately 85 % of the horizontal stiffness is due to tensile force in vertical suspensions.

The torsional frequency is linear with respect to the distance between vertical wires.

3.2.9 Static displacements

The average wind velocity pressure acting on the section model during wind tunnel tests give rise to static displacements. Figure 3.22 gives horizontal (translational) displacement due to a horizontal force acting on the section model at it's centre of gravity, and it is evident that the stiffness is non-linear.

Assuming that the load coefficients given in Table 3.3 are valid for the prototype setup, simulation of a 20 m/s turbulent wind field in Abaqus/CAE (see Appendix B) gives a horizontal static displacement of 154 mm and a vertical static displacement of 43 mm (downwards). The displacement downwards was unexpectedly large, but it should be noted that the lift slope coefficient $\mathrm{d}C_L/\mathrm{d}\alpha$ is highly conservative. However, if it actually turns out to be this large in wind tunnel experiments, the effective pretension length of the lower vertical springs will be significantly reduced – which in turn reduces the maximum vertical and torsional amplitudes that can be represented. The horizontal and vertical buffeting excitation amplitude was 42 and 11 mm, respectively.

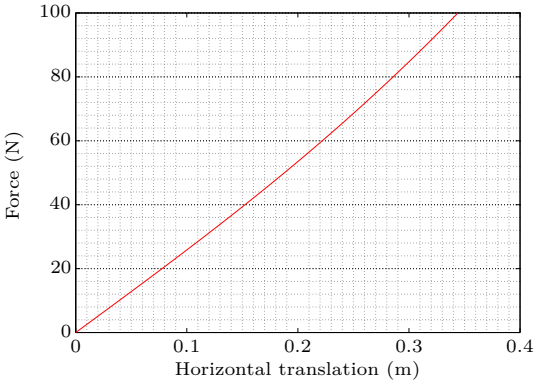

Figure 3.22: Force vs. horizontal translation of the section model.

3.3 Experimental setup

3.3.1 Frame

The frame was constructed by 48×98 mm spruce timber according to Figure 3.14, and the final structure was stiff and heavy enough to allow large excitation of the section model without vibrating. Final construction drawings of the frame is shown in Figure 3.23, and a picture of the final prototype is shown in Figure 3.24.

Because of a last minute change of the load cell mounting setup, the total length of the suspension pairs ended up 50 mm longer than the designed length. That is, the effective inner frame height was 3050 mm rather than 3000 mm, and the effective width was 2050 mm instead of 2000 mm. This has of course been considered in computations in subsequent chapters.

3.3.2 Section model

The section model profile was manufactured in aluminium by Blikkenslager Olaf Hansen AS in Trondheim.

To allow the extension arms to be attached to the profile, 48 mm thick wooden pieces was glued to the profile at each end, before the extension arms was screwed onto them. Extension and rotation arms was manufactured by a former professor at NTNU. To allow easy positioning of the wires, they was attached to the arms by custom-made brackets.

The final setup is shown in Figure 3.24.

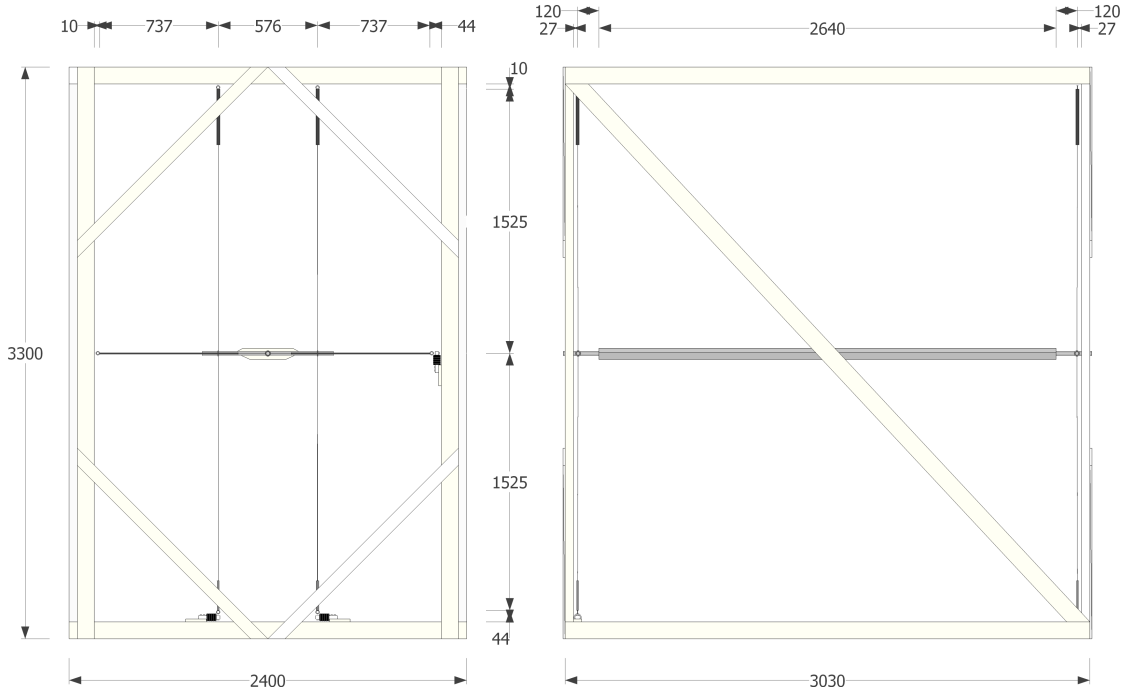

(a) Front view *(b)* Side view

Figure 3.23: Final construction drawings of the suspension rig.

3.3.3 Load cells

To completely determine the motion of the model, it is enough to measure the force in one out of the two springs in each suspension pair. Hence, six HBM Z6FC2 load cells were installed. C2 is a quality measure according to OIML R 60 regulations, and means that the maximal number of load cell verification intervals is 2000.

Two of the load cells have a maximum capacity of 10 kg, two of 20 kg and two of 50 kg. A lower maximum weight implies higher accuracy, since the number of verification intervals is the same. Since the horizontal springs have a very low stiffness, the two with 10 kg maximum capacity were installed to measure horizontal forces. The remaining 20 and 50 kg cells were installed to measure forces in the vertical springs; the two with 20 kg capacity on one end of the section model, and the two with 50 kg capacity on the other.

Calibration was performed by comparison to known weights, and the accuracy proved to be high. The load cells with 10 and 20 kg maximum capacity were correct to a fraction of a gram, while the 50 kg cells was correct to ± 2 g.

The data acquisition was performed by a HBM Spider 8 unit, which amplify, filter and digitalise signals from the load cells. The filter is a 10 Hz Butterworth-filter, and data was sampled at 200 Hz to ensure a fairly white frequency distribution of any noise.

3.3.4 Springs

The spring stiffness and corresponding initial forces were measured to verify the specifications provided by the supplier. The measurements were obtained by measuring the spring force at various deflections. It was found that the stiffness and initial forces of the horizontal springs matched specifications well, while the stiffness of the vertical springs on average was a approximately 1-2 % lower than specified, approximately 207-209 N/m. It was also noted that the stiffness was not perfectly linear, but stiffer for medium deflections than for long and short deflections.

Small deviations of stiffness and initial forces only matters when displacements are to be estimated based on the forces. To ensure maximal accuracy of the estimation, the measured stiffness and initial forces were calibrated such that the estimated deflection (due to pretensioning) of each spring was correct *after* installed in the rig.

3.3.5 Wire

To connect the section model to the springs, high tension spring wire with a diameter of 0.4 mm (Lesjöfors cat.no. 6415) was used. Attachment loops were made simply by bending the wire and wrapping duct tape around it to keep it in place. To ensure the integrity of the loop, the wire was bended and wrapped several times.

(a) Rig prototype

(b) Load cells

(c) Suspension setup

Figure 3.24: Pictures of the experimental setup.

4 Results and discussion

An important part of this work is to determine the dynamic properties of the experimental setup. To ensure reliable results, experiments must be carried out systematically and the system identification quality has to be verified. Finally, non-linear effects of static displacements and excitation amplitudes should be investigated.

4.1 Identification experiments

The prototype setup only allows experiments involving free vibration response in still air. To investigate effects of static displacements and excitation amplitudes, simulations had to be conducted in Abaqus/CAE.

Ideally, a mechanical setup, possibly based on magnetism, would have been installed to produce the initial displacements. Such equipment was not available, but it was found satisfactory to introduce displacements by hand, i.e. by forcing the section model into a specific configuration before releasing it. By introducing displacements by hand, they will necessarily not be exactly the same for each test. Since the identification itself (in theory) is independent of signal amplitudes, this should not pose a problem, but to enhance the reliability of the results, all experiments were repeated at least three times.

4.1.1 Structural properties

To ensure good identification of the structural properties of the prototype, the tests described below were conducted. *Small displacements* means as small as possible while still obtaining good data – due to damping, the torsional mode requires a relatively larger displacement than the horizontal modes.

Test 1 *All modes excited by small initial displacements.*
This test produces free vibration response in still air with minimum non-linear amplitude effects, and serves as a baseline for the other tests.

Test 2 *All modes excited by small initial displacements, torsional inertia modified.*
This test was also intended to confirm that the analytical model gives correct

results if essential design parameters change.

Test 3 *All modes excited by small initial displacements, torsional stiffness modified.*
This test was intended to confirm that the analytical model gives correct results if essential design parameters change.

4.1.2 Effect of excitation amplitudes

The amplitude dependency may be important, particularly considering the non-linear horizontal stiffness. Analytical results indicate that horizontal displacement is the dominating source of stiffness changes in the system.

To investigate this in the suspension rig, each mode was successively excited with a large amplitude, and the displacements were record until dampened out. By performing system identification on successive portions of the recorded signal (where the amplitude decreases for each portion), the amplitude dependency was determined.

More specifically, the following tests were carried out:

Test 4a *Horizontal translational mode excited by maximum initial displacement.*
This test was intended to investigate how stiffness and damping of the horizontal translational mode changes with it's amplitude.

Test 4b *Horizontal translational mode excited by maximum initial displacement, all other modes excited by small initial displacements.*
This test was intended to investigate how stiffness and damping of all modes changes with horizontal amplitude.

Test 4c *Horizontal translational mode excited by medium initial displacement, all other modes excited by small initial displacements.*
This test was intended to further investigate how stiffness and damping of all modes changes with horizontal amplitude.

Test 5 *Horizontal rotational mode excited by maximum initial displacement.*
This test was intended to investigate how stiffness and damping of the horizontal rotational mode changes with it's amplitude.

Test 6 *Vertical translational mode excited by maximum initial displacement.*
This test was intended to investigate how stiffness and damping of the vertical translational mode changes with it's amplitude.

Test 7 *Vertical rotational mode excited by maximum initial displacement.*
This test was intended to investigate how stiffness and damping of the vertical rotational mode changes with it's amplitude.

Test 8 *Torsional rotational mode excited by maximum initial displacement.*
This test was intended to investigate how stiffness and damping of the torsional rotational mode changes with it's amplitude.

4.1.3 Abaqus/CAE simulations

All tests performed on the prototype was also simulated in Abaqus/CAE. For infinitely small amplitudes, natural frequencies was obtained directly by solving the eigenvalues of the system, rather than performing system identification on simulated response.

In addition to the free vibration tests, it is desirable to investigate the behaviour of the section model when exposed to turbulent wind. This was simulated by a Monte Carlo simulation of the buffeting loads acting on the section model, followed by a response simulation in Abaqus/CAE. It should be noted that frequency dependent motion induced forces were not included in the simulation.

4.2 Response measurements

System identification is based on displacement records of the section model. The section model has six rigid body modes, but the sixth mode, longitudinal translation, was barely excited during the free vibration tests, and it was not observable in the recorded time series. Hence, it is assumed to have five independent (modal) degrees of freedom; two translational and three rotational.

Modes with very small excitation amplitudes can cause badly conditioned matrices and numerical issues with the identification methods, even after normalisation of the signals. This is overcome by performing identification on signals where each channel contains the response of a single modal degree of freedom. Since each channel contains information about one mode only, it does not affect the observability of the (reduced) system. Hence, uninteresting or less excited modes can be omitted by discarding them from the output signal.

There are several ways to measure the response of the section model, e.g. by laser, position transducers or spring forces. Measuring by laser could be challenging, since the suspension rig allow motion in five (six) degrees of freedom, and it would be hard to ensure that the lasers kept track of the correct spatial points on the section model setup. Position transducers were not available at NTNU, and it was also suspected that they would have introduced damping and disturbed the force symmetry of the model (the extension cables are subjected to a constant, non-negligible tension force). Hence, it was decided to record displacement indirectly through spring forces, measured by load cells.

4.2.1 Computation of displacements

The displacement of a wire bracket from position P_0 to P, illustrated in Figure 4.25, can be computed from measured spring forces by the four step process described below. It is assumed perfectly bilinear springs, infinitely stiff wires and that the measurement of a spring force is independent of the spring direction (angle). Finally, rotation estimates

are based on an assumption of small angles, which may be an incorrect simplification, particularly when it comes to torsional rotation (which may be up to 10°).

The four steps are:

1. Estimate the horizontal displacement p of the wire bracket directly from change of tension in horizontal springs attached at the corresponding side of the section model.

2. Remove the constant (initial) spring force from F and estimate the spring length l by Hooke's law. To improve accuracy, the spring stiffness should be combined with the stiffness of the elastic wire into an effective stiffness of the suspension.

3. Estimate the vertical displacement h of the wire bracket by

$$h = \sqrt{(l + w)^2 + p^2} - (l_0 + w) \tag{4.82}$$

   where p is the horizontal displacement determined above and l_0 is the initial spring length. The initial length of a spring is it's free length plus the pretension length when the section model is at rest.

4. Transform the displacements of the six wire brackets into the five modal degrees of freedom.

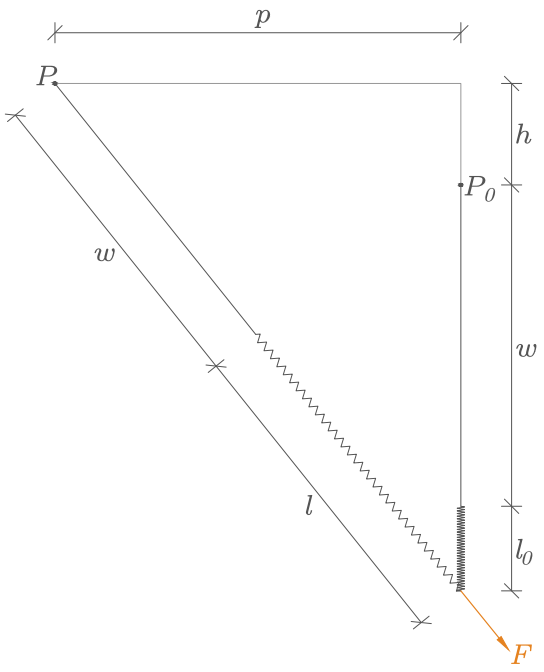

Figure 4.25: Displacement of a wire bracket from P_0 to P.

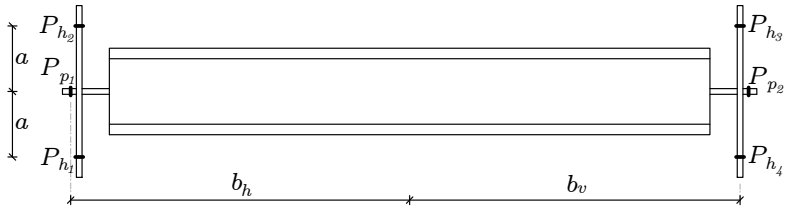

Figure 4.26: Wire bracket positions.

Figure 4.26 identifies the six wire bracket positions and distances to corresponding rotation axes, where

$$a = 0.288 \text{ m}, \qquad b_v = 1.440 \text{ m}, \qquad b_h = 1.490 \text{ m}$$

The modal displacements can now be found by

$$\begin{bmatrix} r_1 \\ r_2 \\ r_3 \\ r_4 \\ r_5 \end{bmatrix} = \frac{1}{4} \begin{bmatrix} 2 & 2 & 0 & 0 & 0 & 0 \\ -2/b_h & 2/b_h & 0 & 0 & 0 & 0 \\ 0 & 0 & 1 & 1 & 1 & 1 \\ 0 & 0 & 1/b_v & 1/b_v & -1/b_v & -1/b_v \\ 0 & 0 & 1/a & -1/a & -1/a & 1/a \end{bmatrix} \begin{bmatrix} p_1 \\ p_2 \\ h_1 \\ h_2 \\ h_3 \\ h_4 \end{bmatrix} \tag{4.83}$$

where $r_{1\text{-}5}$ are the modal degrees of freedom; horizontal translation, horizontal rotation, vertical translation, vertical rotation and torsional rotation, respectively.

Figure 4.27 shows the fluctuating components of the forces measured during a free vibration test. It is evident that the frequency content of the forces is concentrated at the five natural frequencies of the system, although the PSD of horizontal rotation is much smaller than the PSD of horizontal translation. This implies that the system is observable, which is an important requirement for system identification.

Figure 4.28 shows the computed displacement response, which agrees well with the observed amplitudes (judged by eye) during the tests. It is clear that each channel contains a single harmonic component, which is the free vibration response to the initial excitation of that particular mode.

4.2.2 Preprocessing of data

In addition to the Butterworth filter applied to the force signals by the data acquisition device, several processing steps are applied to enhance the system identification:

1. Detrend response signals to ensure zero mean, i.e. remove the static (mean) component to isolate the fluctuating component. The static displacements are, however, necessary for correction after the system identification.

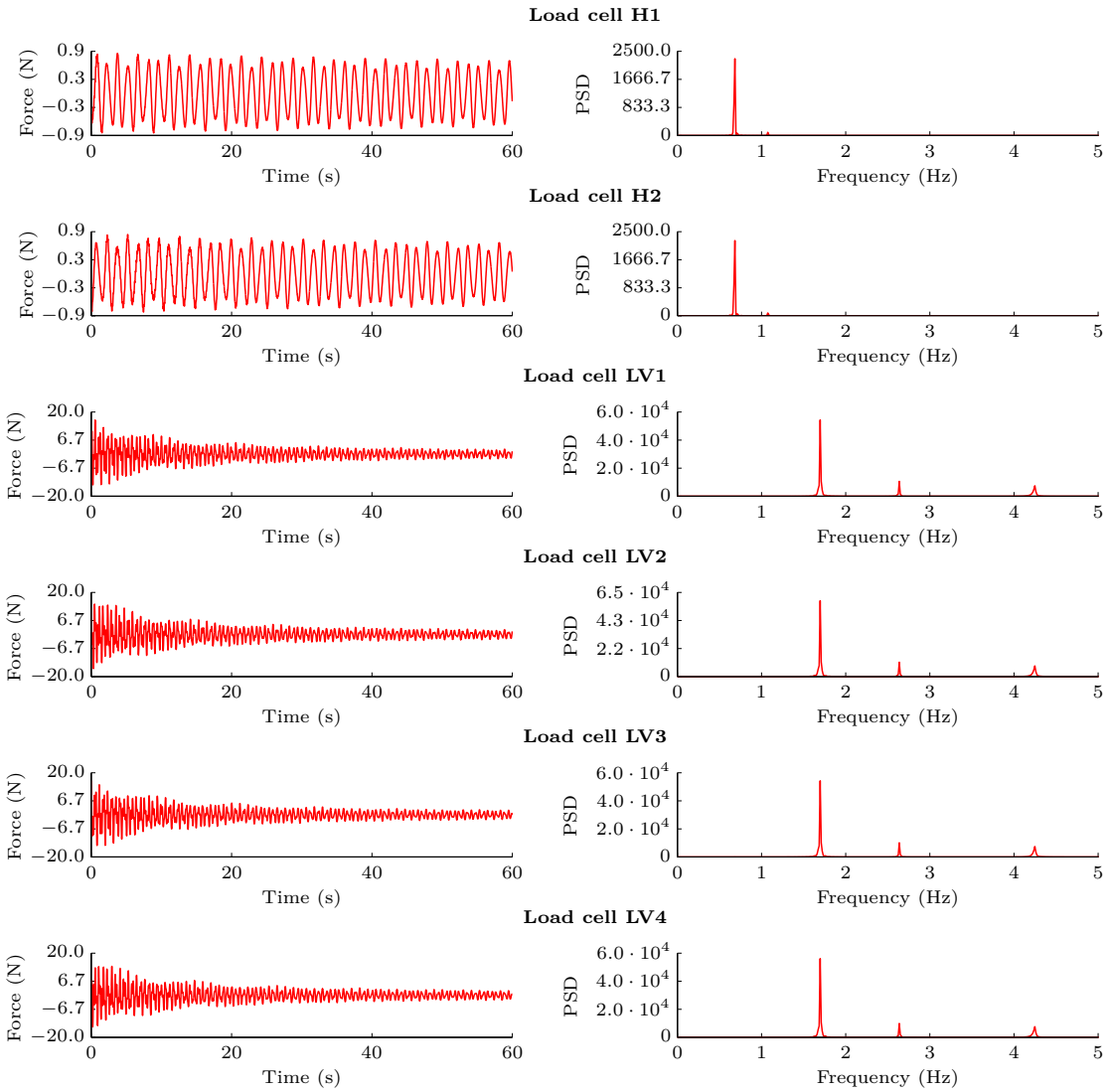

Figure 4.27: Fluctuating component of forces due to free vibration response. "H" and "LV" refer to load cells connected to horizontal and lower vertical springs, respectively.

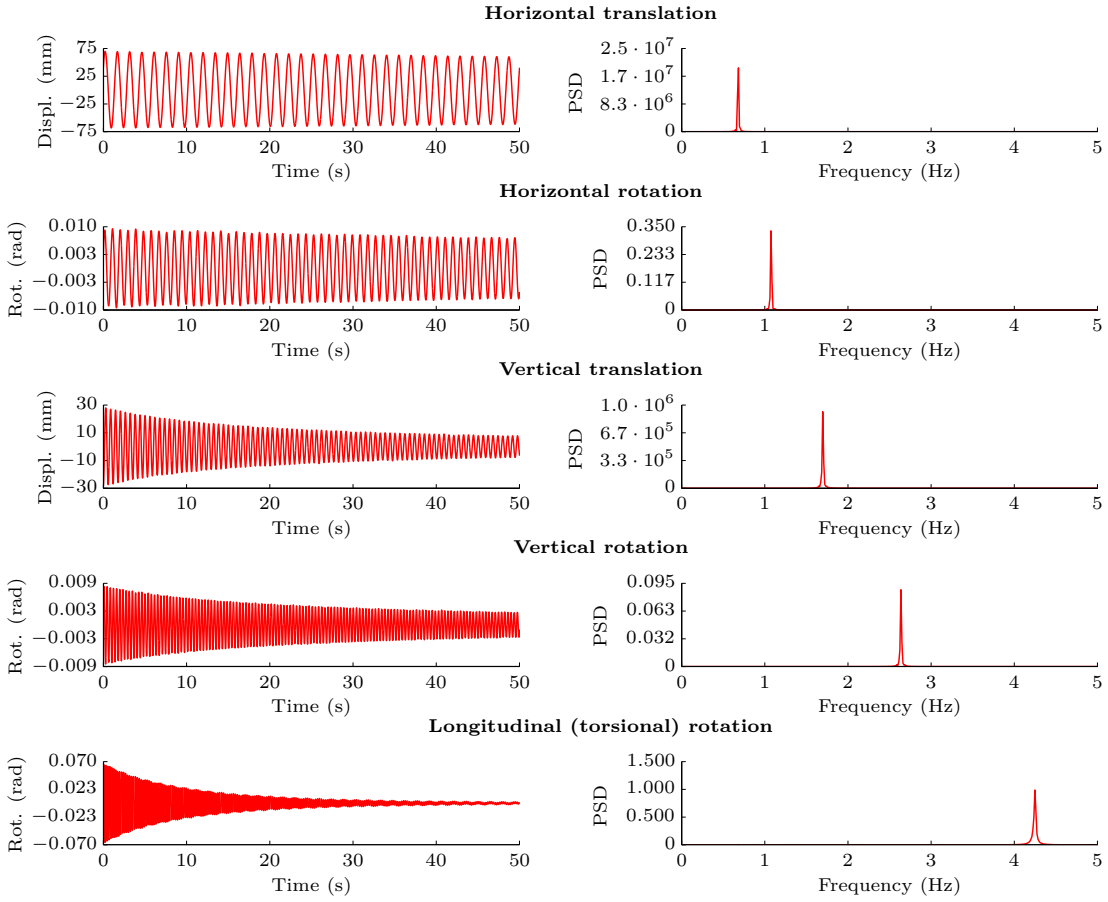

Figure 4.28: Free vibration response and corresponding power spectra.

2. Apply a zero-phase (bidirectional), low-pass Chebyshev Type I filter to remove high frequency noise and spring resonance vibrations. The filter used herein has an effective order of 16, i.e. 8 on each pass. To avoid significant amplitude distortion, the cutoff-frequency should be 20-30 % higher than the natural frequency of the torsional mode.

3. Resample (decimate) the signal to a suitable sampling rate. The choice of sampling rate is discussed in detail in section 4.3.2.

4. Apply a "windowing" method to circumvent the misfit at the two extreme ends of the time series, i.e. discard samples at the beginning and end of the signal that may be inaccurate due to filtering and/or resampling. It was found that truncating 10 % of the beginning and end of the signal produced good and consistent results.

5. Normalise the response signals to unit standard deviation, to avoid numerical issues with badly conditioned matrices.

It should be noted that a correct amplitude is more or less irrelevant, as long as frequency, phase (relative to other modes) and logarithmic decrement are maintained.

4.3 System identification

The system identification methods will be tested on both measured and simulated data to learn their ability to produce consistent and reliable results. It is also important to find out how the identification is affected by sampling rate, signal duration etc.

In the following, the terms *estimated* and *identified* refer to quantities, e.g. stiffness matrix or modal damping ratios, obtained by system identification, while the term *analytical* refers to quantities obtained by the analytical stiffness matrix derived in appendix A.

4.3.1 Preliminary analysis

The power spectra in Figure 4.28 clearly indicates the natural frequencies of the system, which are compared to analytical values in Table 4.10.

An estimate of the modal damping ratios is found by investigating the logarithmic decrements of the displacement records in Figure 4.28. The values in Table 4.11 have been estimated by measuring 7 equidistant peaks for each modal response, where the distance is chosen to span as much of the record as possible. They correspond well to the measured displacements, as illustrated in Figure 4.29.

Mode	Analytical (Hz)	Estimated (Hz)
Horizontal translation	0.68	0.68
Horizontal rotation	1.06	1.07
Vertical translation	1.70	1.70
Vertical rotation	2.62	2.64
Torsional rotation	4.23	4.25

Table 4.10: Natural frequencies obtained analytically and estimated by spectral analysis.

Mode	Peak interval	Damping ratio (%)
Horizontal translation	5	0.06
Horizontal rotation	7	0.09
Vertical translation	12	0.19
Vertical rotation	19	0.12
Torsional rotation	31	0.25

Table 4.11: Modal damping ratios estimated by logarithmic decrements.

4.3.2 Identification parameters

To ensure good identification of the system, it is essential to adjust the parameters of the respective methods adequately; they must produce good results both from measured an simulated data. The most important parameters are model order, sampling rate and maximum number of lags for covariance estimates in the CBHM method. The parameters will be optimised based on measured data, and then verified on simulated data.

4.3.2.1 Model order

Valuable information about the state-space order of the dynamic system can be obtained by inspection of the singular values obtained by SVD in the CBHM (and N4SID) method, which is shown in Figure 4.30. The identification is performed on data resampled to 10 Hz. It is clear that the state space model should be of order 10, which is reasonable, since only five of the six rigid body modes of the section model are observable in the output. The effect of altering the model order is shown in Figure 4.31, and it is seen that an order of ten estimates the frequencies exactly. Higher orders introduce spurious frequencies, while lower orders are missing frequencies. It should, however, be noted that the spurious frequencies corresponds to singular values that would have been truncated by the transformation to the final state space model; see section 2.3.4 and the note on equation (2.74).

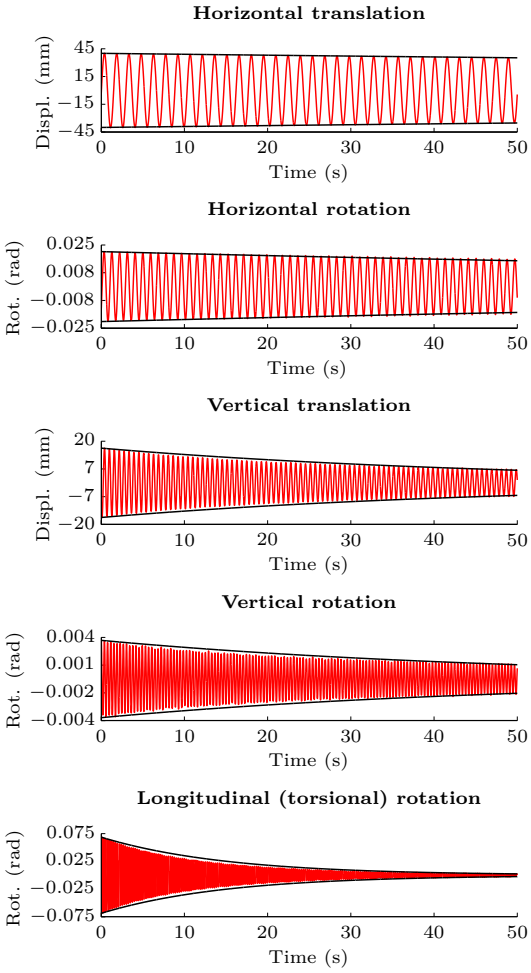

Figure 4.29: Verification of modal damping ratios estimated by logarithmic decrements. Amplitude limits due to estimated damping are indicated by black curves.

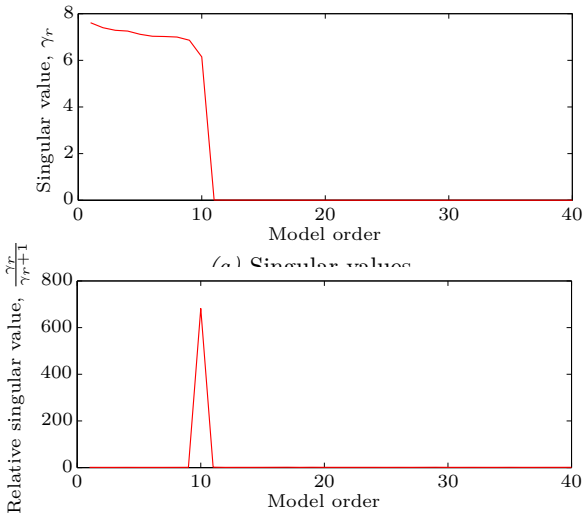

(b) Relative singular values

Figure 4.30: Singular values obtained by the CBHM method.

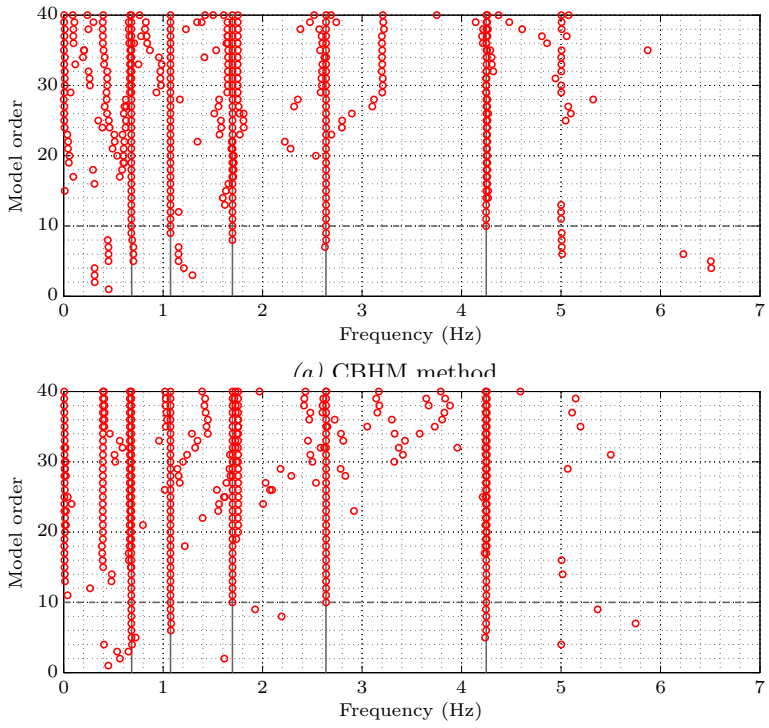

(b) N4SID method

Figure 4.31: Estimated natural frequencies vs. model order. Frequencies estimated by spectral analysis are indicated by vertical lines.

4.3.2.2 Sampling rate

All time series are sampled over 60 seconds at 200 Hz, but resampling to an optimal sampling rate is important to obtain good identifications.

Figure 4.32 and Figure 4.33 shows the effect of sampling rate on the modal quantities and structural matrices, respectively, identified by the CBHM method. It is here assumed a maximum time lag for covariance estimates corresponding to one period of horizontal translation, which is the longest natural period. Based on the diagrams, it is evident that the effect on the CBHM identification is negligible, although a minor reduction of some of the (false) cross terms in the damping matrix occurs when the sampling frequency increases. However, the identified modal damping ratios do not coincide well with the preliminary estimates.

Major cross terms in the damping matrix are more or less present in all identifications by the CBHM method. In this case, however, the effect on identification of aerodynamic derivatives should be small, as they are mainly associated with vertical rotation.

On the contrary, the effect on the N4SID identification is highly present in Figure 4.34. The damping matrix, particularly the terms that corresponds to horizontal motion, proves to be sensitive to the sampling rate. The reason for this is that horizontal motion occur at low frequencies that are determined by a large number of samples per oscillation cycle, giving rise to inaccuracies in the conversion from discrete to continuous eigenvalues, which is sensitive to number of samples per cycle. The effect is the same, if not worse, for the displacement records from the other tests performed in the laboratory. One of them peaked to approximately 100 % damping ratio if resampled to 120 Hz, but if resampled to 110 or 130 Hz, the results were relatively good. The only sampling rates that gave consistent, good results was 10–30 Hz. Hence, subsequent identifications will be based on data decimated to 10 Hz, which corresponds to approximately two samples per period of torsional rotation.

The N4SID identification seems to provide good estimates of both stiffness and damping matrix, as the damping ratios coincides with those of the preliminary analysis, and both matrices are approximately diagonal. A sampling rate of 10 Hz gives the smallest cross terms in the damping matrix. As was the case for the damping matrix identified by the CBHM method, the significant cross terms are associated with vertical rotation, which is not included in the computation of aerodynamic derivatives.

The identifications performed in subsequent sections are based on data resampled to 10 Hz.

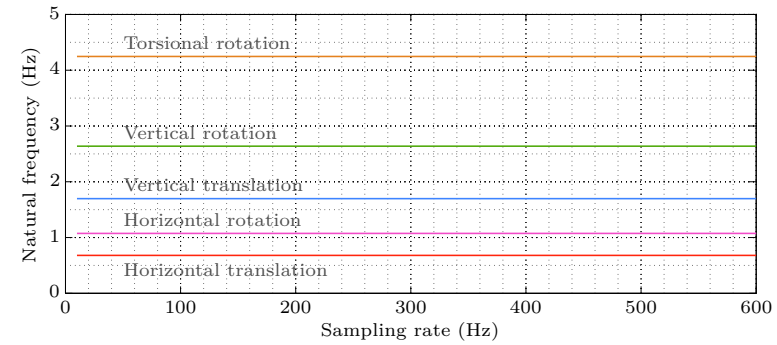

(a) Natural frequencies

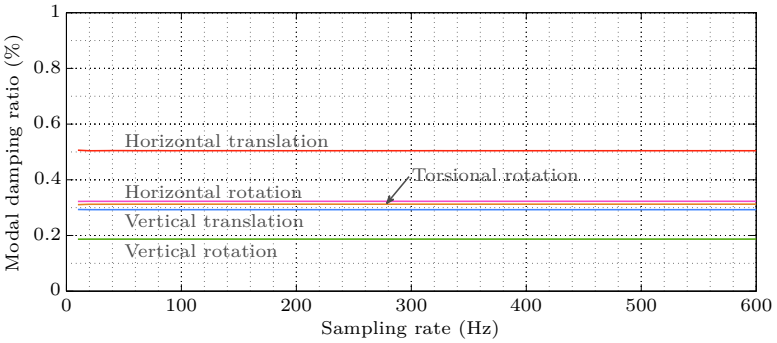

(b) Modal damping ratios

Figure 4.32: Effect of sampling rate on CBHM identification.

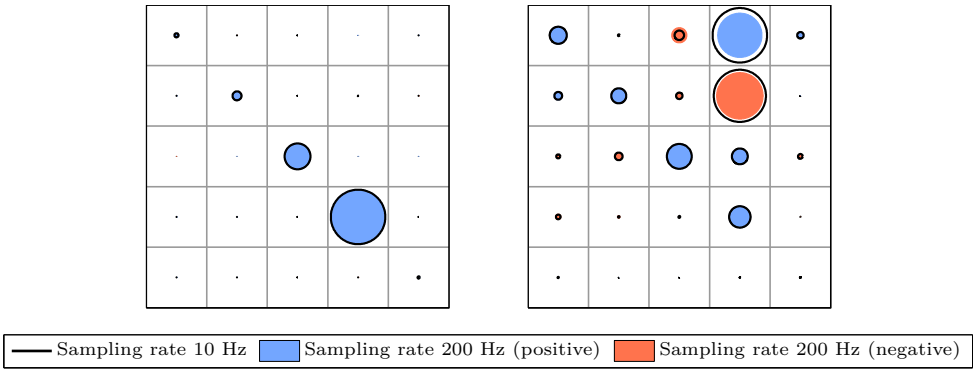

(a) Stiffness matrix *(b)* Damping matrix

Figure 4.33: Relative changes of structural matrices identified by the CBHM method when sampling rate is changed from 200 Hz to 10 Hz. Radius is proportional to value.

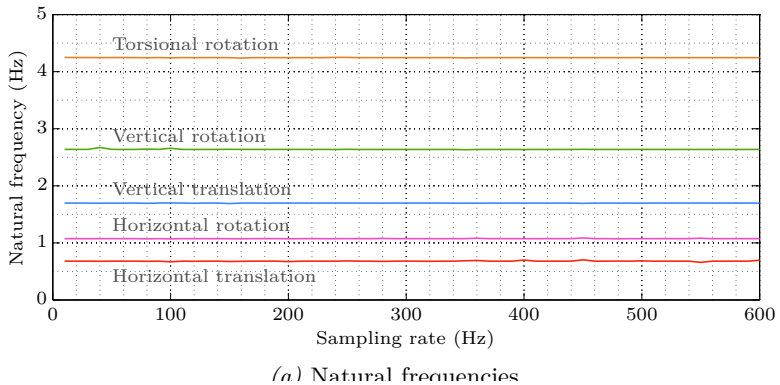

(a) Natural frequencies

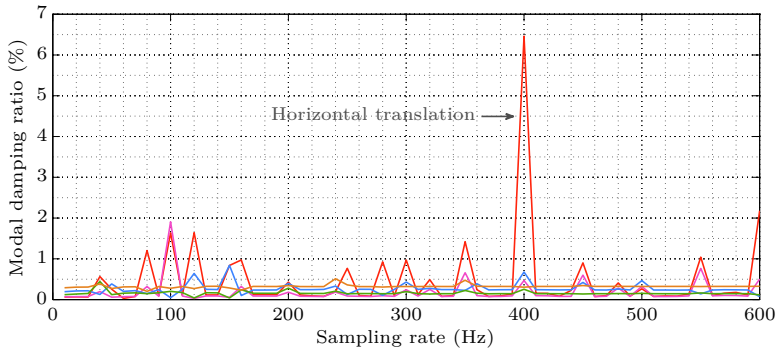

(b) Modal damping ratios

Figure 4.34: Effect of sampling rate on N4SID identification.

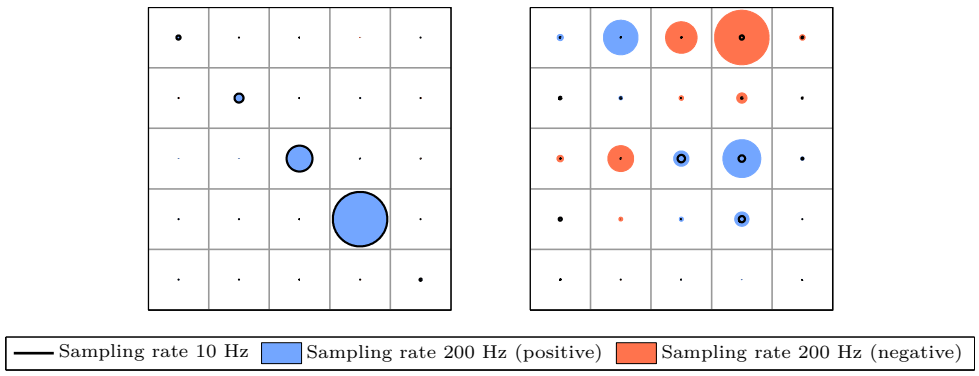

(a) Stiffness matrix *(b)* Damping matrix

Figure 4.35: Relative changes of structural matrices identified by the N4SID method when sampling rate is changed from 200 Hz to 10 Hz. Radius is proportional to value.

4.3.2.3 Number of lags for covariance estimates

Figure 4.36 shows the natural frequencies and modal damping ratios for increasing number of lags, and it is evident that the damping ratios deviates more from the values estimated by logarithmic decrements if the number of lags increases.

According to Hoen [17], at least one period of all natural periods should be encompassed by the maximum number of lags for covariance estimates. Thus, that is the number of lags used in CBHM identification in subsequent sections.

4.3.3 Verification based on simulated data

To verify the accuracy of the methods with the optimised parameters, they are tested on simulated data where the stiffness and damping matrix are known.

Time series are sampled at 200 Hz, and initially excited by the initial displacements summarised in Table 4.12.

Mode	Initial displacement	
Horizontal translation	0.100	m
Horizontal rotation	0.050	rad
Vertical translation	0.060	m
Vertical rotation	0.050	rad
Torsional rotation	0.200	rad

Table 4.12: Initial displacement for free vibration response simulations.

4.3.3.1 Record length

System identification based on free vibration response presents a challenge, since the higher modes dampen out relatively fast. This effect is even more severe if the section model is placed in a steady air flow, since motion induced aerodynamic damping can be much stronger than structural damping inherent in the rig. Hence, it is imperative to investigate the performance of the two methods for short displacement records.

Figure 4.38 clearly shows that the CBHM method need long time series to estimate damping accurately. More precisely, the quality of damping estimates is dependent on number of oscillation cycles. It is seen that the CBHM method eventually estimates the damping of lower modes correctly, but the displacement records have to be 20 minutes long to achieve that. Moreover, long records disturbs the identification of the torsional mode, since free vibration response of this mode is more or less damped out after 30 seconds.

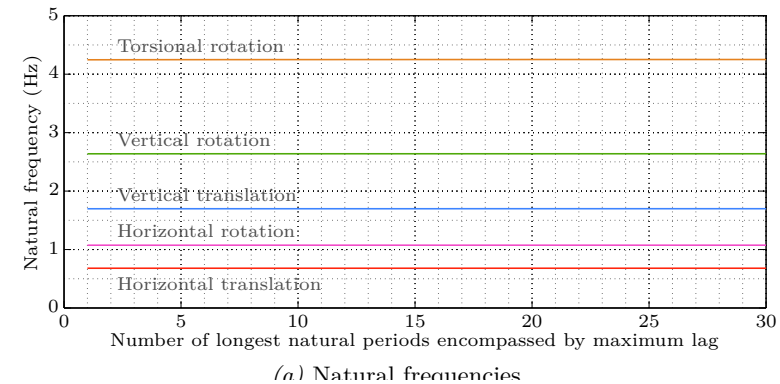

(a) Natural frequencies

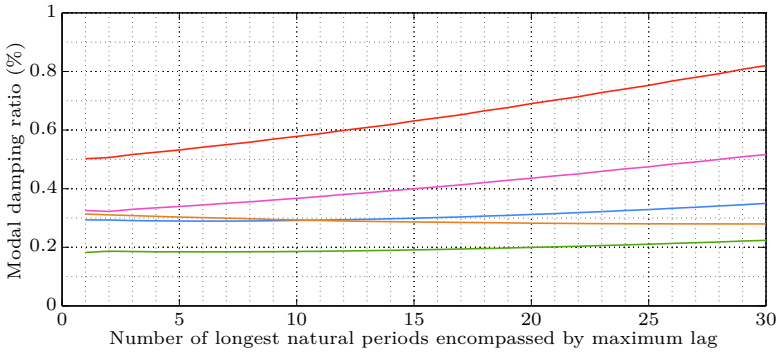

(b) Modal damping ratios

Figure 4.36: Effect of maximum lag for covariance estimates on CBHM identification.

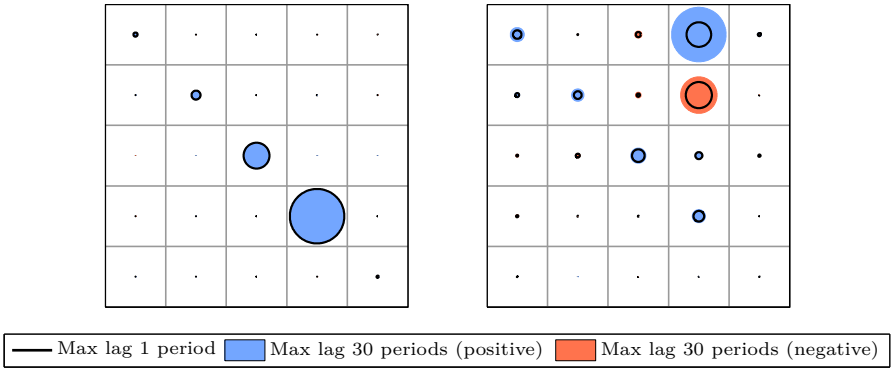

(a) Stiffness matrix *(b)* Damping matrix

Figure 4.37: Relative changes of structural matrices identified by the CBHM method when maximum lag for covariance estimates is changed from 1 to 30 times the longest natural period. Radius is proportional to value.

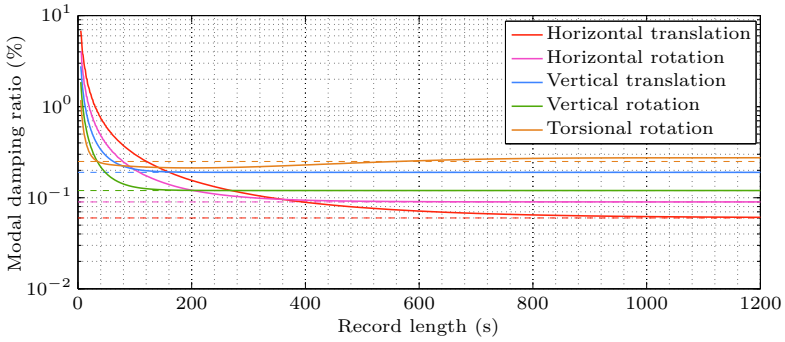

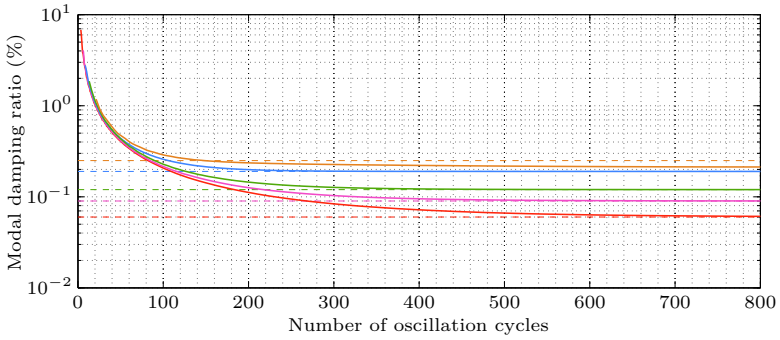

(a) CBHM

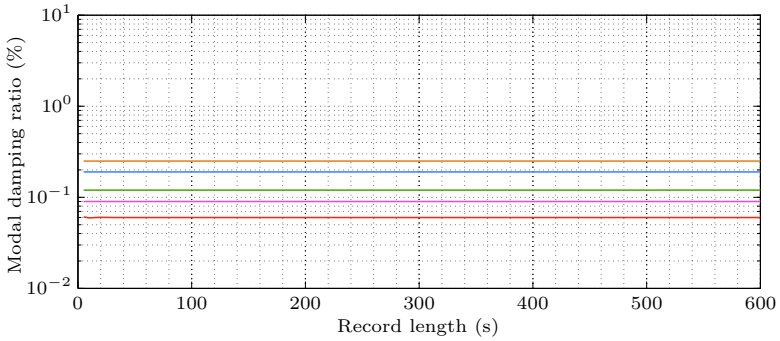

(b) N4SID

Figure 4.38: Effect of displacement record length and number of oscillation cycles on modal damping ratios. Exact values are indicated by dashed lines.

According to the figure, the optimal free vibration record length to capture the dynamic properties of the prototype is 10 minutes, but the identified damping ratios do not match the true values perfectly. In contrast, the N4SID method identifies the damping ratios of the simulated displacements with high accuracy based on a five seconds long record.

Because the torsional mode was *completely* dampened out after about 10 minutes, the N4SID method encountered numerical issues for longer records.

4.3.3.2 Noise

By simulating 60 and 300 seconds time series based on the natural frequencies and damping ratios estimated by the preliminary analysis, the natural frequencies, damping ratios and damping matrices shown in Figure 4.39 was identified.

Introduction of white noise introduces major cross terms, as shown in Figure 4.40. It is evident that the distortion is related to the lowest mode. Because lower modes are (over)determined by more samples per period than the other modes, they are more sensitive to noise; i.e. lower modes have a higher degree of distortion than higher modes.

4.4 Dynamic properties in still air

To determine the aerodynamic derivatives of the section model, it is necessary to obtain accurate and consistent estimates of the damping and stiffness matrix. Thus, accurate identification of the full structural matrices is important. Modal damping ratios and natural frequencies reflects the main dynamic characteristics of the systems, but do not provide any information on coupling between modes. It should be remembered that system identification of full structural matrices requires a correct mass matrix.

In the previous section, it was evident that the performance of both the CBHM and N4SID method decreases significantly when noise was present in the signal. It is, however, an important difference between the simulated and measured response; simulations are contaminated with white noise, while the measured response mainly contains high frequency noise – which is removed by filtering.

The high frequency noise in the recorded time series was estimated to be 0.0-0.2 % RNS, primarily related to horizontal motion, and it was found that the main contribution is vibration of horizontal springs. Electrical noise was extremely weak.

The recorded time series shows no indication that the sixth mode, longitudinal translation, is observable in the signal. Hence, the assumption of five modal degrees of freedom seems justified.

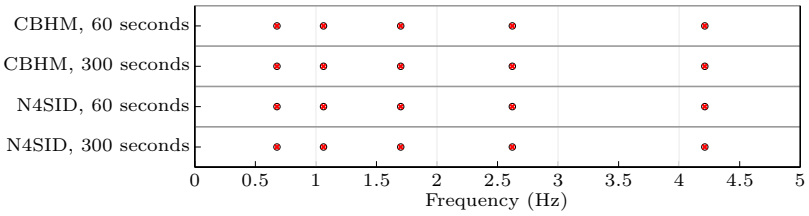

(a) Natural frequencies

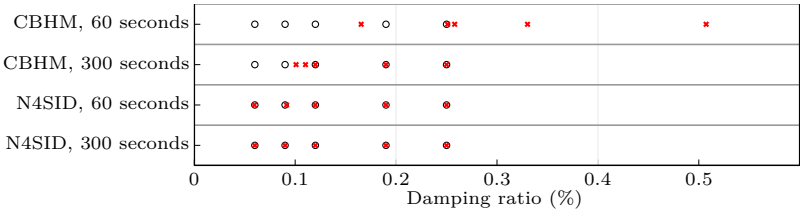

(b) Modal damping ratios

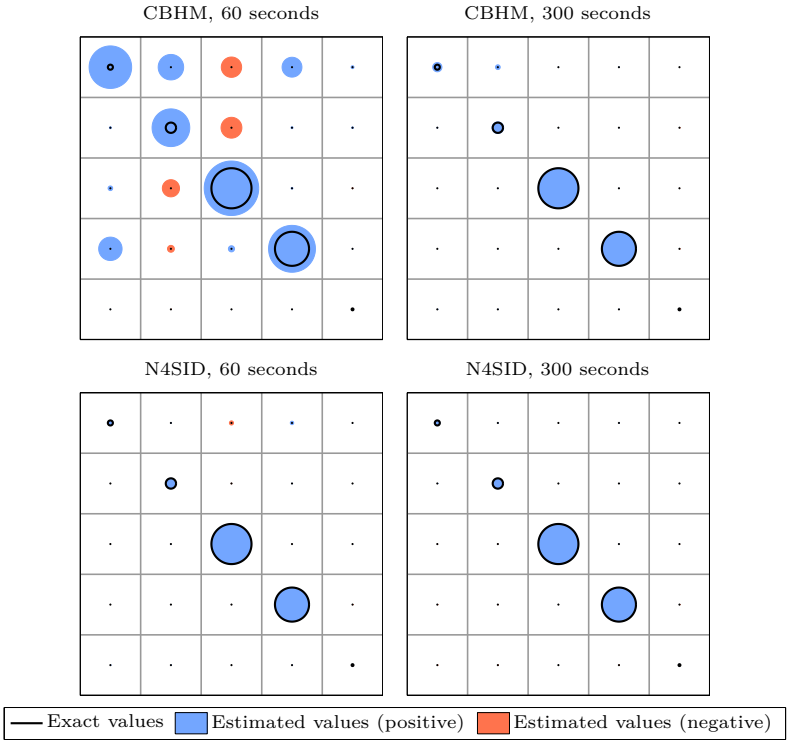

(c) Damping matrix. Radius is proportional to value.

Figure 4.39: Identification based on simulated *noise-free* displacement records of various lengths; compared with each other and to exact values. Free vibration response.

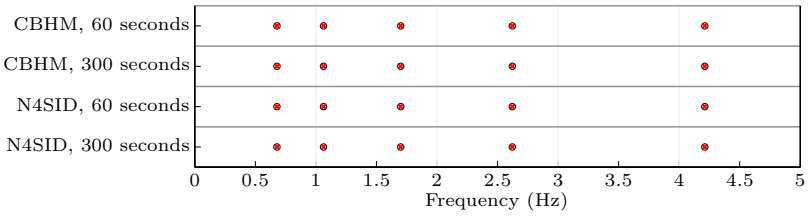

(a) Natural frequencies

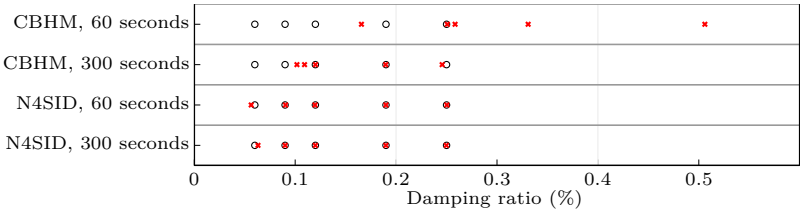

(b) Modal damping ratios

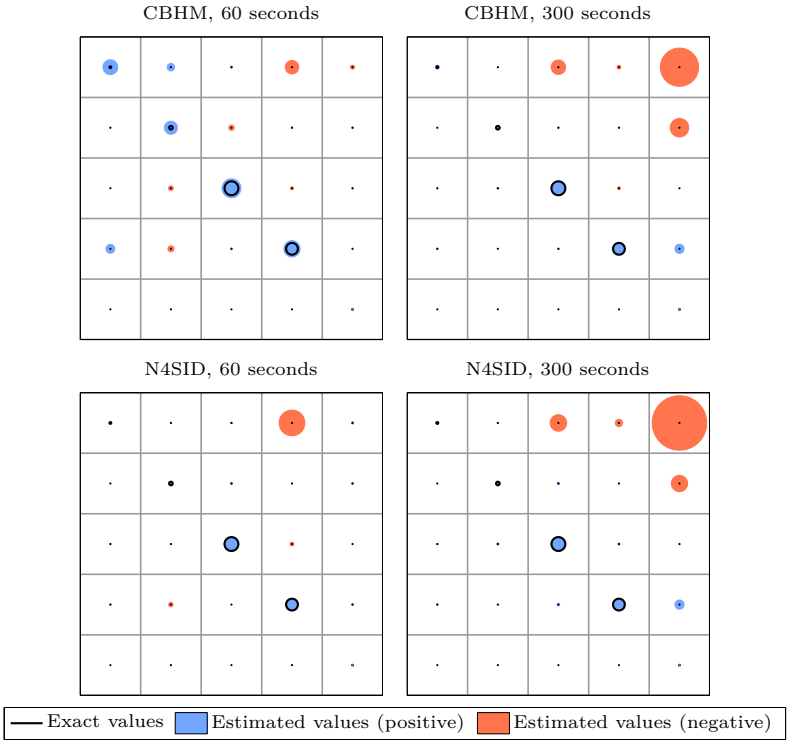

(c) Damping matrix. Radius is proportional to value.

Figure 4.40: Identification based on simulated *noisy* (1% RNS) displacement records of various lengths; compared with each other and to exact values. Free vibration response.

4.4.1 Modal quantities

4.4.1.1 Natural frequencies

To ensure that the main characteristics of the section model is accurately recovered, the identified natural frequencies of three independent records of free vibration response are compared in Table 4.13 and Figure 4.41.

The results are extremely consistent regarding the estimated frequencies, and it is clear that the analytical mass and stiffness matrix estimates represent the main dynamic characteristics of the system accurately, as the mean deviation of natural frequencies is as low as 0.5 % for all sets of recorded displacements. If the uninteresting horizontal and vertical rotation modes are excluded, the mean deviation drops to 0.3 %.

The torsional moment of inertia can be altered by adding extra weights to the rotation arms, and the rotational stiffness is nearly proportional to the wire distance squared (geometric contributions are not proportional). To gain further confidence in the mass and stiffness calculations, the torsional natural frequency was identified for two altered configurations:

Mode	Analytical	CBHM			N4SID		
		Set 1	Set 2	Set 3	Set 1	Set 2	Set 3
Horizontal translation	0.68	0.68	0.68	0.68	0.68	0.68	0.68
Horizontal rotation	1.06	1.07	1.07	1.08	1.07	1.07	1.08
Vertical translation	1.70	1.70	1.70	1.70	1.70	1.70	1.70
Vertical rotation	2.62	2.64	2.64	2.64	2.64	2.64	2.64
Torsional rotation	4.23	4.25	4.25	4.25	4.25	4.25	4.25

(a) Analytical and identified natural frequencies, given in Hz.

Mode	CBHM			N4SID		
	Set 1	Set 2	Set 3	Set 1	Set 2	Set 3
Horizontal translation	0.24	0.25	0.28	0.25	0.25	0.28
Horizontal rotation	1.02	1.02	1.20	1.01	1.02	1.19
Vertical translation	−0.19	−0.18	−0.20	−0.17	−0.16	−0.18
Vertical rotation	0.61	0.60	0.57	0.61	0.61	0.58
Torsional rotation	0.44	0.49	0.44	0.50	0.54	0.49
Mean (absolute) deviation	0.50	0.51	0.54	0.51	0.52	0.55

(b) Deviation of identified frequencies with respect to analytical values, given in %.

Table 4.13: Natural frequencies identified from three sets of recorded displacements (small amplitudes) during 60 seconds of free vibration.

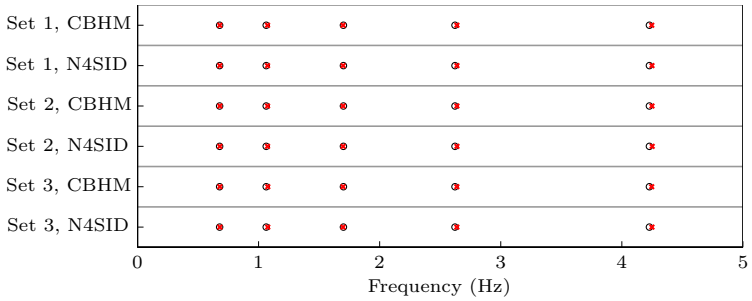

Figure 4.41: Natural frequencies identified from three sets of recorded displacements (small amplitudes) during 60 seconds of free vibration. Compared to analytical values.

1. Additional weights of 43 g was added with their centre of gravity 367 mm from the centre line of the extension arms; two on each arm, four in total. This gave the following increase of moment of inertia:

$$I_{\text{add}} = 4 \cdot 0.043 \text{ kg} \cdot (0.367 \text{ m})^2 = 0.023 \text{ kg·m}^2$$

2. The distance between the vertical wires was changed from 576 mm to 478 mm, i.e. a decrease of 17 %. This mainly changes the torsional stiffness, but a minor change of moment of inertia is also introduced, since the mass of springs and wire brackets are moved closer to the rotation axis.

The analytical and identified natural frequencies of the default and two altered configurations are shown in Table 4.14. It is clear that the analytical values also here matches the identified values with a high degree of accuracy. It should be noted that the agreement between analytical and estimated frequencies (particularly by the CBHM method) is consistently better when only the torsional mode is excited than all modes excited – although the improvement is small.

4.4.1.2 Modal damping ratios

In contrast to mass and stiffness, which are subject to well-defined (macro level) physical laws, the damping of the system is much harder to predict. Damping stems from several sources, where the most important structural source is internal friction in the spring and wire material. This damping is difficult to predict; mainly because it is introduced by complicated mechanisms within the material, and partially because it is simplified to be represented as viscous (velocity proportional) damping

Table 4.15 and Figure 4.42 gives the identified damping ratios of the three sets of (small amplitude) displacement records. Like in section 4.3.3.1, it is evident that damping estimated by the CBHM method is dependent on number of recorded oscillations of each mode, as the difference between estimates decreases for higher modes. Looking at

the damping ratio of the vertical translation mode, where the amplitude of set 2 and 3 is twice as big as the amplitude of set 1, another important source of damping reveals itself; the (aerodynamic) damping of air increases when the amplitude is increased, because higher velocity is required to maintain the frequency.

The differences between the damping estimates of the CBHM and N4SID method are illustrated in Figure 4.43, and it is clear that the CBHM method produces poor estimates of the modal damping ratios, particularly for lower modes. This is obviously because fewer cycles of motion are recorded for lower modes than for higher modes.

Aerodynamic damping is also apparent, although barely, as the damping of the signal is

Mode	Analytical	CBHM			N4SID		
		Set 1	Set 2	Set 3	Set 1	Set 2	Set 3
Unmodified	4.23	4.24	4.24	4.24	4.24	4.25	4.25
Additional mass	4.00	4.02	4.02	4.02	4.02	4.02	4.02
Shorter wire distance	3.60	3.61	3.61	3.61	3.61	3.61	3.62

(a) Analytical and identified natural frequencies, given in Hz.

Mode	CBHM			N4SID		
	Set 1	Set 2	Set 3	Set 1	Set 2	Set 3
Unmodified	0.33	0.36	0.33	0.41	0.43	0.42
Additional mass	0.38	0.39	0.34	0.48	0.49	0.45
Shorter wire distance	0.30	0.32	0.35	0.40	0.42	0.45
Mean (absolute) deviation	0.34	0.36	0.34	0.43	0.45	0.44

(b) Deviation of identified frequencies with respect to analytical values, given in %.

Table 4.14: Natural frequency of torsional rotation obtained for various configurations. Identifications are based recorded displacements (small amplitudes) during 60 seconds of free vibration of the torsional mode only.

Mode	CBHM			N4SID		
	Set 1	Set 2	Set 3	Set 1	Set 2	Set 3
Horizontal translation	0.50	0.50	0.50	0.06	0.05	0.06
Horizontal rotation	0.33	0.32	0.33	0.07	0.07	0.07
Vertical translation	0.29	0.36	0.37	0.19	0.27	0.27
Vertical rotation	0.18	0.20	0.21	0.12	0.14	0.15
Torsional rotation	0.31	0.34	0.36	0.29	0.32	0.33

Table 4.15: Modal damping ratios, given in %, identified from three sets of recorded displacements (small amplitudes) during 60 seconds of free vibration.

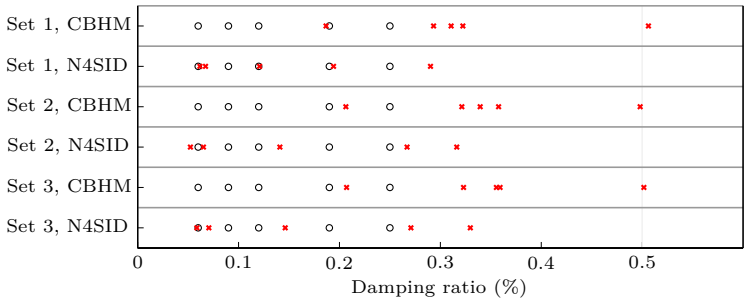

Figure 4.42: Modal damping ratios identified from three sets of recorded displacements (small amplitudes) during 60 seconds of free vibration. Compared to preliminary estimates.

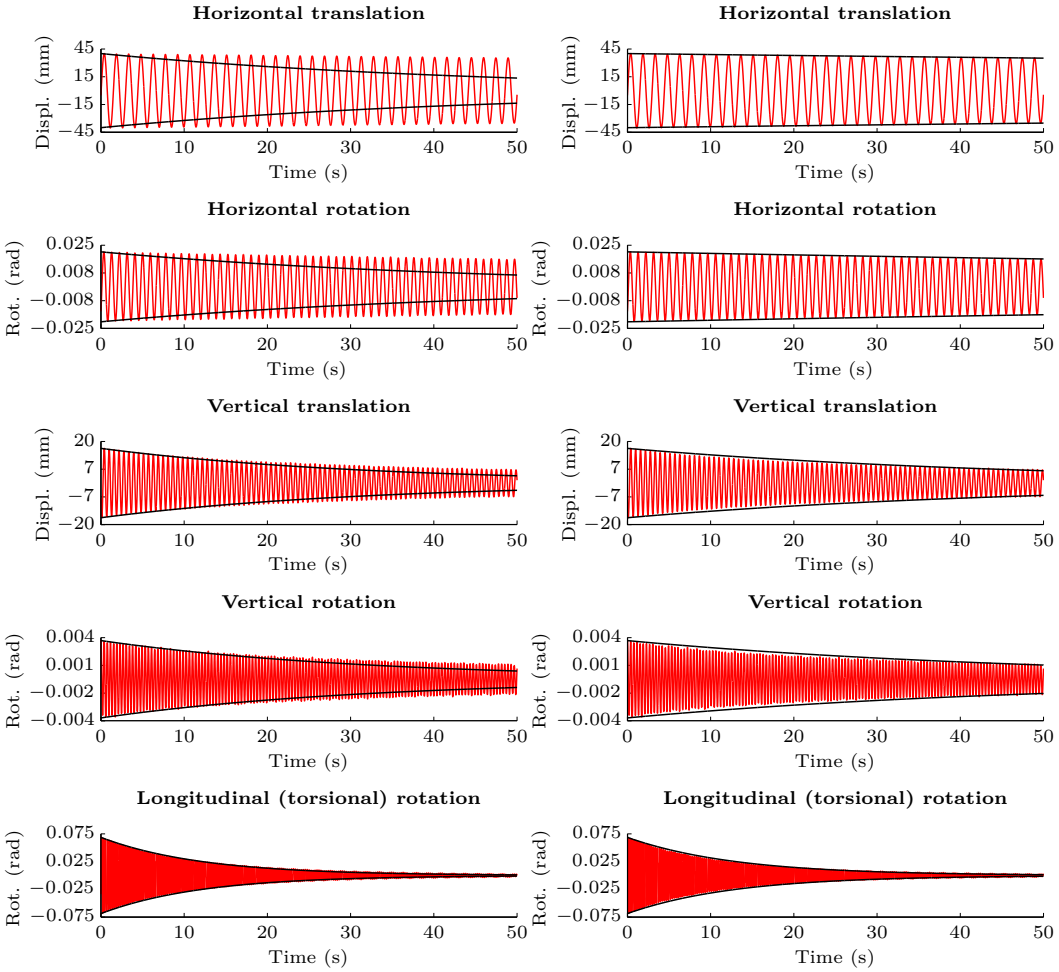

(a) CBHM method *(b)* N4SID method

Figure 4.43: Verification of damping ratios identified from set 1 of recorded displacements. Amplitude limits due to estimated damping are indicated by black curves.

stronger than estimated at the beginning, and weaker at the end; it is stronger for larger amplitudes and lower for smaller amplitudes.

4.4.1.3 Mode shapes

The mode shapes are illustrated in Figure 4.44, and it is clear that they represent rigid body motion. This is also confirmed by Table 4.16, where it is seen that each mode comprise motion in virtually one degree of freedom only.

It is also seen that the identified mode shapes matches fairly well with the analytical shapes. Due to the low damping, the imaginary components of the shapes are very small, and the absolute values are approximately equal to the real values.

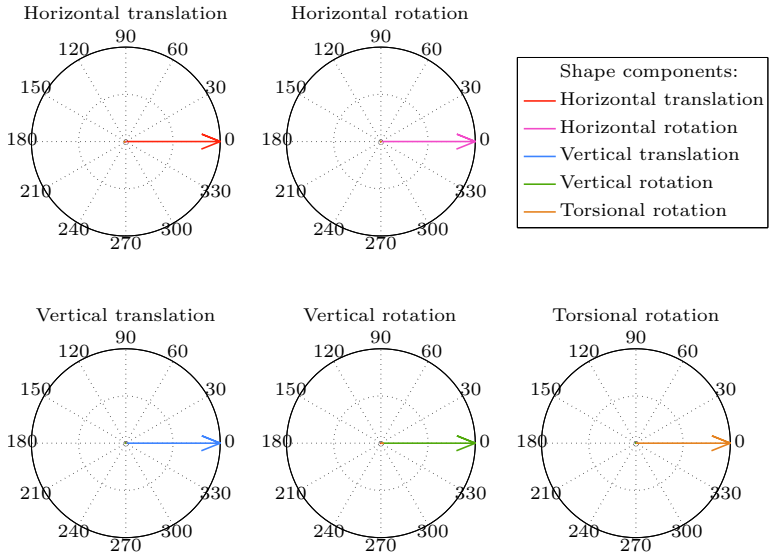

Figure 4.44: Damped (complex) mode shapes estimated by the N4SID method. Because of low damping and the rigidity of the section model, all modes are dominated by one real component.

4.4.2 Stiffness matrix

The analytical and identified modal stiffness matrices are given in Table 4.17, and it is seen that the identification gives consistent results that are matching the analytical matrix well. It is also observed that they are fairly symmetric, although not perfectly. In general, cross terms below the diagonal are approximately zero, while cross terms above the diagonal, particularly between horizontal translation and torsional rotation, are more significant - although small compared to diagonal terms. The relation between the horizontal and torsional mode was observed directly in the laboratory; due to imperfections in the setup, horizontal translation induces a small torsional rotation. This may distort the determination of aerodynamic derivatives, particularly P_3^*.

Degree of freedom	Mode 1	Mode 2	Mode 3	Mode 4	Mode 5
Horizontal translation	1.000	0.001	0.000	0.000	0,002
Horizontal rotation	0.001	1.000	0.000	0.000	0.000
Vertical translation	0.000	0.000	1.000	0.006	0.000
Vertical rotation	0.000	0.000	0.007	1.000	0.000
Torsional rotation	0.017	0.000	0.020	0.019	1.000

(a) Analytical (undamped shapes)

Degree of freedom	Mode 1	Mode 2	Mode 3	Mode 4	Mode 5
Horizontal translation	1.000	0.002	0.002	0.003	0,002
Horizontal rotation	0.004	1.000	0.001	0.004	0.000
Vertical translation	0.001	0.000	1.000	0.008	0.001
Vertical rotation	0.000	0.001	0.004	1.000	0.001
Torsional rotation	0.015	0.003	0.007	0.022	1.000

(b) Record set 1

Degree of freedom	Mode 1	Mode 2	Mode 3	Mode 4	Mode 5
Horizontal translation	1.000	0.003	0.003	0.007	0,001
Horizontal rotation	0.004	1.000	0.001	0.003	0.000
Vertical translation	0.001	0.001	1.000	0.003	0.001
Vertical rotation	0.000	0.001	0.003	1.000	0.002
Torsional rotation	0.015	0.002	0.006	0.025	1.000

(c) Record set 2

Degree of freedom	Mode 1	Mode 2	Mode 3	Mode 4	Mode 5
Horizontal translation	1.000	0.004	0.002	0.003	0,001
Horizontal rotation	0.002	1.000	0.001	0.004	0.001
Vertical translation	0.001	0.001	1.000	0.003	0.001
Vertical rotation	0.000	0.001	0.003	1.000	0.002
Torsional rotation	0.015	0.003	0.006	0.027	1.000

(d) Record set 3

Table 4.16: Component magnitudes of the complex mode shapes, determined analytically and identified from three sets of recorded displacements (small amplitudes) during 60 seconds of free vibration.

$$\begin{bmatrix} 260.9 & 0 & 0 & 0 & 0 \\ 0 & 560.1 & 0 & 0 & 0 \\ 0 & 0 & 1651.4 & 0 & 0 \\ 0 & 0 & 0 & 3424.7 & 0 \\ 0 & 0 & 0 & 0 & 142.0 \end{bmatrix}$$

(a) Analytical

$$\begin{bmatrix} 261.5 & -4.5 & 5.4 & -6.4 & -15.5 \\ 2.0 & 570.7 & -4.3 & 23.3 & -1.3 \\ -1.8 & 1.3 & 1645.0 & 6.5 & 4.0 \\ 0.3 & 1.8 & 7.0 & 3466.1 & -7.0 \\ 2.1 & 0.4 & -0.8 & -2.1 & 143.2 \end{bmatrix}$$

(b) Set 1, CBHM

$$\begin{bmatrix} 261.4 & 0.7 & -3.1 & -7.9 & -20.0 \\ 1.0 & 570.7 & -0.6 & 10.2 & -1.4 \\ -1.1 & -0.1 & 1645.6 & 15.1 & 7.0 \\ 0.2 & 2.1 & 7.4 & 3466.5 & -6.4 \\ 2.2 & 0.4 & -0.8 & -1.9 & 143.4 \end{bmatrix}$$

(c) Set 1, N4SID

$$\begin{bmatrix} 261.6 & -3.3 & -7.6 & -114.0 & -9.8 \\ 2.0 & 570.7 & -3.6 & -39.4 & 3.4 \\ -1.0 & 2.9 & 1645.7 & 23.7 & -1.5 \\ 0.3 & 3.4 & 6.0 & 3466.2 & -7.7 \\ 2.1 & 0.3 & -0.7 & -2.4 & 143.4 \end{bmatrix}$$

(d) Set 2, CBHM

$$\begin{bmatrix} 261.6 & 1.3 & -3.7 & 9.1 & -9.4 \\ 1.1 & 570.7 & -0.6 & 8.6 & -0.5 \\ -1.7 & 1.0 & 1646.0 & 1.0 & -3.5 \\ -0.1 & 3.0 & 5.8 & 3466.6 & -8.3 \\ 2.1 & 0.3 & -0.7 & -2.2 & 143.5 \end{bmatrix}$$

(e) Set 2, N4SID

$$\begin{bmatrix} 261.7 & 16.4 & -5.6 & -39.5 & -14.2 \\ 0.6 & 572.7 & 0.6 & 14.3 & 5.3 \\ -0.9 & -3.5 & 1644.8 & 10.7 & 0.5 \\ 0.7 & 1.7 & 5.8 & 3464.0 & -7.7 \\ 2.1 & 0.4 & -0.7 & -2.4 & 143.2 \end{bmatrix}$$

(f) Set 3, CBHM

$$\begin{bmatrix} 261.8 & 1.4 & -2.7 & 9.5 & -11.5 \\ 0.8 & 572.7 & -0.6 & 9.9 & 2.6 \\ -1.1 & 1.0 & 1645.3 & 3.4 & -5.0 \\ 0.6 & 3.3 & 6.3 & 3464.5 & -8.4 \\ 2.1 & 0.3 & -0.7 & -2.4 & 143.3 \end{bmatrix}$$

(g) Set 3, N4SID

Table 4.17: Analytical and identified stiffness matrix, identified from three sets of recorded displacements (small amplitudes) during 60 seconds of free vibration.

4.4.3 Damping matrix

The analytical and identified modal damping matrices are given in Table 4.18. They are not as consistent as the stiffness estimates, and they are less symmetric – particularly those identified by the CBHM method. As seen in section 4.3.3, the CBHM method needs long time series to produce decent estimates, but the response time series used here are only 60 seconds long. Longer time series would decrease accuracy of estimates related to torsional rotation.

To get a visual overview of the damping matrices, they are illustrated in Figure 4.45, where false cross terms are evident. It is particularly interesting to see that the major cross terms are related to the uninteresting rotational modes, although a coupling between the horizontal and torsional mode can be suspected. Aerodynamic damping of the vertical translational mode in set 2 and 3 is evident, but it is clear that the CBHM method over-estimates the damping of all modes.

It should be noted that identification where uninteresting modes have been removed from the recorded output was found to produce the same result as by discarding uninteresting terms from matrices identified from response of all modes.

$$\begin{bmatrix} 0.615 & -0.067 & -0.342 & 2.006 & 0.238 \\ 0.284 & 0.548 & -0.235 & -1.916 & -0.009 \\ -0.151 & -0.282 & 0.907 & 0.579 & -0.175 \\ -0.169 & -0.057 & -0.069 & 0.780 & -0.011 \\ 0.046 & 0.011 & 0.006 & 0.017 & 0.033 \end{bmatrix}$$

(a) Set 1, CBHM

$$\begin{bmatrix} 0.072 & -0.028 & -0.050 & -0.344 & 0.142 \\ 0.201 & 0.114 & -0.011 & -0.121 & 0.104 \\ 0.038 & -0.059 & 0.602 & 0.531 & -0.154 \\ -0.258 & -0.018 & -0.011 & 0.503 & -0.007 \\ 0.047 & 0.006 & 0.000 & 0.013 & 0.031 \end{bmatrix}$$

(b) Set 1, N4SID

$$\begin{bmatrix} 0.619 & 0.610 & -0.506 & -0.348 & 0.012 \\ 0.214 & 0.542 & -0.193 & 0.337 & -0.001 \\ -0.248 & -0.075 & 1.104 & 0.385 & 0.063 \\ -0.223 & 0.017 & 0.087 & 0.853 & 0.029 \\ 0.039 & -0.001 & -0.011 & -0.001 & 0.037 \end{bmatrix}$$

(c) Set 2, CBHM

$$\begin{bmatrix} 0.060 & 0.036 & 0.104 & 1.531 & -0.106 \\ 0.143 & 0.110 & 0.004 & -0.029 & -0.066 \\ -0.029 & -0.007 & 0.823 & -0.357 & 0.158 \\ -0.192 & 0.015 & 0.131 & 0.589 & 0.049 \\ 0.039 & -0.008 & -0.020 & 0.009 & 0.034 \end{bmatrix}$$

(d) Set 2, N4SID

$$\begin{bmatrix} 0.614 & -2.042 & -0.830 & 1.625 & 0.197 \\ -0.054 & 0.551 & 0.115 & -0.667 & -0.001 \\ -0.244 & 0.241 & 1.108 & -0.064 & -0.187 \\ -0.023 & -0.176 & 0.008 & 0.866 & -0.028 \\ 0.004 & 0.008 & -0.001 & 0.009 & 0.038 \end{bmatrix}$$

(e) Set 3, CBHM

$$\begin{bmatrix} 0.076 & 0.082 & -0.076 & -0.026 & 0.279 \\ -0.028 & 0.119 & -0.015 & -0.147 & 0.188 \\ -0.096 & 0.077 & 0.837 & 0.361 & -0.086 \\ 0.022 & 0.028 & 0.064 & 0.609 & 0.007 \\ 0.005 & -0.031 & -0.001 & 0.011 & 0.035 \end{bmatrix}$$

(f) Set 3, N4SID

Table 4.18: Damping matrix identified from three sets of recorded displacements (small amplitudes) during 60 seconds of free vibration.

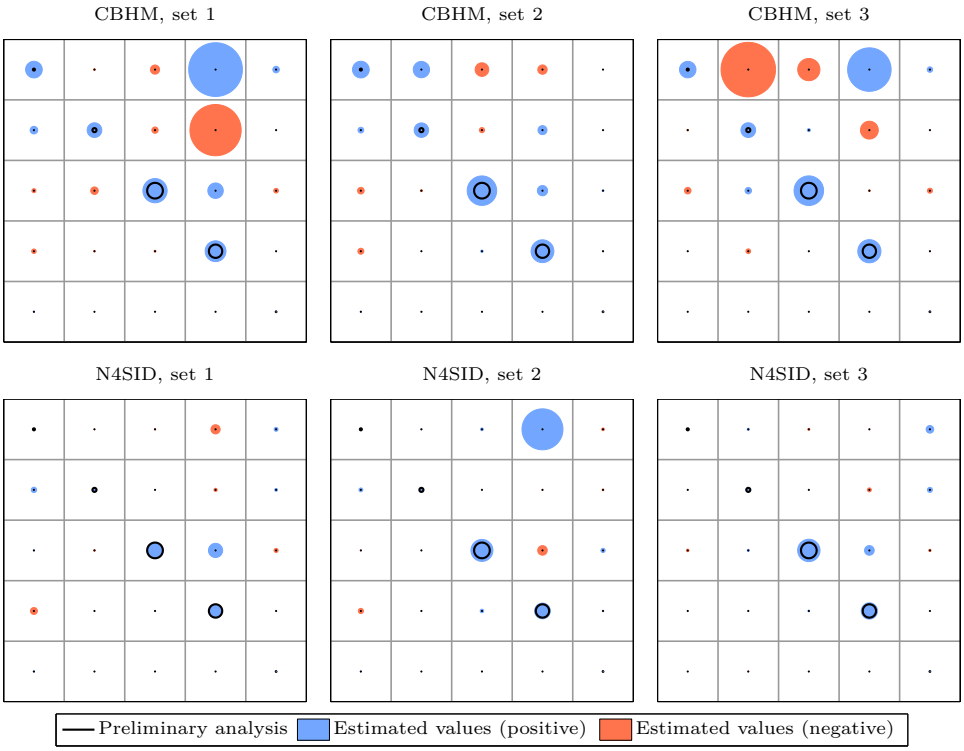

(a) Full damping matrix

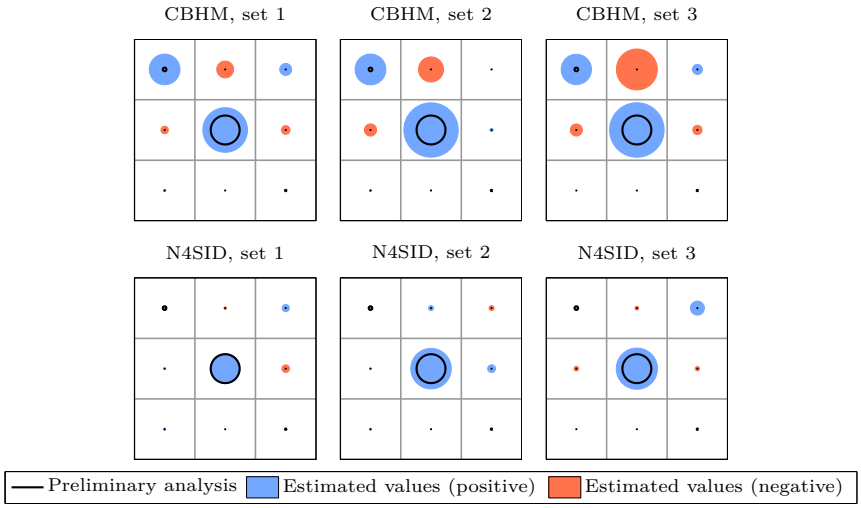

(b) Reduced damping matrix (only modes relevant to determine ADs)

Figure 4.45: Damping matrix identified from three sets of recorded displacements (small amplitudes) during 60 seconds of free vibration. Compared to values obtained from set 1 in preliminary analysis. Radius is proportional to value.

4.5 Effect of static displacements

A major issue with the experimental setup examined in this work, is that displacements of the section model alters the stiffness of the system. The largest changes occurs for horizontal displacements. When the section model is displaced horizontally, two things happen: the vertical springs are elongated, which in turn increases the tension in the vertical suspensions. Hence, the vertical springs contribute to the horizontal stiffness, and the geometric stiffness increases.

4.5.1 Natural frequencies

Assuming (infinitely) small amplitudes, changes are induced by static displacements due to mean wind velocity pressure acting on the model. Derivation of an analytical stiffness matrix considering the effect of displacements is given in Appendix A, although it suffer from some minor flaws regarding rotational displacements. To illustrate the strengths and flaws of the analytical model, it is compared to results obtained from the Abaqus/CAE model. However, the FE model does not provide the stiffness matrix directly; only natural frequencies are given.

The comparisons in Figure 4.46 and Figure 4.47 give a good indication of the displacement effects. Given that the FE model provides a good representation of the prototype, it is clear that the effects of translational displacements are estimated correctly by the derived analytical solution, but the effect of rotation on rotational modes are estimated incorrectly. It should be noted that the effect of vertical translation is not symmetric

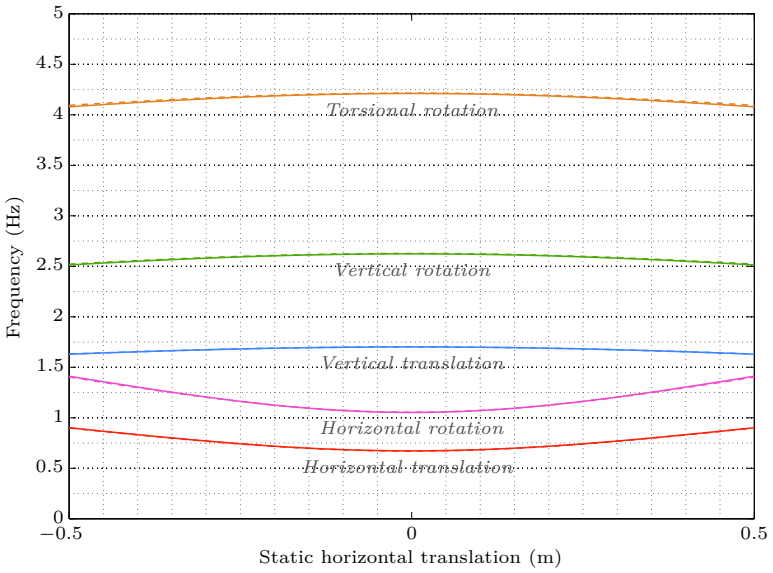

Figure 4.46: Natural frequencies as function of static horizontal translation.

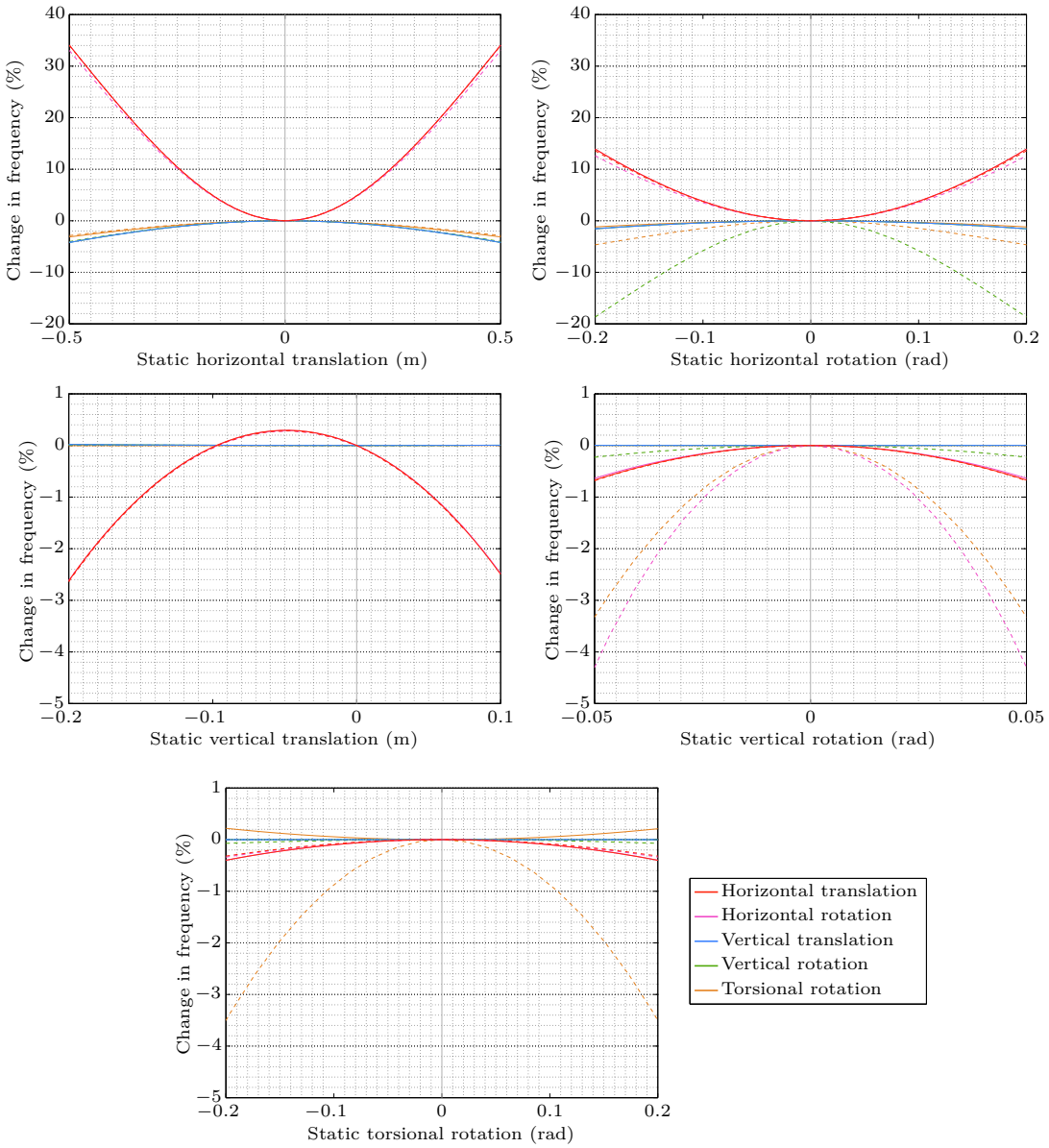

Figure 4.47: Change in natural frequencies as function of static displacements. Analytical values are indicated by solid lines, Abaqus/CAE simulations by dashed lines. Vertical translation is positive downwards.

about the resting position of the section model, because at rest, the tension in the upper suspensions is higher than the tension in the lower suspensions, as they carry the weight of the section model. An upwards displacement of approximately 50 mm gives equal tension in all suspensions.

4.5.2 Correction

To determine the aerodynamic derivatives of the section model, it was in equation (2.11d) assumed that

$$\mathbf{K}_{\text{eff}} = \mathbf{K}_0 + \mathbf{K}_{ae}$$

However, because of the effect of static displacements, this must now be rewritten to

$$\mathbf{K}_{\text{eff}} = \mathbf{K}_{\text{eff},0} - \Delta\mathbf{K}(\bar{\mathbf{r}}) = \mathbf{K}_0 + \mathbf{K}_{ae} \tag{4.84}$$

where $\mathbf{K}_{\text{eff},0}$ is the identified stiffness matrix and $\Delta\mathbf{K}$ represents the change in stiffness induced by the static displacements $\bar{\mathbf{r}}$. Hence, to obtain the ADs of the section model, it is necessary to determine $\Delta\mathbf{K}(\bar{\mathbf{r}})$.

It is proposed to estimate the change of stiffness by computing the modal stiffness matrix corresponding to measured static displacements, and subtracting the matrix corresponding to zero displacements. The modal matrices should be based on the mass matrix derived from Table 3.8 and the analytical stiffness matrix derived in Appendix A. Thus,

$$\Delta\mathbf{K}(\bar{\mathbf{r}}) = \mathbf{K}_{\text{analytical}}(\bar{\mathbf{r}}) - \mathbf{K}_{\text{analytical}}(\mathbf{0}) \tag{4.85}$$

To verify the correction procedure, a simulation was conducted in Abaqus/CAE, where the section model was loaded with the *buffeting wind velocity pressure* of a Monte Carlo-simulated turbulent wind field with mean velocity of 20 m/s. Properties of the wind field were resembling the conditions described in [50], and the frequency content of the simulated wind field does not fulfil the white noise assumption. The lack of motion induced forces gives a conservative estimate, as no aerodynamic damping was included. Theory behind the Monte Carlo simulation and details of the wind field are presented in Appendix B.

The static (mean) displacements of the simulated response are given in Table 4.19. The corresponding correction was estimated to be

$$\Delta\mathbf{K}(\bar{\mathbf{r}}) = \begin{bmatrix} 23.3 & 0.0 & 0.0 & 0.0 & 0.0 \\ 0.0 & 49.8 & 0.0 & 0.0 & 0.0 \\ 0.0 & 0.0 & -14.8 & 0.0 & 0.0 \\ 0.0 & 0.0 & 0.0 & -30.6 & 0.0 \\ 0.0 & 0.0 & 0.0 & 0.0 & -1.0 \end{bmatrix}$$

Mode	Static displacement	
Horizontal translation	0.154	m
Horizontal rotation	-0.002	rad
Vertical translation	-0.043	m
Vertical rotation	0.005	rad
Torsional rotation	-0.006	rad

Table 4.19: Static component of response obtained from simulated response of a turbulent wind field acting on the section model.

The stiffness matrix identified by the CBHM method (which produced highest accuracy in this case) was

$$\mathbf{K}_{\text{eff},0} = \begin{bmatrix} 275.1 & -24.3 & 22.8 & -4.0 & -101.7 \\ -1.5 & 588.4 & 0.8 & -34.4 & -7.1 \\ 14.0 & 16.7 & 1633.4 & 17.7 & -43.9 \\ -1.8 & -23.9 & -1.2 & 3390.6 & 29.0 \\ -2.6 & -0.2 & 2.7 & 0.1 & 138.7 \end{bmatrix}$$

and the corrected matrix becomes

$$\mathbf{K}_{\text{eff}} = \begin{bmatrix} 251.8 & -24.3 & 22.8 & -4.0 & -101.7 \\ -1.5 & 538.6 & 0.8 & -34.4 & -7.1 \\ 14.0 & 16.7 & 1648.1 & 17.7 & -43.9 \\ -1.8 & -23.9 & -1.2 & 3421.2 & 29.0 \\ -2.6 & -0.2 & 2.7 & 0.1 & 139.6 \end{bmatrix}$$

It is evident that the coupling between horizontal translation and torsional rotation, particularly, is considerably higher than for free vibration response.

The identified and corrected natural frequencies are given in Figure 4.48 and Table 4.20, and it is seen that the correction improves the identification significantly – although horizontal translational and rotational stiffness estimates are slightly over-corrected.

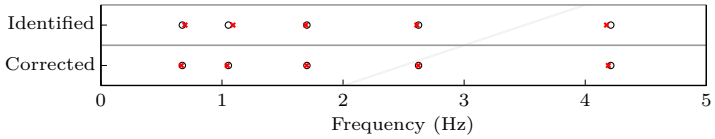

Figure 4.48: Identified and corrected natural frequencies obtained from simulated response of a turbulent wind field acting on the section model. Compared to analytical values.

Mode	Analytical	Identified	Corrected
Horizontal translation	0.67	0.69	0.66
Horizontal rotation	1.05	1.09	1.04
Vertical translation	1.70	1.69	1.70
Vertical rotation	2.62	2.61	2.62
Torsional rotation	4.21	4.18	4.19

(a) Analytical, identified and corrected natural frequencies, given in Hz.

Mode	Identified	Corrected
Horizontal translation	3.23	-1.26
Horizontal rotation	3.54	-0.94
Vertical translation	-0.56	-0.11
Vertical rotation	-0.54	-0.09
Torsional rotation	-0.83	-0.49
Mean (absolute) deviation	1.74	0.58

(b) Deviation of identified and corrected frequencies with respect to analytical values, given in %.

Table 4.20: Identified and corrected natural frequencies obtained from simulated response of a turbulent wind field acting on the section model.

4.6 Effect of excitation amplitudes

Since the stiffness of the system changes with displacements, it is obvious that the excitation amplitudes of the modes will affect the effective stiffness of the system, i.e. the stiffness identified by system identification. The effective stiffness can be considered an average of the continuously changing instantaneous stiffness. Since the instantaneous stiffness is non-linear with respect to static displacements, the effective stiffness is a function of both excitation amplitudes and static displacements.

4.6.1 Abaqus/CAE simulations

To gain first insight into this highly non-linear problem, simulations in Abaqus/CEA have been conducted. It is important to learn how large amplitudes in each degree of freedom affects the stiffness of the system. The test was carried out by first exciting all modes with small excitation amplitudes (0.01 meter or radians, whichever appropriate), before each mode successively was excited with it's maximum amplitude.

The maximum amplitudes of each degree of freedom are given in Table 4.21, and the corresponding natural frequencies are given in Figure 4.49. It is clear that the horizontal amplitude has the most impact on the modal stiffness – which was expected, given the results regarding static displacements in the previous section. However, it should be kept

Degree of freedom	Amplitude	
Horizontal translation	0.450	m
Horizontal rotation	0.150	rad
Vertical translation	0.080	m
Vertical rotation	0.050	rad
Torsional rotation	0.200	rad

Table 4.21: Maximum (physically feasible) excitation amplitudes of the prototype.

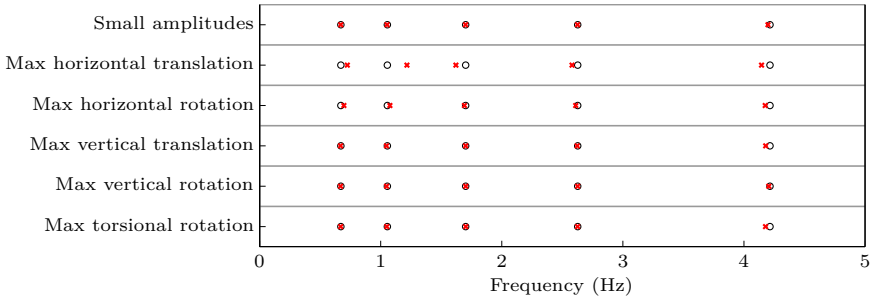

Figure 4.49: Effect of maximum excitation amplitude on the corresponding natural frequencies. Identified by the CBHM method, based on simulations performed by Abaqus/CAE.

in mind that the maximum horizontal amplitude is unduly large compared to amplitudes that can be expected in a wind tunnel.

4.6.2 Horizontal translation

Having learned that the horizontal translation amplitude has the most significant effect on the system stiffness, it was time to test it on the prototype. Three tests were carried out with a large horizontal excitation amplitude of approximately 0.450 m, and three tests with a smaller amplitude of approximately 0.250 m. The displacement record of a large amplitude test is shown in Figure 4.50, and a strong coupling between horizontal translation and torsional rotation is evident. This is most likely due to small imperfections in geometry and stiffness symmetry, which gives rise to torsional rotation for large horizontal displacements.

A significant beating effect can also be observed in the vertical translation amplitude. Beating occurs when two harmonics of slightly different frequencies interfere with each other. In this case, it may be caused by the fact that the vertical frequency changes with horizontal displacements; since the horizontal displacements at each end of the section model generally differ, the instantaneous vertical stiffness also differ.

In general, it was observed that large amplitudes decreased the quality of both measurements and identifications.

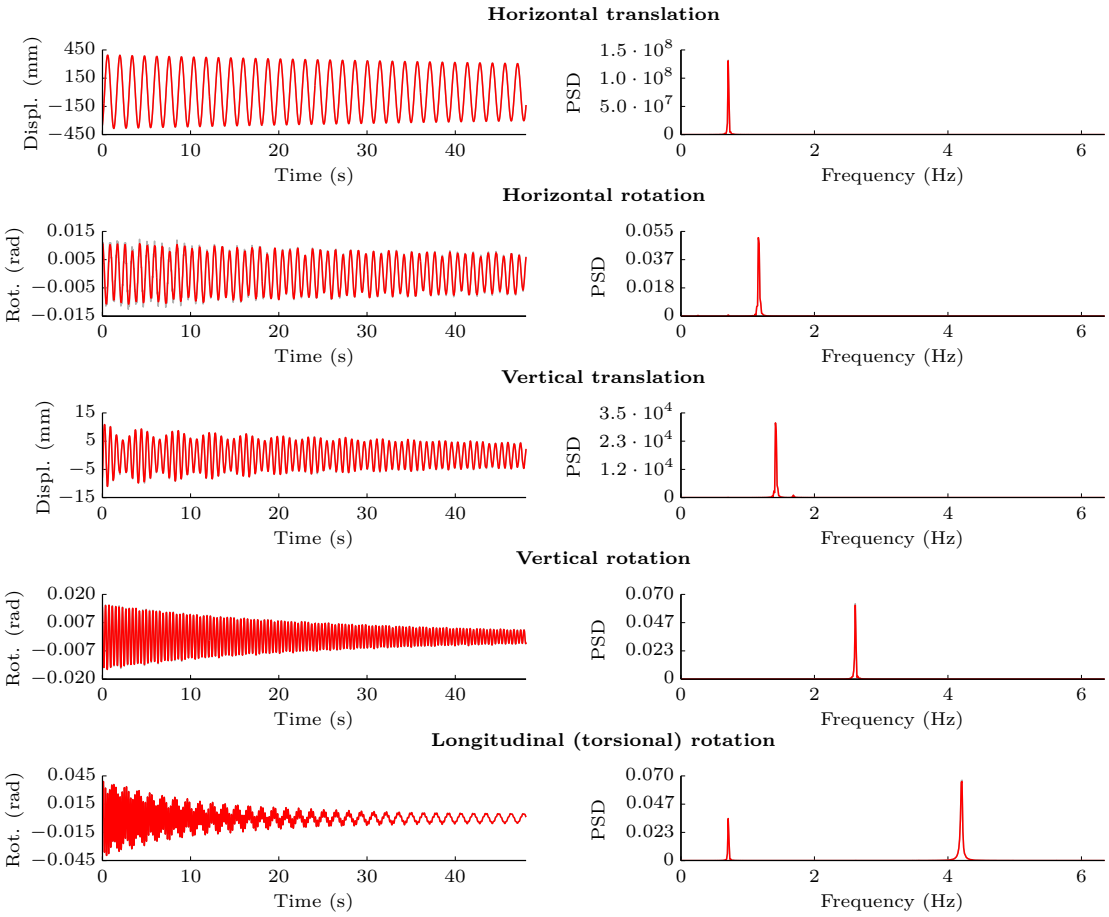

Figure 4.50: Free vibration response (large horizontal amplitude) and corresponding power spectra.

The identified natural frequencies of the six tests are given in Figure 4.51. Identification was performed with a sampling rate of 30 Hz instead of 10 Hz for these particular tests, as the N4SID method produced poor quality results with 10 Hz sampling rate.

The most conspicuous difference from the Abaqus model, is the drop of the vertical translation frequency. Otherwise, the effects are smaller than predicted by the Abaqus/CAE simulations. There are also signs of inconsistencies in the identified results; particularly the third set gives small variations in the estimates produced by the two methods. This is probably due to the increase in disturbances that follows the large amplitude.

Modal damping ratios of the tests are given in Table 4.22, but major cross terms in the damping matrix give inconsistent results. The N4SID method has proved to give good and consistent results for small amplitudes, but here it clearly produces low accuracy – although the inconsistency may not stem from the identification alone. It is possible that small differences between excitations in each tests (excitations are, after

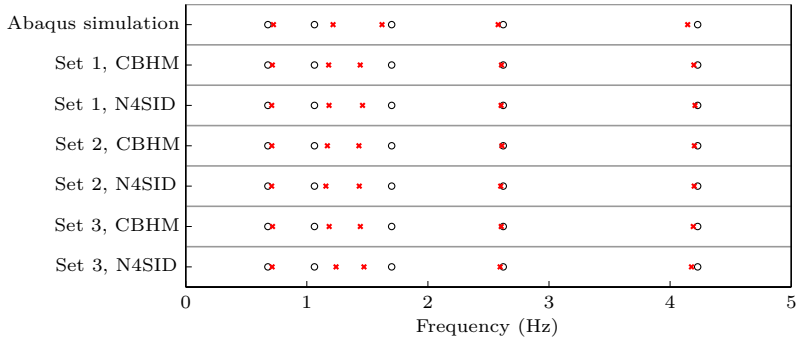

(a) Maximum amplitude (≈ 0.450 m)

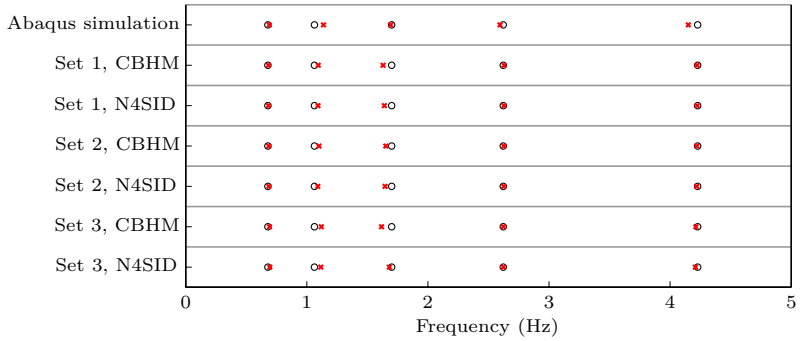

(b) Medium amplitude (≈ 0.250 m)

Figure 4.51: Natural frequencies identified from recorded displacements with large and medium amplitudes during 60 seconds of free vibration.

all, introduced by hand) are responsible for some of the variations. However, by comparing the estimates produced by the CBHM and N4SID method, it is clear that they have negligible correlation, which indicates that the identification procedure is the main source of the inconsistency.

4.6.3 Single mode effects

To gain further insight in the effect of excitation amplitudes, free vibration response of each mode was recorded separately. The mode was initially excited by it's maximum amplitude, response was recorded until it was dampened out, and identification was performed by the N4SID method on small portions of the time series. The resulting graphs of frequency and damping plotted against amplitude are given in Figure 4.52 and Figure 4.53, respectively.

When it comes to stiffness and natural frequencies, it is evident that the effect of excitation amplitudes about the resting position of the section model (no static displacements) is approximately proportional to the effect of corresponding static displacements. The

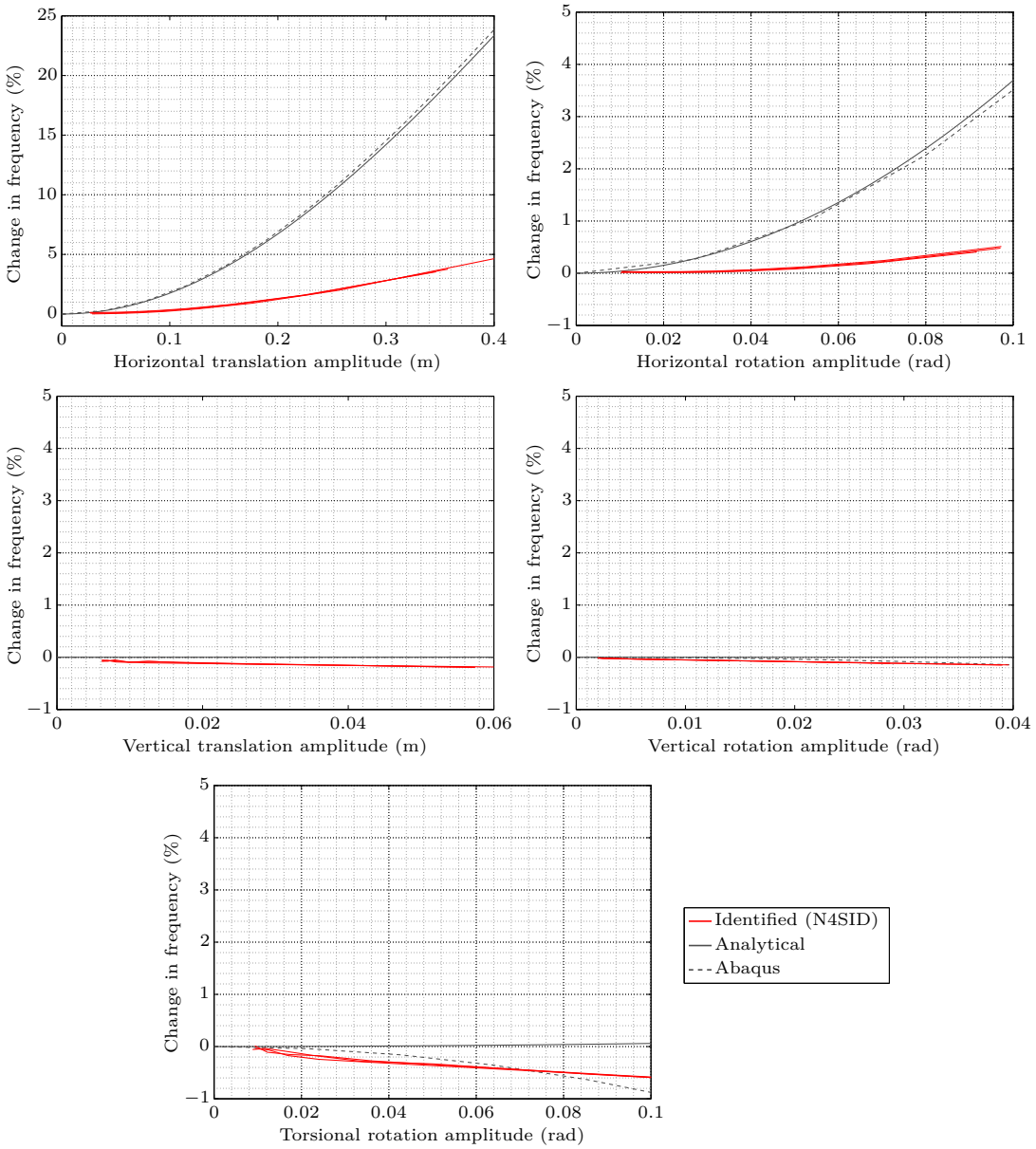

Figure 4.52: Effect of excitation amplitude on the corresponding natural frequency, identified by the N4SID method. Change in frequencies due to static displacements corresponding to the excitation amplitudes are included for comparison.

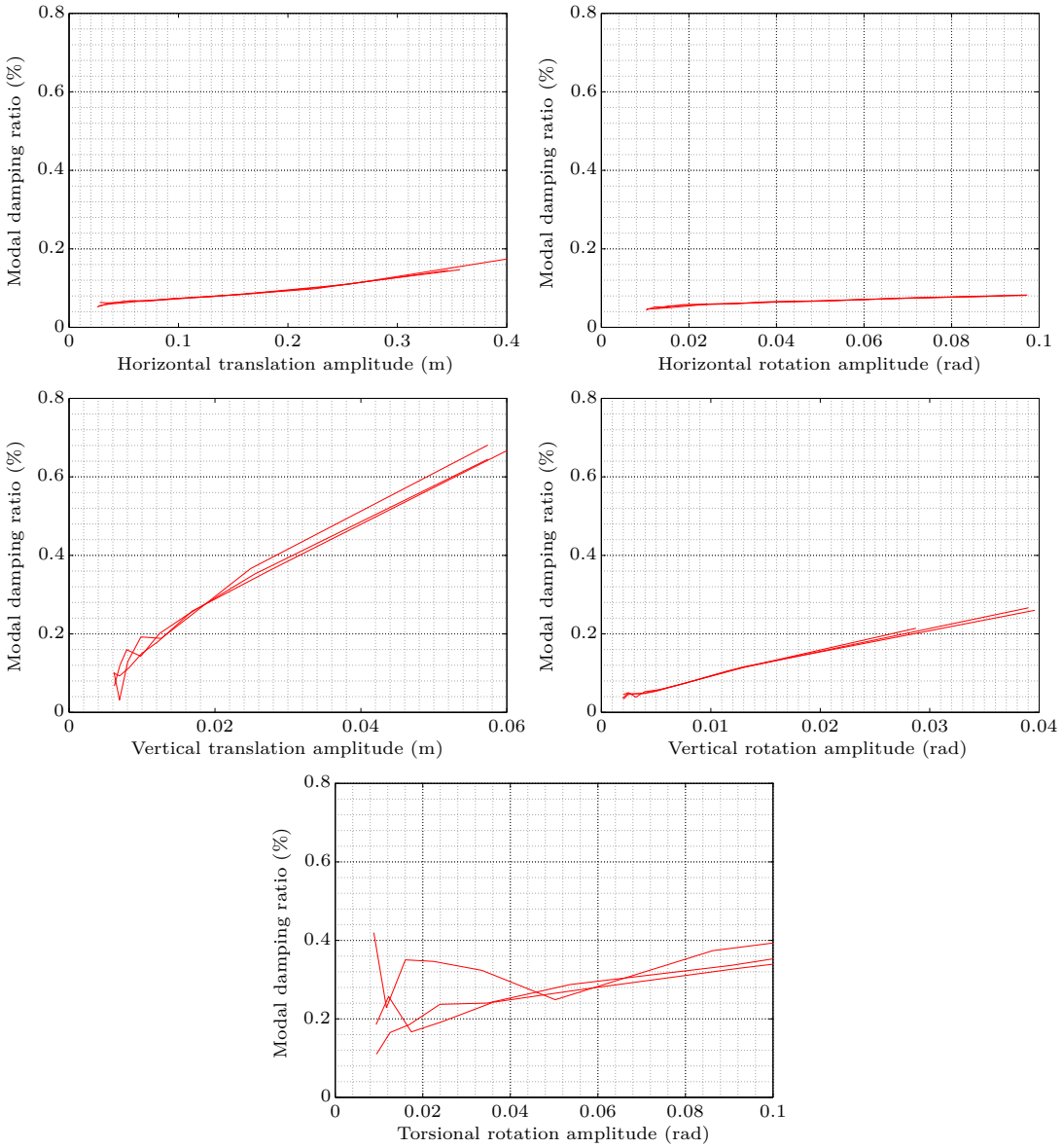

Figure 4.53: Effect of excitation amplitude on the corresponding damping ratio, identified by the N4SID method.

Mode	CBHM			N4SID		
	Set 1	Set 2	Set 3	Set 1	Set 2	Set 3
Horizontal translation	0.49	0.49	0.50	0.10	0.02	0.61
Horizontal rotation	0.82	0.73	1.62	0.31	0.11	1.46
Vertical translation	0.70	0.73	0.64	0.61	0.41	1.30
Vertical rotation	0.37	0.26	0.27	0.34	0.00	0.25
Torsional rotation	0.39	0.37	0.40	0.98	0.17	0.70

(a) Maximum amplitude (≈ 0.450 m)

Mode	CBHM			N4SID		
	Set 1	Set 2	Set 3	Set 1	Set 2	Set 3
Horizontal translation	0.50	0.50	0.50	0.10	0.71	0.07
Horizontal rotation	0.38	0.69	0.54	0.35	0.34	0.89
Vertical translation	2.32	1.53	2.40	0.21	1.19	2.77
Vertical rotation	0.20	0.21	0.22	0.06	0.22	0.39
Torsional rotation	0.37	0.39	0.40	0.37	0.35	0.92

(b) Medium amplitude (≈ 0.250 m)

Table 4.22: Modal damping ratios, given in %, obtained by identification based of recorded displacements with medium and large amplitudes during 60 seconds of free vibration.

proportionality factor, however, seems to vary between modes.

The amplitude dependency of the damping is quite clear, as larger amplitude give larger damping for all modes. This was an expected result, as aerodynamic damping depends on the velocity, and maximum velocity is proportional to maximum excitation amplitude. Since the wind velocity pressure is proportional to the velocity squared, the damping ratio becomes proportional the the velocity, and thus also to the excitation amplitude. This is reflected in the graphs, which are more or less linear.

Disturbances in the estimated damping ratios are most likely because they are identified from short time series of data, but also because of a higher degree of disturbances in response records obtained from large amplitudes.

5 Concluding remarks

5.1 Summary and conclusions

A prototype of a suspension rig allowing for horizontal, vertical and torsional motion of a section model has been developed and tested in the work described in this thesis. Furthermore, dynamic properties of the model have been obtained analytically and by two different methods of system identification, which have been compared to each other.

5.1.1 Experimental setup

The experimental setup proved to be simple and inexpensive to build, which is a major advantage over the complicated three-degree-of-freedom setup presented in the introduction. However, several drawbacks of an experimental setup based on suspension wires was revealed.

First, the suspension setup inherently introduces non-linear changes in stiffness when the section model is displaced from it's resting position. Consequently, to minimise this effect, the rig has to be as high as possible – which may lead to practical issues in a wind tunnel. Second, geometric stiffness due to tension in vertical suspensions constitutes a major part of stiffness related to horizontal motion. This effectively sets a lower bound on horizontal stiffness, which in turn sets an upper bound on the frequency ratios involving the horizontal mode. This bound may be altered by increasing vertical stiffness, although at the cost of increased natural frequencies – which in turn decreases the upper limits of reduced velocities in a wind tunnel. Finally, three uninteresting rigid body modes are inherent in the section model; one translational that was not observable in the recorded response, and hence did not pose a problem, and two rotational that can not be restrained during wind tunnel tests. It was found that they do not affect the identification of dynamic properties, but it is unknown if they affect the aeroelastic behaviour of the section model.

5.1.2 System identification

The dynamic properties of the prototype was determined by system identification based on free vibration response in still air. Determination of structural matrices requires that the modal mass matrix of the system is known. Natural frequencies matched the analytically derived frequencies closely, which indicates that the mass matrix was correct. The stiffness matrix was also identified with high accuracy, although minor cross terms was present. Identification of modal damping ratios and damping matrix, however, depended on several factors – the most important being choice of identification method. The N4SID method turned out to be sensitive to sampling rate of input data, but produced reliable and consistent damping estimates with relatively small cross terms in the damping matrix, even for short displacement records. The optimal sampling rate of the response signal proved to be twice the highest natural frequency, which is the theoretically ideal value. In contrast, the CBHM method required very long time series to produce decent damping estimates. It can be concluded that the N4SID method is much better suited for determination of dynamic properties based on free vibration response in still air than the CBHM method, and it would probably be the best choice for wind tunnel experiments.

5.1.3 Non-linear effects

A consequence of allowing horizontal motion of the section model, is that average wind velocity pressure acting on it during wind tunnel tests give rise to static displacements, which in turn alters the stiffness of the system. A correction procedure has been proposed, where the change of the analytical stiffness matrix due to the static displacements is subtracted from the identified stiffness matrix. It was tested by applying it to a stiffness matrix identified from simulated response to a turbulent wind field, and it improved the identification significantly. Minor stiffness effects of excitation amplitudes was observed, but significant effects only occurred for extreme horizontal amplitudes that would never take place in wind tunnel tests. Aerodynamic damping effects due to large amplitudes were also observed, but they would be present in any type of section model setups.

5.2 Suggestions for further work

Even though several drawbacks and limitations have been mentioned above, the proposed experimental setup seems promising for further research and development.

In this thesis, focus has been on dynamic properties in still air. Further work on the concept should involve testing in a wind tunnel, to investigate both accuracy and effect of the horizontal degree of freedom on identified aerodynamic derivatives. Several modifications of the setup are proposed:

- To maintain frequency ratios of the full scale model, vertical stiffness should be increased, as it was chosen too low in the present setup. This may be important when investigating coupling between modes.
- To decrease the lower bound on horizontal stiffness, horizontal springs may be removed, and horizontal motion may instead be recorded by e.g. lasers or position transducers. If position transducers are used, it should be investigated if they affect the stiffness and/or damping of the system.
- To allow mass and moment of inertia to be configured by extra weights, a new, lighter section model should be built. The current section model is too heavy and provides no flexibility regarding mass configuration.

In addition, effects of static displacements and excitation amplitudes, both due to structural and aeroelastic causes, should be (further) investigated.

References

[1] Abaqus/CAE, *version 6.10-2*. Dassault Systèmes, 2010, software.

[2] M. Aoki, *State space modelling of time series*, ser. Universitext. Springer Verlag, 1987.

[3] V. Boonyapinyo and T. Janesupasaeree, "Data-driven stochastic subspace identification of flutter derivatives of bridge decks," *Journal of Wind Engineering and Industrial Aerodynamics*, vol. 98, no. 12, pp. 784–799, 2010.

[4] R. Brincker and P. Andersen, "Understanding stochastic subspace identification," in *Proceedings of The 24th International Modal Analysis Conference (IMAC)*, 2006.

[5] E. Buckingham, "On physically similar systems; illustrations of the use of dimensional equations," *Physical Review*, vol. 4, pp. 345–376, 1914.

[6] L. Caracoglia, P. P. Sarkar, F. L. Haan, H. Sato, and J. Murakoshi, "Comparative and sensitivity study of flutter derivatives of selected bridge deck sections, part 2: Implications on the aerodynamic stability of long-span bridges," *Engineering Structures*, vol. 31, no. 9, pp. 2194–2202, 2009.

[7] J. Cermak and N. Isyumov, *Manual of Practice No. 67: Wind Tunnel Studies of Buildings and Structures*, ser. ASCE Manuals and Reports on Engineering Practice. American Society of Civil Engineers, 1998.

[8] C.-T. Chen, *Linear system theory and design*, 3rd ed. Oxford University Press, 2009.

[9] A. Chiuso and G. Picci, "Some algorithmic aspects of subspace identification with inputs," *International Journal of Applied Mathematics and Computer Science*, vol. 11, no. 1, pp. 55–75, 2001.

[10] A. G. Chowdhury and P. P. Sarkar, "A new technique for identification of eighteen flutter derivatives using a three-degree-of-freedom section model," *Engineering Structures*, vol. 25, no. 14, pp. 1763–1772, 2003.

[11] W. Gawronski and H. G. Natke, "Realizations of the transfer-function matrix," *International Journal of Systems Science*, vol. 18, no. 2, pp. 229–236, 1987.

[12] Y. Ge and H. Tanaka, "Aerodynamic flutter analysis of cable-supported bridges by multi-mode and full-mode approaches," *Journal of Wind Engineering and Industrial Aerodynamics*, vol. 86, no. 2–3, pp. 123–153, 2000.

[13] M. Gu and X.-R. Qin, "Direct identification of flutter derivatives and aerodynamic admittances of bridge decks," *Engineering Structures*, vol. 26, no. 14, pp. 2161–2172, 2004.

[14] R. Henriksen, "Realization of linear systems," Lecture notes, Division of Engineering Cybernetics, The Norwegian Institute of Technology, Trondheim, 1990, report no. 90-01-W.

[15] E. Hjorth-Hansen, "Section model tests," in *Aerodynamics of Large Bridges: proceedings of the first International Symposium on Aerodynamics of Large Bridges, Copenhagen, Denmark*, A. Larsen, Ed. A.A. Balkema, 1992, pp. 95–112.

[16] B. L. Ho and R. E. Kalman, "Effective construction of linear state-variable models from input/output functions," *Regelungstechnik*, vol. 14, no. 12, pp. 545–548, 1966.

[17] C. Hoen, "System identification of structures excited by stochastic load processes," Ph.D. dissertation, The Norwegian Institute of Technology, Trondheim, 1991, NTH 1991:37.

[18] P. Horowitz and W. Hill, *The art of electronics*, 2nd ed. Cambridge University Press, 1989.

[19] O. Øiseth and R. Sigbjörnsson, "An alternative analytical approach to prediction of flutter stability limits of cable supported bridges," *Journal of Sound and Vibration*, vol. 330, no. 12, pp. 2784–2800, 2011.

[20] J. B. Jakobsen, "Fluctuating wind load and response of a line-like engineering structure with emphasis on motion-induced wind forces," Ph.D. dissertation, The Norwegian Institute of Technology, Trondheim, 1995, NTH 1995:62.

[21] J. B. Jakobsen and E. Hjorth-Hansen, "Determination of the aerodynamic derivatives by a system identification method," *Journal of Wind Engineering and Industrial Aerodynamics*, vol. 57, no. 2–3, pp. 295–305, 1995.

[22] N. P. Jones, L. Singh, R. H. Scanlan, and O. Lorendeaux, "A force balance for measurement of 3-D aeroelastic parameters," *Structures Congress - Proceedings*, vol. 2, pp. 1639–1642, 1995.

[23] H. Katsuchi, N. P. Jones, and R. H. Scanlan, "Multimode coupled flutter and buffeting analysis of the Akashi-Kaikyo bridge," *Journal of Structural Engineering*, vol. 125, no. 1, pp. 60–70, 1999.

[24] E. Kreyszig, *Advanced Engineering Mathematics*, 9th ed. John Wiley & Sons, Inc., 2006.

[25] W. E. Larimore, "System identification, reduced order filtering and modeling via canonical variate analysis," in *Proceedings of the American Control Conference*, vol. 2, 1983, pp. 445–451.

[26] W. E. Larimore, "Canonical variate analysis for system identification, filtering, and adaptive control," in *Proceedings of the 29th IEEE Conference on Decision and Control, Honolulu, Hawaii*, vol. 1, 1990, pp. 635–639.

[27] L. Ljung, *System identification: theory for the user*, 2$^{\text{nd}}$ ed. Prentice Hall, 1999.

[28] L. Ljung, *MATLAB®R2012a: System Identification Toolbox^{TM}: user's guide*, The MathWorks, Inc., 2012.

[29] L. Ljung and T. Glad, *Modeling of dynamic systems*. Prentice Hall, 1994.

[30] MATLAB®, *version 7.14.0.739 (R2012a)*. The MathWorks Inc., 2012, software.

[31] MATLAB®: Signal Processing Toolbox$^{\text{TM}}$, *version 6.17 (R2012a)*. The MathWorks Inc., 2012, software.

[32] MATLAB®: System Identification Toolbox$^{\text{TM}}$, *version 8.0 (R2012a)*. The MathWorks Inc., 2012, software.

[33] S. S. Mishra, K. Kumar, and P. Krishna, "Relevance of eighteen flutter derivatives in wind response of a long-span cable-stayed bridge," *Journal of Structural Engineering*, vol. 134, no. 5, pp. 769–781, 2008.

[34] B. C. Moore, "Principal component analysis in linear systems: controllability, observability and model reduction," *IEEE Transactions on Automatic Control*, vol. AC-26, no. 1, pp. 17–32, 1981.

[35] A. V. Oppenheim and R. W. Schafer, *Discrete-time signal processing*, 3$^{\text{rd}}$ ed. Pearson, 2010.

[36] P. P. Sarkar, L. Caracoglia, F. L. Haan, H. Sato, and J. Murakoshi, "Comparative and sensitivity study of flutter derivatives of selected bridge deck sections, part 1: Analysis of inter-laboratory experimental data," *Engineering Structures*, vol. 31, no. 1, pp. 158–169, 2009.

[37] P. P. Sarkar, A. G. Chowdhury, and T. B. Gardner, "A novel elastic suspension system for wind tunnel section model studies," *Journal of Wind Engineering and Industrial Aerodynamics*, vol. 92, no. 1, pp. 23–40, 2004.

[38] P. P. Sarkar, N. P. Jones, and R. H. Scanlan, "System identification for estimation of flutter derivatives," *Journal of Wind Engineering and Industrial Aerodynamics*, vol. 41-44, pp. 1243–1254, 1992.

[39] R. H. Scanlan, "Amplitude and turbulence effects on bridge flutter derivatives," *Journal of Structural Engineering, ASCE*, vol. 123, no. 2, pp. 232–236, 1997.

[40] R. H. Scanlan and N. P. Jones, "Aeroelastic analysis of cable-stayed bridges," *Journal of Structural Engineering, ASCE*, vol. 116, no. 2, pp. 279–297, 1990.

[41] R. H. Scanlan and J. J. Tomko, "Airfoil and bridge deck flutter derivatives," *Journal of the Engineering Mechanics Division, ASCE*, vol. 97, no. EM6, pp. 1717–1737, 1971.

[42] L. Singh, N. P. Jones, R. H. Scanlan, and O. Lorendeaux, "Identification of lateral flutter derivatives of bridge decks," *Journal of Wind Engineering and Industrial Aerodynamics*, vol. 60, pp. 81–89, 1996.

[43] J. O. Smith, *Introduction to Digital Filters with Audio Applications* . http://ccrma.stanford.edu/~jos/filters/, accessed 17th May 2012, online book.

[44] J. O. Smith, *Mathematics of the Discrete Fourier Transform (DFT)* . http://ccrma.stanford.edu/~jos/mdft/, accessed 6th June 2012, online book.

[45] S. W. Smith, *The scientist and engineer's guide to digital signal processing.* California Technical Publishing, 1997.

[46] J. Staar, "A study of MBH-type realization algorithms," *Automatica*, vol. 17, no. 3, pp. 523–533, 1981.

[47] Statens vegvesen, "Hardangerbrua: Gr.lagsdata rev. 06.03.2007 (cy.path down-st), analysed by ALVSAT," March 2007, unpublished.

[48] Statens vegvesen, "Hardangerbrua: Beregninger, kapittel 1: Grunnlag," November 2008, project 12-2950, revision 5.

[49] E. Strømmen, *Theory of bridge aerodynamics*, 2nd ed. Springer, 2010.

[50] Svend Ole Hansen ApS, "The Hardanger Bridge: Static and dynamic wind tunnel tests with a section model," December 2006, revision 1.

[51] H. Tanaka, "Similitude and modelling in wind tunnel testing of bridges," *Journal of Wind Engineering and Industrial Aerodynamics*, vol. 33, no. 1-2, pp. 283–300, 1990.

[52] P. Van Overschee and B. De Moor, "Subspace algorithms for the stochastic identification problem," *Automatica*, vol. 29, no. 3, pp. 649–660, 1993.

[53] P. Van Overschee and B. De Moor, "N4SID: Subspace algorithms for the identification of combined deterministic-stochastic systems," *Automatica*, vol. 30, no. 1, pp. 75–93, 1994.

[54] P. Van Overschee and B. De Moor, *Subspace identification for linear systems: theory, implementation, applications.* Kluwer Academic Pulishers, 1996.

[55] M. Verhaegen, "A novel non-iterative MIMO state space model identification technique," in *Proceedings of the 9th IFAC/IFORS Symposium on Identification and System Parameter Estimation, Budapest, Hungary*, 1991, p. 1453–1458.

[56] M. Verhaegen and P. Dewilde, "Subspace model identification part 1: The output-error state space model identification class of algorithms," *International Journal of Control*, vol. 56, no. 5, pp. 1187–1210, 1992.

[57] J.-J. Wu, "Prediction of the dynamic characteristics of an elastically supported full-size flat plate from those of its complete-similitude scale model," *Computers & Structures*, vol. 84, no. 3–4, pp. 102–114, 2006.

Appendix A: Stiffness matrix

The stiffness matrix of the section model is rather complex, and depends on both initial spring forces (due to self weight and pretensioning), static (mean) displacements and dynamic excitation amplitudes. An idealised mathematical model will be obtained by first considering each of the two basic suspension systems (one at each end of the section model) individually, and establishing their respective stiffness matrices. These matrices will then be combined and transformed into the stiffness matrix of the full system.

Inertia and damping forces are assumed to be independent of the stiffness, and are not considered in the equilibrium calculations.

A.1 Stiffness matrix of the basic suspension system

Figure A.54 shows the basic suspension system, which essentially comprises a rotation arm, six springs and six wires. It is considered two-dimensional, which is an adequate approximation, such that static ($\bar{r}$) and dynamic (r) displacements are defined in the xz-plane. The local degrees of freedom, r_x, r_z and r_θ, correspond to linear combinations of the global degrees of freedom in the full system. This will be further discussed in section A.2. It is important to note that the brackets used to mount the wires onto the rotation arms give a small offset e between the centre line of the rotation arm and the actual mounting point.

A direct approach will be taken to establish the matrix for an infinitesimal excitation amplitude. In turn, each degree of freedom is given an infinitesimal displacement while the others are restrained, and the equilibrium expression will then indirectly give the stiffness relations sought for. Finally, it is a matter of reorganizing these expressions to obtain the stiffness matrix.

It is in general assumed infinitely stiff wires and perfectly bilinear springs, i.e.

$$F_S = F_0 + k\mathrm{d}l$$

where F_s is the spring force, F_0 is a constant force due to internal stresses in the spring, k is the stiffness and $\mathrm{d}l$ is the deflection. To incorporate the elasticity of the wires,

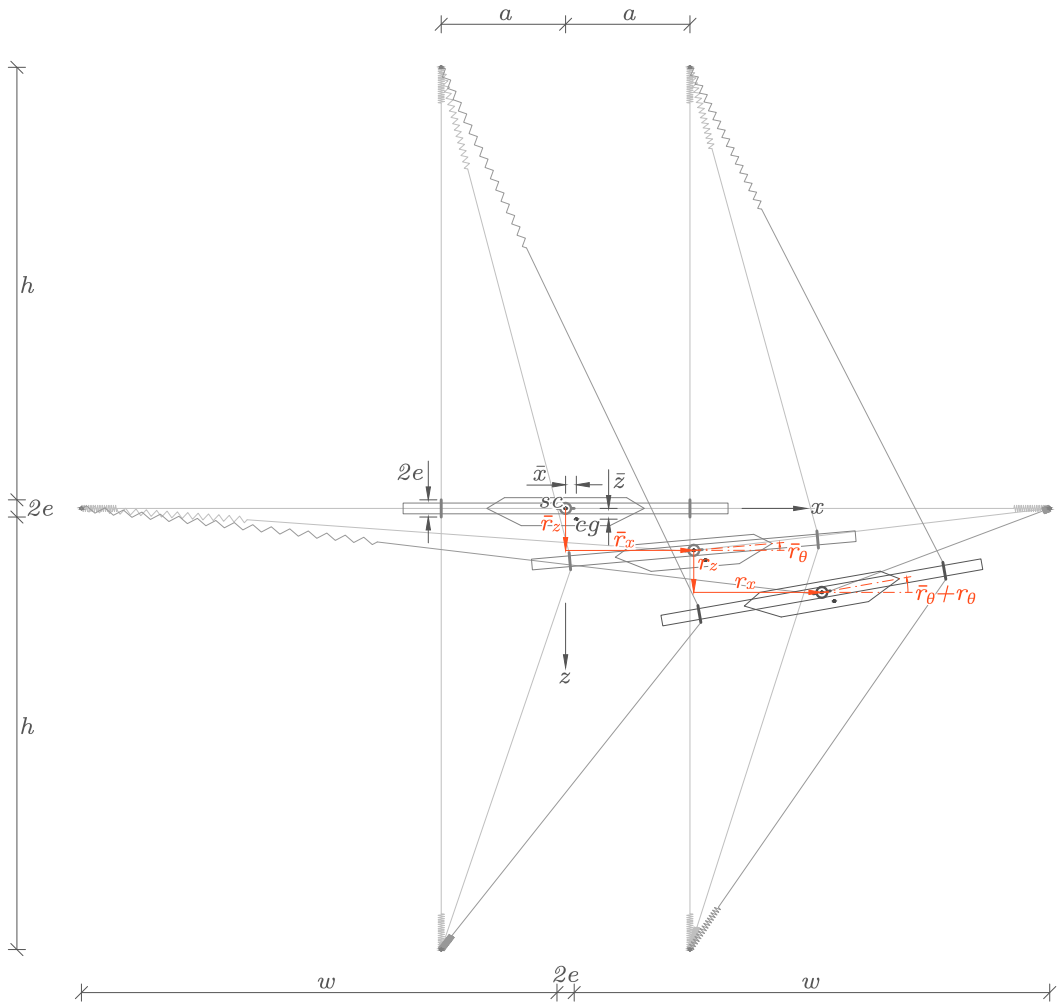

Figure A.54: Definition of geometry and displacements of the basic suspension system.

an effective spring stiffness which accommodates the wire stiffness should be calculated. It is also assumed that $\bar{r}_\theta$ is small enough to justify the approximation of $\cos(\bar{r}_\theta) \approx 1$ and $\sin(\bar{r}_\theta) \approx \bar{r}_\theta$.

A.1.1 Effect of infinitesimal displacements

The reaction to a displacement of the end of a suspension comprises two parts. The first part is a force induced by spring elongation, while the second part is a force induced by tension in the suspension, referred to as *geometric stiffness*. Geometric stiffness constitutes a major part of the horizontal stiffness of the section model.

Figure A.55 shows the loading situation for one of the vertical suspensions in the setup,

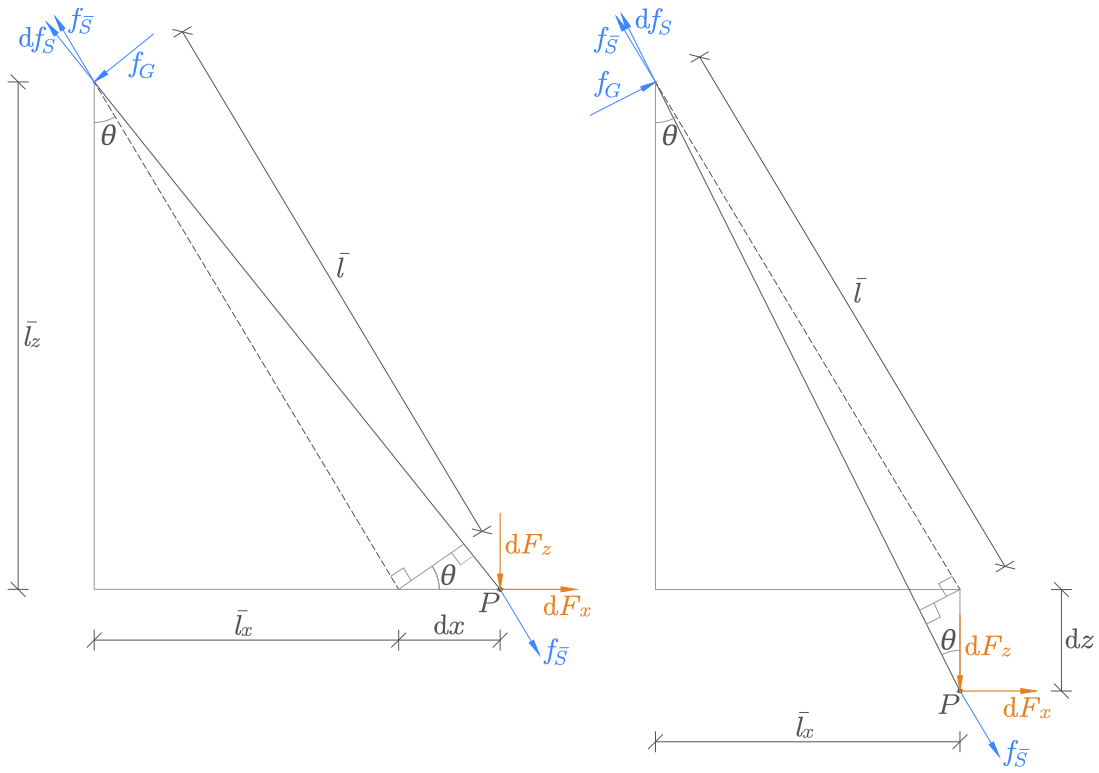

(a) Horizontal displacement

(b) Vertical displacement

Figure A.55: Effect of infinitesimal displacements (exaggerated).

but is also valid for horizontal suspensions. The infinitesimal displacements are exaggerated, but it is assumed that they are so small that the deformed suspension is approximately parallel to the undeformed suspension. It is loaded with a tensile force $f_{\bar{S}}$, and infinitesimal displacements $\mathrm{d}x$ and $\mathrm{d}z$ has been introduced by the forces $\mathrm{d}F_x$ and $\mathrm{d}F_z$. This has given rise to an increase of the tensile force, $\mathrm{d}f_S$, and a force due to geometric stiffness, f_G. Both forces are directed opposite to the displacement, i.e. the x-components are directed opposite to $\mathrm{d}x$ in Figure A.55a, and the z-components opposite to $\mathrm{d}z$ in Figure A.55b.

The static tensile force $f_{\bar{S}}$ is given by

$$f_{\bar{S}} = f_{S_0} + k\left(\bar{l} - \bar{l}_z\right) \tag{A.86}$$

where f_{S_0} is an initial force due to weight and pretensioning of springs. In Figure A.55a, the assumption of bilinear springs gives

$$\mathrm{d}f_S = k\mathrm{d}l = k\frac{\bar{l}_x}{\bar{l}}\mathrm{d}x \tag{A.87}$$

where k is the spring stiffness, and moment equilibrium about P gives

$$f_G = f_{\bar{S}} \frac{\bar{l}_z}{\bar{l}^2 + \bar{l}_x \mathrm{d}x} \mathrm{d}x \approx \frac{f_{\bar{S}}}{\bar{l}} \frac{\bar{l}_z}{\bar{l}} \mathrm{d}x \tag{A.88}$$

These forces may be decomposed into x and z-components, given by

$$f_{S,x} = f_{\bar{S}} \frac{\bar{l}_x}{\bar{l}} + k \frac{\bar{l}_x^2}{\bar{l}^2} \mathrm{d}x \quad \text{and} \quad f_{S,z} = f_{\bar{S}} \frac{\bar{l}_z}{\bar{l}} + k \frac{\bar{l}_x \bar{l}_z}{\bar{l}^2} \mathrm{d}x \tag{A.89}$$

$$f_{G,x} = \frac{f_{\bar{S}}}{\bar{l}} \frac{\bar{l}_z^2}{\bar{l}^2} \mathrm{d}x \quad \text{and} \quad f_{G,z} = \frac{f_{\bar{S}}}{\bar{l}} \frac{\bar{l}_x \bar{l}_z}{\bar{l}^2} \mathrm{d}x \tag{A.90}$$

Similarly, the force components of the situation in Figure A.55b is given by

$$f_{S,x} = f_{\bar{S}} \frac{\bar{l}_x}{\bar{l}} + k \frac{\bar{l}_x \bar{l}_z}{\bar{l}^2} \mathrm{d}x \quad \text{and} \quad f_{S,z} = f_{\bar{S}} \frac{\bar{l}_z}{\bar{l}} + k \frac{\bar{l}_z^2}{\bar{l}^2} \mathrm{d}x \tag{A.91}$$

$$f_{G,x} = \frac{f_{\bar{S}}}{\bar{l}} \frac{\bar{l}_x \bar{l}_z}{\bar{l}^2} \mathrm{d}z \quad \text{and} \quad f_{G,z} = \frac{f_{\bar{S}}}{\bar{l}} \frac{\bar{l}_x^2}{\bar{l}^2} \mathrm{d}z \tag{A.92}$$

A.1.2 Infinitesimal horizontal displacement

In Figure A.56, spring stiffness, displacements and forces acting on the rotation arm are defined. Forces required to maintain the displacement are denoted R, spring forces f_S and forces due to geometric stiffness are denoted f_G. The abbreviations h, uv and lv indicate the main direction of a suspension, and stands for *horizontal*, *upper vertical* and *lower vertical*, respectively. The subscripts 1 and 2 indicates the side, i.e. left or right. Since the full system comprises two instances of this subsystem, the weight M_g should be taken as half the total weight.

Equilibrium is now expressed by

$$\mathbf{R}_x = \begin{bmatrix} R_{x,x} \\ R_{z,x} \\ R_{\theta,x} \end{bmatrix} = \mathbf{R}_{\mathbf{S},x} + \mathbf{R}_{\mathbf{G},x} + \mathbf{R}_{\mathbf{M},x} \tag{A.93}$$

where the subscript x indicates forces *induced by a horizontal displacement*. To enhance readability, the forces has been divided into vectors based on their origin. These vectors are established based on Figure A.56, and are given by

$$\mathbf{R}_{\mathbf{S},x} = \begin{bmatrix} f_{S,h_1,x} - f_{S,h_2,x} + f_{S,uv_1,x} + f_{S,uv_2,x} + f_{S,lv_1,x} + f_{S,lv_2,x} \\ f_{S,h_1,z} + f_{S,h_2,z} + f_{S,uv_1,z} + f_{S,uv_2,z} - f_{S,lv_1,z} - f_{S,lv_2,z} \\ \left(f_{S,h_1,x} + f_{S,h_2,x}\right) \bar{r}_\theta e + \left(f_{S,h_1,z} - f_{S,h_2,z}\right) e \\ + \left(f_{S,lv_1,x} - f_{S,uv_2,x}\right) \left(\bar{r}_\theta a + e\right) + \left(f_{S,uv_1,x} - f_{S,lv_2,x}\right) \left(\bar{r}_\theta a - e\right) \\ + \left(f_{S,uv_1,z} + f_{S,lv_2,z}\right) \left(a + \bar{r}_\theta e\right) - \left(f_{S,uv_2,z} + f_{S,lv_1,z}\right) \left(a - \bar{r}_\theta e\right) \end{bmatrix} \tag{A.94}$$

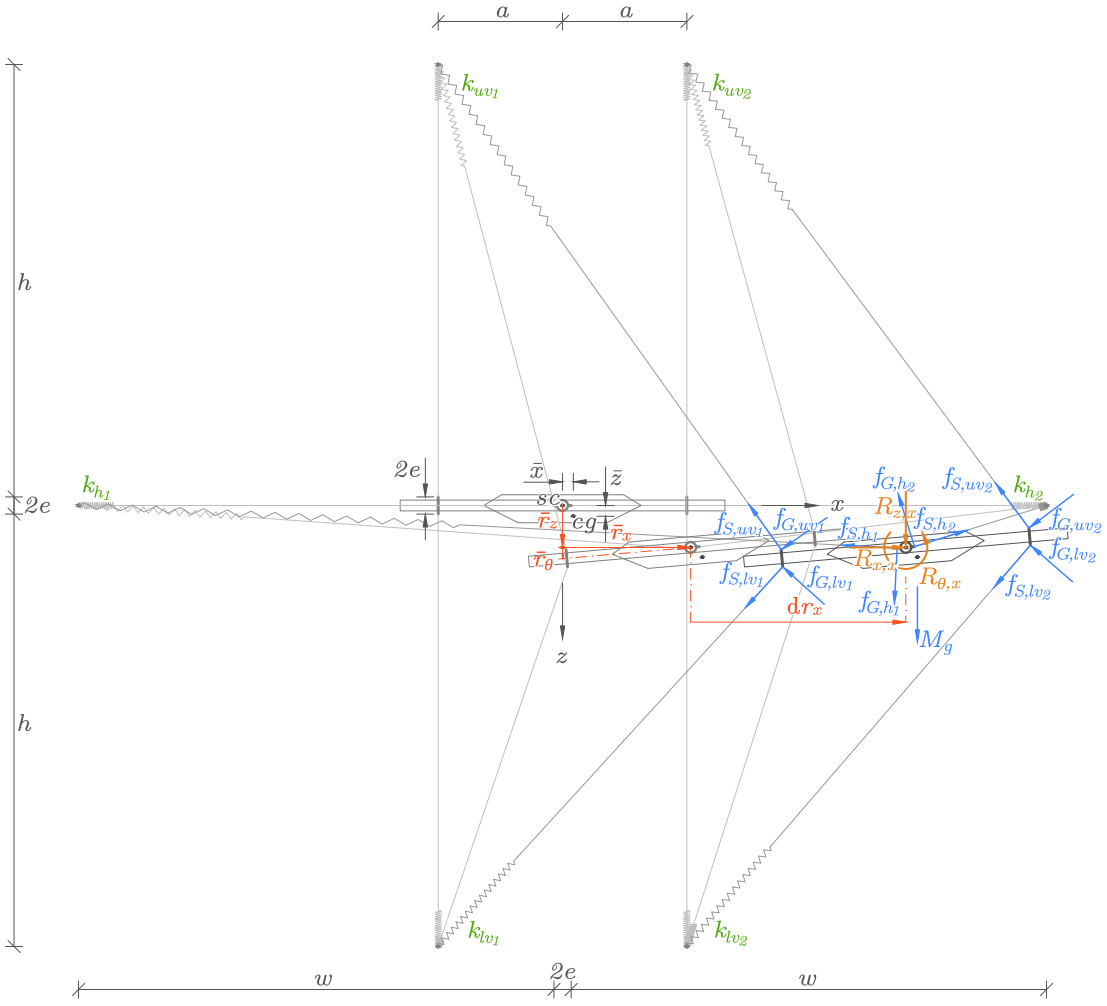

Figure A.56: Infinitesimal horizontal displacement (exaggerated).

$$\mathbf{R}_{\mathbf{G},x} = \begin{bmatrix} f_{G,h_1,x} + f_{G,h_2,x} + f_{G,uv_1,x} + f_{G,uv_2,x} + f_{G,lv_1,x} + f_{G,lv_2,x} \\ -f_{G,h_1,z} + f_{G,h_2,z} - f_{G,uv_1,z} - f_{G,uv_2,z} + f_{G,lv_1,z} + f_{G,lv_2,z} \\ \left(f_{G,h_1,x} - f_{G,h_2,x}\right)\bar{r}_\theta e - \left(f_{G,h_1,z} + f_{G,h_2,z}\right)e \\ + \left(f_{G,lv_1,x} - f_{G,uv_2,x}\right)\left(\bar{r}_\theta a + e\right) + \left(f_{G,uv_1,x} - f_{G,lv_2,x}\right)\left(\bar{r}_\theta a - e\right) \\ - \left(f_{S,uv_1,z} + f_{S,lv_2,z}\right)\left(a + \bar{r}_\theta e\right) + \left(f_{S,uv_2,z} + f_{S,lv_1,z}\right)\left(a - \bar{r}_\theta e\right) \end{bmatrix} \tag{A.95}$$

$$\mathbf{R}_{\mathbf{M},x} = \begin{bmatrix} 0 \\ -M_g \\ \left(\bar{x} + \bar{r}_\theta \bar{z}\right) M_g \end{bmatrix} \tag{A.96}$$

To facilitate calculations, these expressions has to be systematised.

To obtain compact vector expressions, it is necessary to introduce element-wise operators. The following notation will be adopted:

- $\bullet$ denotes the *dot product* of two vectors.
- $\odot$ denotes element-wise multiplication of two vectors, i.e. the *Hadamard product*.
- $\oslash$ denotes element-wise division of two vectors.
- $\textcircled{n}$ denotes element-wise power of n of two vectors.

To accommodate for different directions of the forces, *sign vectors* are introduced:

$$\mathbf{sgn_{S,x}} = \begin{bmatrix} 1 & -1 & 1 & 1 & 1 & 1 \end{bmatrix}^{\mathrm{T}} \tag{A.97a}$$

$$\mathbf{sgn_{S,z}} = \begin{bmatrix} 1 & 1 & 1 & 1 & -1 & -1 \end{bmatrix}^{\mathrm{T}} \tag{A.97b}$$

$$\mathbf{sgn_{G,xz}} = \begin{bmatrix} -1 & 1 & -1 & -1 & 1 & 1 \end{bmatrix}^{\mathrm{T}} \tag{A.97c}$$

$$\mathbf{sgn_{sum}} = \begin{bmatrix} 1 & 1 & 1 & 1 & 1 & 1 \end{bmatrix}^{\mathrm{T}} \tag{A.97d}$$

Finally, to couple forces and moments, the following *moment arm vectors* are introduced:

$$\mathbf{a_x} = \begin{bmatrix} \bar{r}_\theta e \\ \bar{r}_\theta e \\ \bar{r}_\theta a - e \\ -\bar{r}_\theta a - e \\ \bar{r}_\theta a + e \\ -\bar{r}_\theta a + e \end{bmatrix} \quad \text{and} \quad \mathbf{a_z} = \begin{bmatrix} e \\ -e \\ a + \bar{r}_\theta e \\ -a + \bar{r}_\theta e \\ -a + \bar{r}_\theta e \\ a + \bar{r}_\theta e \end{bmatrix} \tag{A.98}$$

Suspension lengths

In the following, the combined length of springs and wire in each suspension is referred to as *suspension length*. The initial suspension lengths are given by

$$\bar{\mathbf{l}}_\mathbf{0} = \begin{bmatrix} w & w & h & h & h & h \end{bmatrix}^{\mathrm{T}} \tag{A.99}$$

Figure A.56 gives the x and z-components of the suspension lengths after static displacements:

$$\bar{\mathbf{l}}_x = \begin{bmatrix} \bar{l}_{h_1,x} \\ \bar{l}_{h_2,x} \\ \bar{l}_{uv_1,x} \\ \bar{l}_{uv_2,x} \\ \bar{l}_{lv_1,x} \\ \bar{l}_{lv_2,x} \end{bmatrix} = \begin{bmatrix} |w + \bar{r}_x| \\ |w - \bar{r}_x| \\ |\bar{r}_x - \bar{r}_\theta e| \\ |\bar{r}_x - \bar{r}_\theta e| \\ |\bar{r}_x + \bar{r}_\theta e| \\ |\bar{r}_x + \bar{r}_\theta e| \end{bmatrix} \quad \text{and} \quad \bar{\mathbf{l}}_z = \begin{bmatrix} \bar{l}_{h_1,z} \\ \bar{l}_{h_2,z} \\ \bar{l}_{uv_1,z} \\ \bar{l}_{uv_2,z} \\ \bar{l}_{lv_1,z} \\ \bar{l}_{lv_2,z} \end{bmatrix} = \begin{bmatrix} |\bar{r}_z + \bar{r}_\theta e| \\ |\bar{r}_z - \bar{r}_\theta e| \\ |h + \bar{r}_z + \bar{r}_\theta a| \\ |h + \bar{r}_z - \bar{r}_\theta a| \\ |h - \bar{r}_z - \bar{r}_\theta a| \\ |h - \bar{r}_z + \bar{r}_\theta a| \end{bmatrix} \tag{A.100}$$

The full lengths are then given by

$$\bar{\mathbf{l}} = \begin{bmatrix} \bar{l}_{h_1} \\ \bar{l}_{h_2} \\ \bar{l}_{uv_1} \\ \bar{l}_{uv_2} \\ \bar{l}_{lv_1} \\ \bar{l}_{lv_2} \end{bmatrix} = \begin{bmatrix} \sqrt{\bar{l}_{h_1,x}^2 + \bar{l}_{h_1,z}^2} \\ \sqrt{\bar{l}_{h_2,x}^2 + \bar{l}_{h_2,z}^2} \\ \sqrt{\bar{l}_{uv_1,x}^2 + \bar{l}_{uv_1,z}^2} \\ \sqrt{\bar{l}_{uv_2,x}^2 + \bar{l}_{uv_2,z}^2} \\ \sqrt{\bar{l}_{lv_1,x}^2 + \bar{l}_{lv_1,z}^2} \\ \sqrt{\bar{l}_{lv_2,x}^2 + \bar{l}_{lv_2,z}^2} \end{bmatrix} = \begin{bmatrix} \sqrt{|w + \bar{r}_x|^2 + |\bar{r}_z + \bar{r}_\theta e|^2} \\ \sqrt{|w - \bar{r}_x|^2 + |\bar{r}_z - \bar{r}_\theta e|^2} \\ \sqrt{|\bar{r}_x - \bar{r}_\theta e|^2 + |h + \bar{r}_z + \bar{r}_\theta a|^2} \\ \sqrt{|\bar{r}_x - \bar{r}_\theta e|^2 + |h + \bar{r}_z - \bar{r}_\theta a|^2} \\ \sqrt{|\bar{r}_x + \bar{r}_\theta e|^2 + |h - \bar{r}_z - \bar{r}_\theta a|^2} \\ \sqrt{|\bar{r}_x + \bar{r}_\theta e|^2 + |h - \bar{r}_z + \bar{r}_\theta a|^2} \end{bmatrix} \tag{A.101}$$

Forces acting on the rotation arm

Initial forces are the tensile forces in the suspensions when the section model is at rest in still air, i.e. forces due to self weight and pretensioning of springs. The initial forces f_{S_0,nn_i} and spring stiffness k_{nn_i} may be vectorised by

$$\mathbf{f_{S_0}} = \begin{bmatrix} f_{S_0,h_1} & f_{S_0,h_2} & f_{S_0,uv_1} & f_{S_0,uv_2} & f_{S_0,lv_1} & f_{S_0,lv_2} \end{bmatrix}^{\mathrm{T}} \tag{A.102}$$

$$\mathbf{k} = \begin{bmatrix} k_{h_1} & k_{h_2} & k_{uv_1} & k_{uv_2} & k_{lv_1} & k_{lv_2} \end{bmatrix}^{\mathrm{T}} \tag{A.103}$$

The static forces are now found by element-wise application of (A.86):

$$\mathbf{f_{\bar{S}}} = \mathbf{f_{S_0}} + \mathbf{k} \odot \left(\bar{\mathbf{l}} - \bar{\mathbf{l}}_\mathbf{0} \right) \tag{A.104}$$

and the spring forces are found from (A.89):

$$\mathbf{f_{S}}_{x,x} = \mathbf{f_{\bar{S}}} \odot \left(\bar{\mathbf{l}}_x \oslash \bar{\mathbf{l}} \right) + \mathbf{k} \odot \left(\bar{\mathbf{l}}_x^{②} \oslash \bar{\mathbf{l}}^{②} \right) \odot (\mathbf{sgn_{S,x}} \mathrm{d}r_x) \tag{A.105a}$$

$$\mathbf{f_{S}}_{z,x} = \mathbf{f_{\bar{S}}} \odot \left(\bar{\mathbf{l}}_z \oslash \bar{\mathbf{l}} \right) + \mathbf{k} \odot \left[\left(\bar{\mathbf{l}}_x \odot \bar{\mathbf{l}}_z \right) \oslash \bar{\mathbf{l}}^{②} \right] \odot (\mathbf{sgn_{S,x}} \mathrm{d}r_x) \tag{A.105b}$$

where $\mathbf{sgn_{S,x}}$ maps the displacement of the rotation arm $\mathrm{d}r_x$ to elongation or shortening of the spring. The forces due to geometric stiffness are similarly found from (A.90):

$$\mathbf{f_{G}}_{x,x} = \left(\mathbf{f_{\bar{S}}} \oslash \bar{\mathbf{l}} \right) \odot \left(\bar{\mathbf{l}}_z^{②} \oslash \bar{\mathbf{l}}^{②} \right) \mathrm{d}r_x \tag{A.106a}$$

$$\mathbf{f_{G}}_{z,x} = \left(\mathbf{f_{\bar{S}}} \oslash \bar{\mathbf{l}} \right) \odot \left[\left(\bar{\mathbf{l}}_x \odot \bar{\mathbf{l}}_z \right) \oslash \bar{\mathbf{l}}^{②} \right] \mathrm{d}r_x \tag{A.106b}$$

The reaction forces defined in equation (A.94) and (A.95) may now be expressed by

$$\mathbf{R}_{\mathbf{S},x} = \begin{bmatrix} \mathbf{f}_{\mathbf{S}x,x} \bullet \mathbf{sgn}_{\mathbf{S,x}} \\ \mathbf{f}_{\mathbf{S}z,x} \bullet \mathbf{sgn}_{\mathbf{S,z}} \\ \mathbf{f}_{\mathbf{S}x,x} \bullet \mathbf{a}_{\mathbf{x}} + \mathbf{f}_{\mathbf{S}z,x} \bullet \mathbf{a}_{\mathbf{z}} \end{bmatrix} \tag{A.107}$$

$$\mathbf{R}_{\mathbf{G},x} = \begin{bmatrix} \mathbf{f}_{\mathbf{G}x,x} \bullet \mathbf{sgn}_{\mathbf{sum}} \\ \mathbf{f}_{\mathbf{G}z,x} \bullet \mathbf{sgn}_{\mathbf{G,xz}} \\ (\mathbf{f}_{\mathbf{G}x,x} \odot \mathbf{a}_{\mathbf{x}} - \mathbf{f}_{\mathbf{G}z,x} \odot \mathbf{a}_{\mathbf{z}}) \bullet \mathbf{sgn}_{\mathbf{S,x}} \end{bmatrix} \tag{A.108}$$

Stiffness relation

Equation A.93–A.96 may be reorganised to the form

$$\begin{bmatrix} R_{x,x} \\ R_{z,x} \\ R_{\theta,x} \end{bmatrix} = \begin{bmatrix} K_{xx} \\ K_{zx} \\ K_{\theta x} \end{bmatrix} \mathrm{d}r_x + \begin{bmatrix} P_x \\ P_z \\ P_\theta \end{bmatrix} \tag{A.109}$$

where the stiffness vector K_{mx} $(m = x, z, \theta)$ constitutes the first column of the stiffness matrix of the system. The force vector P_m contains the net forces required to maintain the static displacement pattern. This relation will be used to establish the full stiffness matrix in section A.2.

A.1.3 Infinitesimal vertical displacement

The effect of an infinitesimal vertical displacement, shown in Figure A.57, is derived in the same manner as for a horizontal displacement. The reaction forces are now given by

$$\mathbf{R}_z = \begin{bmatrix} R_{x,z} \\ R_{z,z} \\ R_{\theta,z} \end{bmatrix} = \mathbf{R}_{\mathbf{S},z} + \mathbf{R}_{\mathbf{G},z} + \mathbf{R}_{\mathbf{M},z} \tag{A.110}$$

where the subscript z indicates forces *induced by a vertical displacement.* The main spring force directions are all the same as in Figure A.56; only magnitudes are different. Hence, $\mathbf{R}_{\mathbf{S},z}$ have the same structure as $\mathbf{R}_{\mathbf{S},x}$, but f_{S,nn_i} now refers to the forces in Figure A.57:

$$\mathbf{R}_{\mathbf{S},z} = \begin{bmatrix} f_{S,h_1,x} - f_{S,h_2,x} + f_{S,uv_1,x} + f_{S,uv_2,x} + f_{S,lv_1,x} + f_{S,lv_2,x} \\ f_{S,h_1,z} + f_{S,h_2,z} + f_{S,uv_1,z} + f_{S,uv_2,z} - f_{S,lv_1,z} - f_{S,lv_2,z} \\ (f_{S,h_1,x} + f_{S,h_2,x})\,\bar{r}_\theta e + (f_{S,h_1,z} - f_{S,h_2,z})\,e \\ + (f_{S,lv_1,x} - f_{S,uv_2,x})\,(\bar{r}_\theta a + e) + (f_{S,uv_1,x} - f_{S,lv_2,x})\,(\bar{r}_\theta a - e) \\ + (f_{S,uv_1,z} + f_{S,lv_2,z})\,(a + \bar{r}_\theta e) - (f_{S,uv_2,z} + f_{S,lv_1,z})\,(a - \bar{r}_\theta e) \end{bmatrix} \tag{A.111}$$

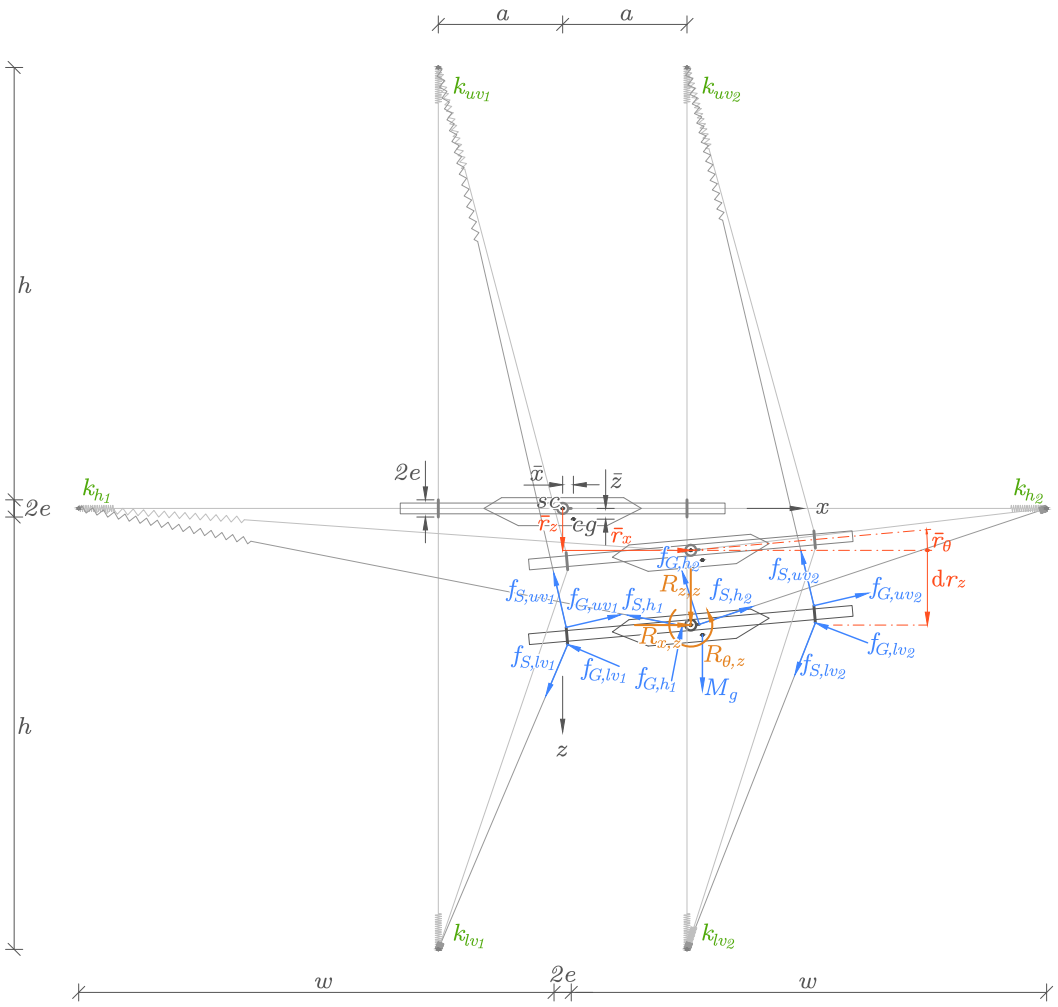

Figure A.57: Infinitesimal vertical displacement (exaggerated).

The reaction forces induced by geometric stiffness are slightly different, since some of the forces have changed direction:

$$\mathbf{R}_{\mathbf{G},z} = \begin{bmatrix} -f_{G,h_1,x} + f_{G,h_2,x} - f_{G,uv_1,x} - f_{G,uv_2,x} + f_{G,lv_1,x} + f_{G,lv_2,x} \\ f_{G,h_1,z} + f_{G,h_2,z} + f_{G,uv_1,z} + f_{G,uv_2,z} + f_{G,lv_1,z} + f_{G,lv_2,z} \\ -\left(f_{G,h_1,x} + f_{G,h_2,x}\right)\bar{r}_\theta e + \left(f_{G,h_1,z} - f_{G,h_2,z}\right)e \\ +\left(f_{G,lv_1,x} + f_{G,uv_2,x}\right)\left(\bar{r}_\theta a + e\right) - \left(f_{G,uv_1,x} + f_{G,lv_2,x}\right)\left(\bar{r}_\theta a - e\right) \\ +\left(f_{S,uv_1,z} - f_{S,lv_2,z}\right)\left(a + \bar{r}_\theta e\right) - \left(f_{S,uv_2,z} - f_{S,lv_1,z}\right)\left(a - \bar{r}_\theta e\right) \end{bmatrix} \tag{A.112}$$

$$\mathbf{R}_{\mathbf{M},z} = \begin{bmatrix} 0 \\ -M_g \\ \left(\bar{x} + \bar{r}_\theta \bar{z}\right) M_g \end{bmatrix} \tag{A.113}$$

The static forces are invariant with respect to infinitesimal displacements, and are unchanged. However, the forces acting on the rotation arm are now changed to

$$\mathbf{f_S}_{x,z} = \mathbf{f_{\bar{S}}} \odot \left(\bar{\mathbf{l}}_x \oslash \bar{\mathbf{l}}\right) + \mathbf{k} \odot \left[\left(\bar{\mathbf{l}}_x \odot \bar{\mathbf{l}}_z\right) \oslash \bar{\mathbf{l}}^{②}\right] \odot (\mathbf{sgn_{S,z}} \mathrm{d}r_z) \tag{A.114a}$$

$$\mathbf{f_S}_{z,z} = \mathbf{f_{\bar{S}}} \odot \left(\bar{\mathbf{l}}_z \oslash \bar{\mathbf{l}}\right) + \mathbf{k} \odot \left(\bar{\mathbf{l}}_z^{②} \oslash \bar{\mathbf{l}}^{②}\right) \odot (\mathbf{sgn_{S,z}} \mathrm{d}r_z) \tag{A.114b}$$

and

$$\mathbf{f_G}_{x,z} = \left(\mathbf{f_{\bar{S}}} \oslash \bar{\mathbf{l}}\right) \odot \left[\left(\bar{\mathbf{l}}_x \odot \bar{\mathbf{l}}_z\right) \oslash \bar{\mathbf{l}}^{②}\right] \mathrm{d}r_z \tag{A.115a}$$

$$\mathbf{f_G}_{z,z} = \left(\mathbf{f_{\bar{S}}} \oslash \bar{\mathbf{l}}\right) \odot \left(\bar{\mathbf{l}}_x^{②} \oslash \bar{\mathbf{l}}^{②}\right) \mathrm{d}r_z \tag{A.115b}$$

The reaction forces defined in equation (A.111) and (A.112) may now be expressed by

$$\mathbf{R_S}_{,x} = \begin{bmatrix} \mathbf{f_S}_{x,z} \bullet \mathbf{sgn_{S,x}} \\ \mathbf{f_S}_{z,z} \bullet \mathbf{sgn_{S,z}} \\ \mathbf{f_S}_{x,z} \bullet \mathbf{a_x} + \mathbf{f_S}_{z,z} \bullet \mathbf{a_z} \end{bmatrix} \tag{A.116}$$

$$\mathbf{R_G}_{,x} = \begin{bmatrix} \mathbf{f_G}_{x,z} \bullet \mathbf{sgn_{G,xz}} \\ \mathbf{f_G}_{z,z} \bullet \mathbf{sgn_{sum}} \\ (\mathbf{f_G}_{z,z} \odot \mathbf{a_z} - \mathbf{f_G}_{x,z} \odot \mathbf{a_x}) \bullet \mathbf{sgn_{S,z}} \end{bmatrix} \tag{A.117}$$

and equation A.110–A.113 may be reorganised to the form

$$\begin{bmatrix} R_{x,z} \\ R_{z,z} \\ R_{\theta,z} \end{bmatrix} = \begin{bmatrix} K_{xz} \\ K_{zz} \\ K_{\theta z} \end{bmatrix} \mathrm{d}r_z + \begin{bmatrix} P_x \\ P_z \\ P_\theta \end{bmatrix} \tag{A.118}$$

where the stiffness vector K_{mz} $(m = x, z, \theta)$ constitutes the second column of the stiffness matrix of the system. The force vector P_m contains the forces, including the weight of the section model, required to maintain the static displacement pattern. These forces are obviously equal to the static forces defined in (A.109).

A.1.4 Infinitesimal rotation

The effect of an infinitesimal rotation, shown in Figure A.58, is derived in the same manner as for a horizontal or vertical displacement, except that it gives rise to both horizontal and vertical displacements simultaneously. Because of this, a small change in rotation also changes the moment arm of the spring forces, which give rise to additional geometric moment stiffness.

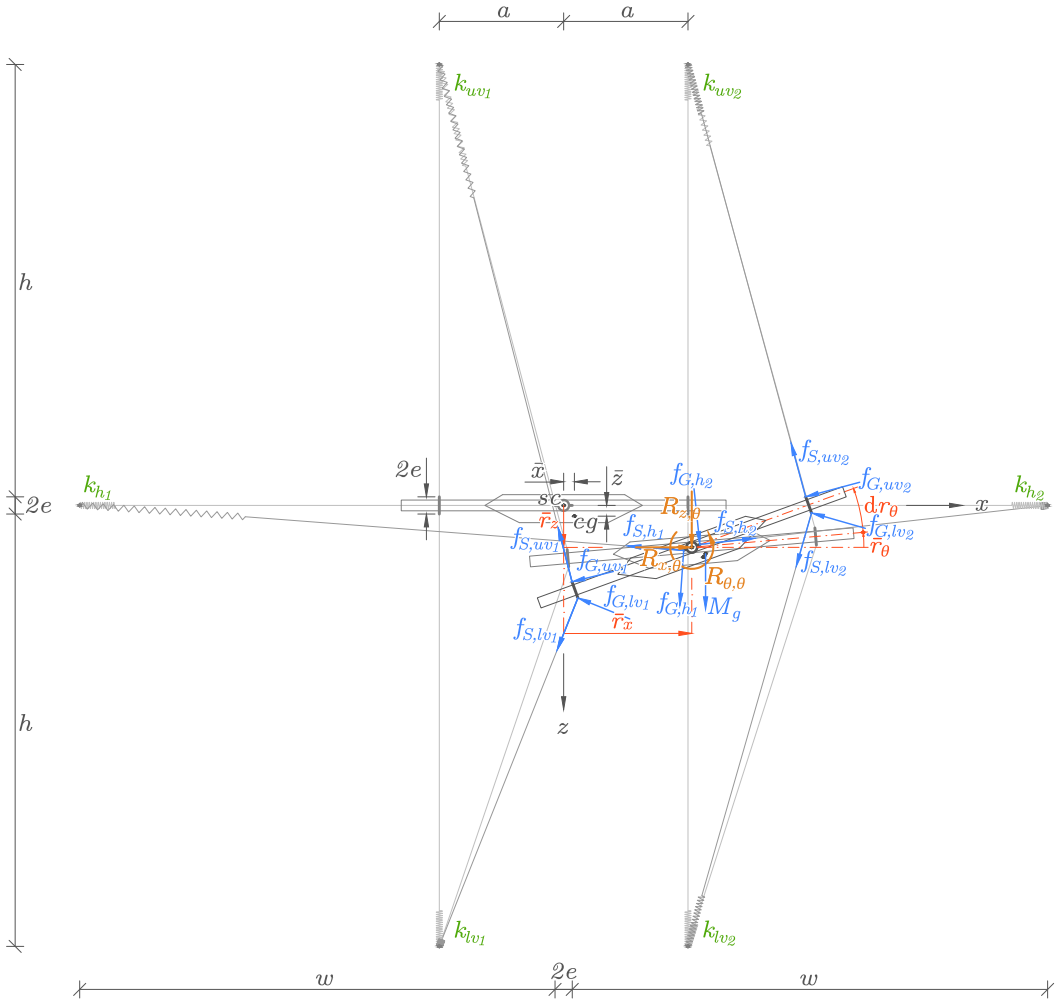

Figure A.58: Infinitesimal rotation (exaggerated).

As usual

$$\mathbf{R}_\theta = \begin{bmatrix} R_{x,\theta} \\ R_{z,\theta} \\ R_{\theta,\theta} \end{bmatrix} = \mathbf{R}_{\mathbf{S},\theta} + \mathbf{R}_{\mathbf{G},\theta} + \mathbf{R}_{\mathbf{M},\theta} \tag{A.119}$$

where

$$\mathbf{R}_{\mathbf{S},\theta} = \begin{bmatrix} f_{S,h_1,x} - f_{S,h_2,x} + f_{S,uv_1,x} + f_{S,uv_2,x} + f_{S,lv_1,x} + f_{S,lv_2,x} \\ f_{S,h_1,z} + f_{S,h_2,z} + f_{S,uv_1,z} + f_{S,uv_2,z} - f_{S,lv_1,z} - f_{S,lv_2,z} \\ (f_{S,h_1,x}+f_{S,h_2,x})\,(\bar{r}_\theta+\mathrm{d}r_\theta)\,e + (f_{S,h_1,z}-f_{S,h_2,z})\,e \\ +\,(f_{S,lv_1,x}-f_{S,uv_2,x})\,[(\bar{r}_\theta+\mathrm{d}r_\theta)\,a+e] + (f_{S,uv_1,x}-f_{S,lv_2,x})\,[(\bar{r}_\theta+\mathrm{d}r_\theta)\,a-e] \\ +\,(f_{S,uv_1,z}+f_{S,lv_2,z})\,[a+(\bar{r}_\theta+\mathrm{d}r_\theta)\,e] - (f_{S,uv_2,z}+f_{S,lv_1,z})\,[a-(\bar{r}_\theta+\mathrm{d}r_\theta)\,e] \end{bmatrix} \tag{A.120}$$

Unlike the other cases of infinitesimal displacements, the sign of the geometric stiffness induced by a small change of rotation is not equal to the sign of the change. Because a rotation gives rise to both horizontal and vertical displacements, it is highly dependent on the static displacements. It is, however, necessary to define positive directions, which is done in Figure A.58. This gives

$$\mathbf{R}_{\mathbf{G},\theta} = \begin{bmatrix} f_{G,h_1,x} - f_{G,h_2,x} + f_{G,uv_1,x} + f_{G,uv_2,x} + f_{G,lv_1,x} + f_{G,lv_2,x} \\ -f_{G,h_1,z} - f_{G,h_2,z} - f_{G,uv_1,z} - f_{G,uv_2,z} + f_{G,lv_1,z} + f_{G,lv_2,z} \\ (f_{G,h_1,x}+f_{G,h_2,x})\,(\bar{r}_\theta+\mathrm{d}r_\theta)\,e - (f_{G,h_1,z}-f_{G,h_2,z})\,e \\ +\,(f_{G,lv_1,x}-f_{G,uv_2,x})\,[(\bar{r}_\theta+\mathrm{d}r_\theta)\,a+e] + (f_{G,uv_1,x}-f_{G,lv_2,x})\,[(\bar{r}_\theta+\mathrm{d}r_\theta)\,a-e] \\ -\,(f_{G,uv_1,z}+f_{G,lv_2,z})\,[a+(\bar{r}_\theta+\mathrm{d}r_\theta)\,e] + (f_{G,uv_2,z}+f_{G,lv_1,z})\,[a-(\bar{r}_\theta+\mathrm{d}r_\theta)\,e] \end{bmatrix} \tag{A.121}$$

$$\mathbf{R}_{\mathbf{M},\theta} = \begin{bmatrix} 0 \\ -M_g \\ [\bar{x} + (\bar{r}_\theta + \mathrm{d}r_\theta)\,\bar{z}]\,M_g \end{bmatrix} \tag{A.122}$$

The forces acting on the rotation arm are now found by applying an infinitesimal horizontal and a vertical displacement successively:

$$\mathbf{f}_{\mathbf{S}x,\theta} = \mathbf{f}_{\bar{\mathbf{S}}} \odot \left(\bar{\mathbf{l}}_x \oslash \bar{\mathbf{l}}\right) + \mathbf{k} \odot \left(\bar{\mathbf{l}}_x \oslash \bar{\mathbf{l}}^{②}\right) \odot \left(\bar{\mathbf{l}}_x \odot \mathbf{a}_\mathbf{x} + \bar{\mathbf{l}}_z \odot \mathbf{a}_\mathbf{z}\right) \mathrm{d}r_\theta \tag{A.123a}$$

$$\mathbf{f}_{\mathbf{S}z,\theta} = \mathbf{f}_{\bar{\mathbf{S}}} \odot \left(\bar{\mathbf{l}}_z \oslash \bar{\mathbf{l}}\right) + \mathbf{k} \odot \left(\bar{\mathbf{l}}_z \oslash \bar{\mathbf{l}}^{②}\right) \odot \left(\bar{\mathbf{l}}_x \odot \mathbf{a}_\mathbf{x} + \bar{\mathbf{l}}_z \odot \mathbf{a}_\mathbf{z}\right) \mathrm{d}r_\theta \tag{A.123b}$$

and

$$\mathbf{f}_{\mathbf{G}x,\theta} = \left(\mathbf{f}_{\bar{\mathbf{S}}} \oslash \bar{\mathbf{l}}\right) \odot \left(\bar{\mathbf{l}}_z \oslash \bar{\mathbf{l}}^{②}\right) \odot \left(\bar{\mathbf{l}}_z \odot \mathbf{a}_\mathbf{x} - \bar{\mathbf{l}}_x \odot \mathbf{a}_\mathbf{z}\right) \mathrm{d}r_\theta \tag{A.124a}$$

$$\mathbf{f}_{\mathbf{G}z,\theta} = \left(\mathbf{f}_{\bar{\mathbf{S}}} \oslash \bar{\mathbf{l}}\right) \odot \left(\bar{\mathbf{l}}_x \oslash \bar{\mathbf{l}}^{②}\right) \odot \left(\bar{\mathbf{l}}_z \odot \mathbf{a}_\mathbf{x} - \bar{\mathbf{l}}_x \odot \mathbf{a}_\mathbf{z}\right) \mathrm{d}r_\theta \tag{A.124b}$$

By introducing

$$\mathbf{a}_{\mathbf{dr}_\boldsymbol{\theta},\mathbf{x}} = \begin{bmatrix} e \\ e \\ a \\ -a \\ a \\ -a \end{bmatrix} \mathrm{d}r_\theta \qquad \text{and} \qquad \mathbf{a}_{\mathbf{dr}_\boldsymbol{\theta},\mathbf{z}} = \begin{bmatrix} 0 \\ 0 \\ e \\ e \\ e \\ e \end{bmatrix} \mathrm{d}r_\theta \tag{A.125}$$

to include the change of rotation in moment equilibrium, the reaction forces defined in equation (A.120) and (A.121) may now be expressed by

$$\mathbf{R}_{\mathbf{S},\theta} = \begin{bmatrix} \mathbf{f}_{\mathbf{S}x,\theta} \bullet \mathbf{sgn}_{\mathbf{S},\mathbf{x}} \\ \mathbf{f}_{\mathbf{S}z,\theta} \bullet \mathbf{sgn}_{\mathbf{S},\mathbf{z}} \\ \mathbf{f}_{\mathbf{S}x,\theta} \bullet (\mathbf{a}_\mathbf{x} + \mathbf{a}_{\mathbf{dr}_\boldsymbol{\theta},\mathbf{x}}) + \mathbf{f}_{\mathbf{S}z,\theta} \bullet (\mathbf{a}_\mathbf{z} + \mathbf{a}_{\mathbf{dr}_\boldsymbol{\theta},\mathbf{z}}) \end{bmatrix} \tag{A.126}$$

$$\mathbf{R}_{\mathbf{G},\theta} = \begin{bmatrix} \mathbf{f}_{\mathbf{G}x,\theta} \bullet \mathbf{sgn}_{\mathbf{S,x}} \\ -\mathbf{f}_{\mathbf{G}z,\theta} \bullet \mathbf{sgn}_{\mathbf{S,z}} \\ (\mathbf{f}_{\mathbf{G}x,\theta} \odot \mathbf{a}_{\mathbf{x}} - \mathbf{f}_{\mathbf{G}z,\theta} \odot \mathbf{a}_{\mathbf{z}}) \bullet \mathbf{sgn}_{\mathbf{sum}} \end{bmatrix} \tag{A.127}$$

Changes in moment arms, $\mathbf{a}_{\mathbf{dr}_{\boldsymbol{\theta}},\mathbf{x}}$ and $\mathbf{a}_{\mathbf{dr}_{\boldsymbol{\theta}},\mathbf{z}}$, are not included in (A.127) because all higher order terms of $\mathrm{d}r_\theta$ are discarded.

Equation A.119–A.122 may now be reorganised to the form

$$\begin{bmatrix} R_{x,\theta} \\ R_{z,\theta} \\ R_{\theta,\theta} \end{bmatrix} = \begin{bmatrix} K_{x\theta} \\ K_{z\theta} \\ K_{\theta\theta} \end{bmatrix} \mathrm{d}r_\theta + \begin{bmatrix} P_x \\ P_z \\ P_\theta \end{bmatrix} \tag{A.128}$$

where the stiffness vector $K_{m\theta}$ $(m = x, z, \theta)$ constitutes the third column of the stiffness matrix of the system. The force vector P_m contains the forces, including the weight of the section model, required to maintain the static displacement pattern. These forces are, as mentioned in A.1.3, equal to the static forces defined in (A.109).

A.1.5 Simplified stiffness matrix

The expressions given above, may be utilised to assemble the stiffness matrix of the basic suspension system. Because of space considerations, an explicit assembly of the full stiffness matrix is not appropriate, but a simplified version may easily be derived. Assuming no static displacements,

$$\bar{r}_x = \bar{r}_z = \bar{r}_\theta = 0$$

no wire bracket or mass centre deviation

$$e = \bar{x} = \bar{z} = 0$$

and

$$\begin{aligned} k_h &= k_{h_1} = k_{h_2} \\ k_{uv} &= k_{uv_1} = k_{uv_2} \\ k_{lv} &= k_{lv_1} = k_{lv_2} \\ f_{S_0,h} &= f_{S_0,h_1} = f_{S_0,h_2} \\ f_{S_0,uv} &= f_{S_0,uv_1} = f_{S_0,uv_2} \\ f_{S_0,lv} &= f_{S_0,lv_1} = f_{S_0,lv_2} \end{aligned}$$

the stiffness matrix of each basic suspension system is found to be

$$\mathbf{K}_{\text{simplified}} = \begin{bmatrix} 2\left(k_h + \frac{f_{S_0,uv}+f_{S_0,lv}}{h}\right) & 0 & 0 \\ 0 & 2\left(k_{uv} + k_{lv} + \frac{f_{S_0,h}}{w}\right) & 0 \\ 0 & 0 & 2\left(k_{uv} + k_{lv}\right)a^2 \end{bmatrix} \tag{A.129}$$

A.2 Stiffness matrix of the full system

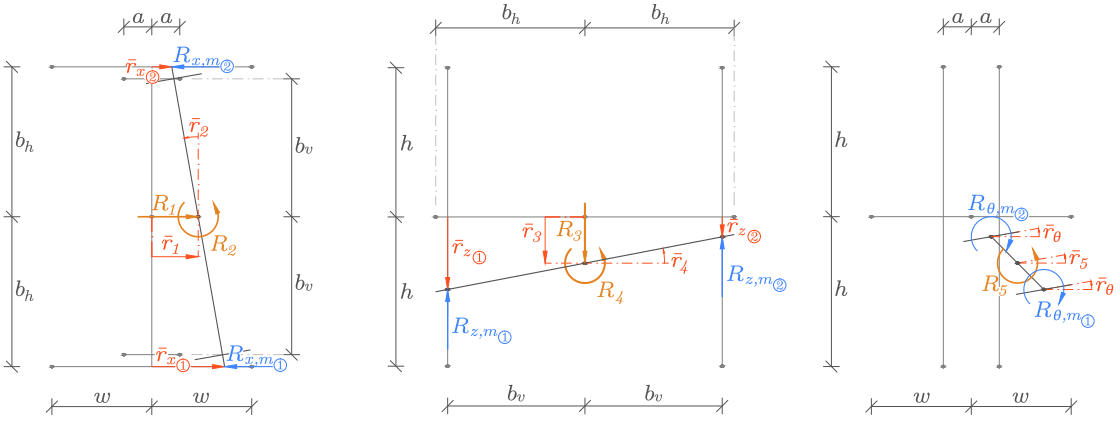

(a) Top view *(b)* Side view *(c)* Front view

Figure A.59: Kinematic relations between full system and subsystems.

The stiffness matrix of the full system may now be assembled based on the expressions derived above. Figure A.59 defines global degrees of freedom, $\bar{r}_i$, local degrees of freedom, $\bar{r}_{m_{①}}$, and reaction forces from the subsystems, $R_{m,n_{①}}$. The encircled subscript i indicates the subsystem, and the subscripts m and n represents directions, i.e. x, z or θ. The lengths b_h and b_v are the distance from the centre of gravity of the section model to the horizontal and vertical wire brackets, respectively.

The difference between b_h and b_v, combined with the rotations $\bar{r}_2$ and $\bar{r}_4$, give rise to small differences in displacements of the horizontal and vertical suspensions within each subsystem. It is assumed that these differences are small enough to justify the two-dimensional approximation made in A.1.

Assuming small rotations, kinematic relations governing the relationship between the two subsystems and the full system are readily derived from Figure A.59:

$$\mathbf{r}_{①} = \begin{bmatrix} \bar{r}_{x_{①}} \\ \bar{r}_{z_{①}} \\ \bar{r}_{\theta_{①}} \end{bmatrix} = \begin{bmatrix} \bar{r}_1 + \bar{r}_2 b_h \\ \bar{r}_3 + \bar{r}_4 b_v \\ \bar{r}_5 \end{bmatrix} \tag{A.130}$$

$$\mathbf{r}_{②} = \begin{bmatrix} \bar{r}_{x_{②}} \\ \bar{r}_{z_{②}} \\ \bar{r}_{\theta_{②}} \end{bmatrix} = \begin{bmatrix} \bar{r}_1 - \bar{r}_2 b_h \\ \bar{r}_3 - \bar{r}_4 b_v \\ \bar{r}_5 \end{bmatrix} \tag{A.131}$$

Next, the stiffness matrices of the two subsystems are established based on their respective static displacements:

$$\mathbf{K}_{①} = K(\mathbf{r}_{①}) \qquad \text{and} \qquad \mathbf{K}_{②} = K(\mathbf{r}_{②})$$

where $K(\mathbf{r})$ is the stiffness matrix derived in section A.1. For simplicity, the only parameter stated here is static displacement, although initial forces and spring stiffness may differ between the two systems. In the MATLAB function calculating the matrix, the small variations of these parameters have been included.

Since the stiffness is based on change in forces, a transformation matrix $\mathbf{T}$ may be established by mapping reaction forces from the subsystems to the full system:

$$\begin{bmatrix} R_1 \\ R_2 \\ R_3 \\ R_4 \\ R_5 \end{bmatrix} = \begin{bmatrix} 1 & 0 & 0 & 1 & 0 & 0 \\ b_h & 0 & 0 & -b_h & 0 & 0 \\ 0 & 1 & 0 & 0 & 1 & 0 \\ 0 & b_v & 0 & 0 & -b_v & 0 \\ 0 & 0 & 1 & 0 & 0 & 1 \end{bmatrix} \begin{bmatrix} R_{x,m_{①}} \\ R_{z,m_{①}} \\ R_{\theta,m_{①}} \\ R_{x,m_{②}} \\ R_{z,m_{②}} \\ R_{\theta,m_{②}} \end{bmatrix} = \mathbf{T} \begin{bmatrix} R_{x,m_{①}} \\ R_{z,m_{①}} \\ R_{\theta,m_{①}} \\ R_{x,m_{②}} \\ R_{z,m_{②}} \\ R_{\theta,m_{②}} \end{bmatrix} \tag{A.132}$$

where the subscript m represents the origin of the reaction force, i.e. type of displacement. The full stiffness matrix is then given by

$$\mathbf{K} = \mathbf{T} \begin{bmatrix} \mathbf{K}_{①} & \mathbf{0} \\ \mathbf{0} & \mathbf{K}_{②} \end{bmatrix} \mathbf{T}^{\mathrm{T}} \tag{A.133}$$

and the stiffness matrix derived in (A.129) gives rise to the simplified global matrix:

$$\mathbf{K}_{\text{simplified}} = \begin{bmatrix} K_{11} & 0 & 0 & 0 & 0 \\ 0 & K_{22} & 0 & 0 & 0 \\ 0 & 0 & K_{33} & 0 & 0 \\ 0 & 0 & 0 & K_{44} & 0 \\ 0 & 0 & 0 & 0 & K_{55} \end{bmatrix} \tag{A.134}$$

where

$$K_{11} = 4\left(k_h + \frac{f_{S_0,uv} + f_{S_0,lv}}{h}\right) \tag{A.135a}$$

$$K_{22} = K_{11} b_h^2 \tag{A.135b}$$

$$K_{33} = 4\left(k_{uv} + k_{lv} + \frac{f_{S_0,h}}{w}\right) \tag{A.135c}$$

$$K_{44} = K_{33} b_v^2 \tag{A.135d}$$

$$K_{55} = 4\left(k_{uv} + k_{lv}\right) a^2 \tag{A.135e}$$

Concluding remarks

The assumption of small rotations and two-dimensional subsystems may in some cases give poor results. Horizontal rotation, in particular, gives rise to displacements out of

the xy-plane of the subsystem, and the static forces in the suspensions lead to geometric moment stiffness, as seen in (A.126).

The length b_h should be considered carefully, since a major part of the horizontal stiffness is geometric stiffness due to tension in the vertical suspensions. It may be a better solution to replace b_h with an *effective* length, such that

$$b_v \leq b_{h,\text{eff}} \leq b_h$$

This length may be found from equilibrium, but it was observed that a mean value, $b_{h,\text{eff}} = (b_h + b_v)/2$, gave good results in the experimental setup described in this paper.

Appendix B: Monte Carlo simulation of a turbulent wind field

B.1 Simulation of spatially coherent time series

The theory presented in this section is based on [49].

To simulate the horizontal along-wind and the vertical across-wind turbulence components u and w of a turbulent wind field at N equidistant points along a line-like structure, it is important to capture the fact that these time series represents simultaneous events, and therefore, they must contain the appropriate spatial coherence properties.

Let $\mathbf{C}_{mn}(\tau)$ be the covariance matrix and $\mathbf{S}_{mn}(\omega)$ the corresponding cross spectral density matrix between two arbitrary points m and n, given by

$$\mathbf{S}_{mn}(\omega) = \begin{bmatrix} S_{uu}(\omega, \Delta s) & S_{uw}(\omega, \Delta s) \\ S_{wu}(\omega, \Delta s) & S_{ww}(\omega, \Delta s) \end{bmatrix} \tag{B.136}$$

where Δs is the spatial distance between m and n. An N by N cross spectral density block matrix may now be assembled:

$$\mathbf{S}(\omega) = \begin{bmatrix} \mathbf{S}_{11} & \cdots & \mathbf{S}_{1n} & \cdots & \mathbf{S}_{1N} \\ \vdots & \ddots & \vdots & \iddots & \vdots \\ \mathbf{S}_{m1} & \cdots & \mathbf{S}_{mn} & \cdots & \mathbf{S}_{mN} \\ \vdots & \iddots & \vdots & \ddots & \vdots \\ \mathbf{S}_{N1} & \cdots & \mathbf{S}_{Nn} & \cdots & \mathbf{S}_{NN} \end{bmatrix} \tag{B.137}$$

This matrix contains all the space and frequency domain information that is necessary for a time domain simulation with correct statistical properties for the turbulence components.

It is assumed that the turbulent wind field can be considered a stationary and homogeneous process, such that

$$\mathbf{C}_{mn}(\tau) = \mathbf{C}_{nm}(\tau) \qquad \text{and} \qquad \mathbf{S}_{mn}(\omega) = \mathbf{S}^*_{nm}(\omega)$$

This implies that $\mathbf{S}$ is Hermitian and non-negative definite. A Cholesky decomposition of $\mathbf{S}$ will then render a lower triangular matrix

$$\mathbf{G}(\omega) = \begin{bmatrix} G_{11} & \cdots & 0 & \cdots & 0 \\ \vdots & \ddots & \vdots & \iddots & \vdots \\ G_{i1} & \cdots & G_{ij} & \cdots & 0 \\ \vdots & \iddots & \vdots & \ddots & \vdots \\ G_{(2N)1} & \cdots & G_{(2N)j} & \cdots & G_{(2N)(2N)} \end{bmatrix} \tag{B.138}$$

whose properties are such that

$$\mathbf{S}(\omega) = \mathbf{G}(\mathbf{G}^*)^{\mathrm{T}} \tag{B.139}$$

Assuming a frequency segmentation of M equidistant points, the simulated time series

$$x_i(t) = \sqrt{2\Delta\omega} \cdot \sum_{j=1}^{i} \sum_{k=1}^{M} |G_{ij}(\omega_k)| \cos(\omega_k t + \psi_{jk}) \tag{B.140}$$

where $i = 1, 2, \ldots, 2N$, k is the frequency segment number and ψ_{jk} is an arbitrary phase angle between zero and 2π, contains the turbulence components at $m = 1, 2, \ldots, N$:

$$u_m(t) = x_{2m-1}(t) \tag{B.141a}$$

$$w_m(t) = x_{2m}(t) \tag{B.141b}$$

B.2 Representative turbulence characteristics

Even though the wind tunnel described in [50] differs from the one at NTNU, turbulence characteristics of the wind field generated in the tunnel have been used to simulate a wind field for FEM-analysis in the present work.

Approximate turbulence intensities are given in Table B.23. Cross spectral densities are described in the following. For simplicity, it is in the following assumed that cross spectra between the u and w components are negligible, such that

$$S_{uw}(\omega, \Delta s) \approx 0 \tag{B.142}$$

where Δs is the spatial separation along the line-like structure.

In most cases of a homogeneous wind field,

$$S_{nn}(\omega, \Delta s) = S_n(\omega) \cdot \hat{C}o_{nn}(\omega, \Delta s) \tag{B.143}$$

where n is a turbulence component (u or w), S_n is the single point spectral density and $\hat{C}o_{nn}$ is the normalised co-spectrum. According to [50], the normalised co-spectra of the wind tunnel used for section model tests of the Hardanger Bridge was approximated by

$$\hat{C}o_{nn}(\omega, \Delta s) = \left(1 - \frac{1}{2}\kappa_n \Delta s L_{exp} \frac{C_n}{2\pi}\right) \exp\left(-\kappa_n \Delta s L_{exp} \frac{C_n}{2\pi}\right) \tag{B.144}$$

where L_{exp} is the length of the wind exposed part of the section model, which for most cases equals the width of the wind tunnel, and

$$\kappa_n(\omega) = \sqrt{\left(\frac{\omega}{V}\right)^2 + \left(\frac{1}{L_n}\right)^2} \tag{B.145}$$

Estimates of the parameters C_n and L_n are given in Table B.23.

The reduced auto spectra was not provided explicitly in [50], but they have been resembled by *Kaimal auto spectra*, defined by

$$\frac{f \cdot S_n(f)}{\sigma_n^2} = \frac{A_n \hat{f}_n}{\left(1 + 1.5 A_n \hat{f}_n\right)^{5/3}} \tag{B.146}$$

where the reduced frequency is defined by $\hat{f}_n = f \cdot {}^sL_n / V$ and ${}^sL_n$ is the integral length scale of the relevant turbulence component. Approximated values of the parameter A_n are given in Table B.23. The auto-spectra and co-spectra are shown in Figure B.60.

Flow property	A_u	A_w	L_u (m)	L_w (m)	C_u	C_w
Parameter value	19	3	1.2	0.2	5.5	2.4

Table B.23: Estimated parameters for determination of turbulence properties.

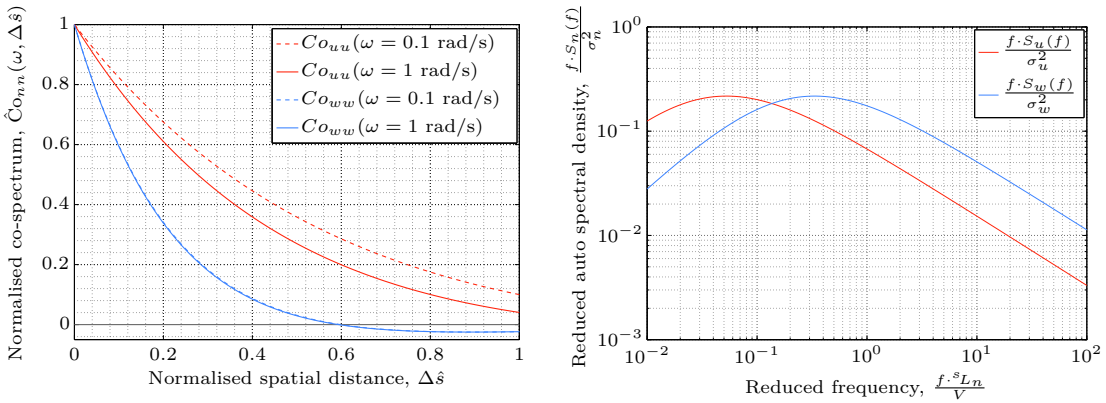

(a) Normalised co-spectra

(b) Reduced auto spectra

Figure B.60: Turbulence characteristics applied in simulations.

Appendix C: Abaqus/CAE model

The FE-model developed in Abaqus/CAE was an important part of the design process of the suspension rig presented in this thesis. It proved to be a good representation of the prototype, although differences were observed when investigating excitation amplitude effects. The model is essentially undamped; only high-frequency α-damping to avoid numerical instabilities is incorporated.

The complete FE-model is shown in Figure C.61. Details of it's most important features will be discussed in the following.

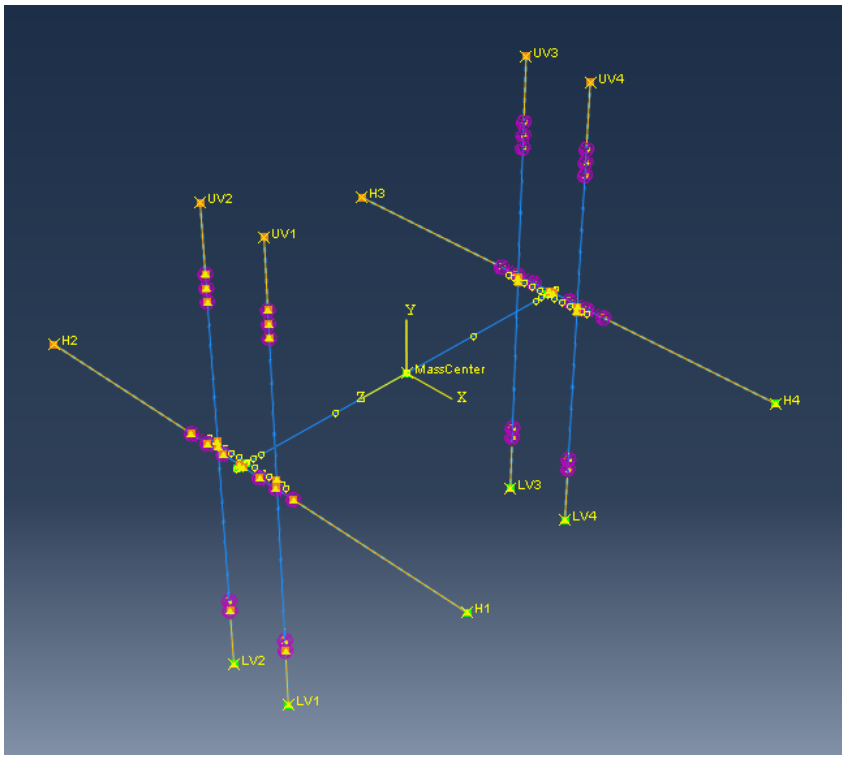

Figure C.61: FE-model in Abaqus/CAE.

C.1 Section model

The section model, including extension and rotation arms, is modelled by beam elements and defined as a rigid body through a "Rigid Body"-constraint. Hence, number of degrees of freedom is minimised, improving simulation speeds dramatically.

C.2 Suspension system

The part named "Suspension", illustrated in Figure C.62a is the main part of the FE-model. It contains all information about the experimental configuration, e.g. spring lengths, pretension lengths, wire brackets, additional weights etc., and it is crucial that it matches reality as close as possible. To simplify the process of reconfiguring the model for a new setup, all sketches have been parametrised as illustrated in Figure C.62. Most of the parameters must be provided by the user, but wire lengths are computed automatically.

It is important that the pretension length parameters matches that specified on the boundary conditions, which are the actual pretension that will be applied to each spring. If not, the final height and/or width of the model will differ from the specified values. To ensure that the section model maintain it's position during the pretension step of the simulation, it is also important that "UpperPretensionLength" is estimated correctly.

C.3 Mass and moment of inertia

Mass and moment of inertia is introduced through "Inertia"-assignments to relevant nodes. It is also simple to model extra weights on the rotation arm, even though it was not done on the prototype. Relevant values are calculated in an Microsoft Excel spreadsheet provided with the Abaqus/CAE model file.

C.4 Springs

To allow springs to be a part of the parametrised sketches, massless dummy truss elements with negligible stiffness defines the spring positions. Spring behaviour is modelled with special spring elements, positioned on top of the dummy trusses, giving constant stiffness regardless of deflection. Spring elements are coloured purple in Figure C.61.

To introduce mass and constant force to the springs, so-called "Slip Ring"-connectors have been utilised. It allows material to flow through nodes, i.e. it allows modelling of a wire with infinite axial stiffness (but no bending stiffness) that follows a path of nodes,

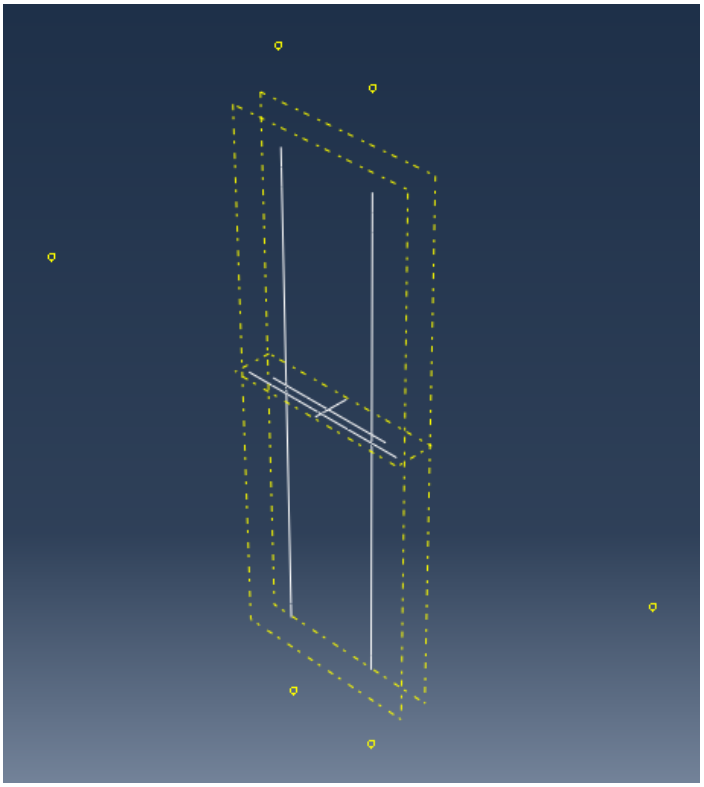

(a) Full suspension subsystem

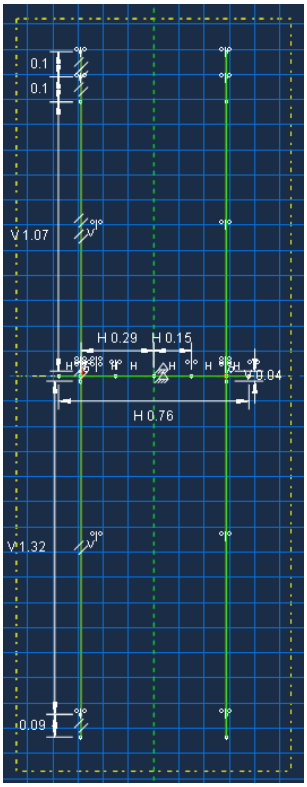

(b) Vertical sketch

Parameter Manager

Name	Current Value	Expression
RigHeight	3.05	3.050
UpperPretensionLength	235.E-03	0.235
LowerPretensionLength	90.E-03	0.090
WeightPosition	150.E-03	0.150
SuspensionPosition	288.E-03	0.288
UpperSpringLength1	100.E-03	0.100
UpperSpringLength2	100.E-03	0.100
LowerSpringLength	90.E-03	0.090
WireBracketDiameter	40.E-03	0.040
UpperWireLength	1.07	(RigHeight-WireBracketDiameter)/2-UpperPretensionLength-UpperSpringLength1-UpperSpringLength2
LowerWireLength	1.325	(RigHeight-WireBracketDiameter)/2-LowerPretensionLength-LowerSpringLength
ArmLength	755.E-03	0.755

Dimension... Insert Before Insert After Move Up Move Down Delete

Expression Builder...

OK Apply Cancel

(c) Parameters of the vertical sketch

Figure C.62: Parametrised sketch of the suspension system.

where each node can be considered a pulley. Hence, displacement and tension force can be transmitted from one end to the other along this path.
Mass and initial force of a spring can now be assigned to an auxiliary datum point a distance away from a fixed spring node. The fixed node represents the attachment point on the rig frame. The auxiliary datum points are shown in Figure C.61 and C.62a; in the former they are also labelled. The force must be oriented such that the fixed node lies in the extension of the force vector. By attaching a "Slip Ring"-connector to the rotation arm and letting it follow a path defined by the wire and spring elements of the suspension before it is attached to the auxiliary node, the motion of the auxiliary node will equal that at the end of the spring – but the direction of motion is independent of the spring direction. Thus, the constant force will always follow the direction of the suspension, and the mass will be accelerated with the acceleration experienced at the end of the spring. Connectors are represented by yellow and orange dashed lines in Figure C.61, although they are not visible behind the suspensions.

Pretensioning of springs is introduced by altering boundary conditions in the first step of the simulation. The "fixed" nodes are moved a distance (equivalent to the corresponding pretension length) further away from the section model. This is illustrated in Figure C.63. Since the springs have no lateral stiffness before they are pretensioned, they have to be supported laterally during this step.

C.5 Wire

The section model is connected to the springs through truss elements that represents the wires in the suspension rig. Since the wires always are in tension, and thereby stays

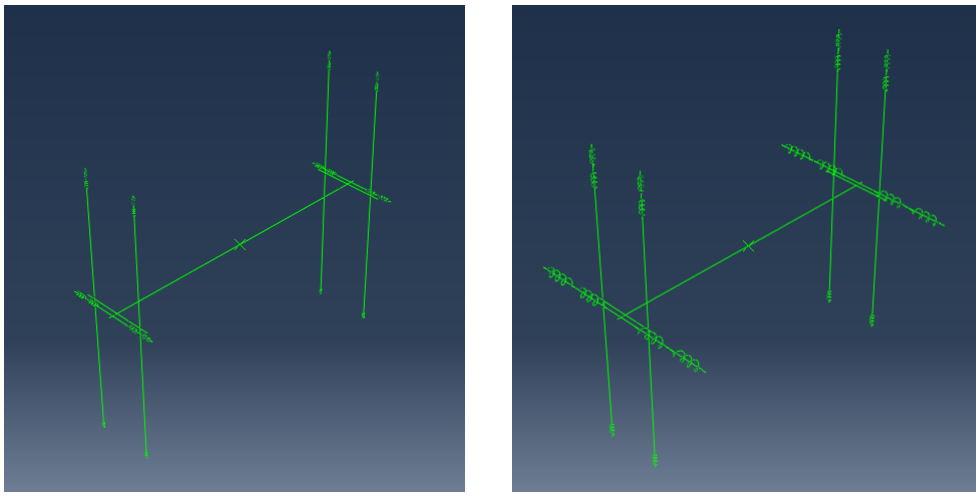

(a) Before pretensioning *(b)* After pretensioning

Figure C.63: Pretensioning of springs.

straight, each wire is modelled by a single truss element. Section and material definitions of the element are defined to match the stiffness properties of the elastic wire.

C.6 Loads

Static loads, e.g. due to mean wind acting on the section model, are applied to the reference node at the mass centre, which is assumed to lie on the torsional rotation axis.

Fluctuating wind loads are calculated in MATLAB, based on a Monte Carlo simulated wind field, and applied to the FE-model through "Equally Spaced"-type amplitudes, where tabular data is loaded from delimited text files generated by MATLAB.

C.7 Simulation steps

The following steps are defined in the model:

Pretension Boundary conditions are altered to pretension the springs. Gravitation is applied to the system.

ReleaseSpringSupport The lateral spring supports, that were necessary during pretensioning, are deactivated.

MeanWind Possible static force components are introduced to the section model.

Frequencies Natural frequencies of the system (after static displacements have been introduced) are computed by considering the eigenvalue problem.

FreeVibrationSetup The section model is forced into the desired initial configuration for free vibration response simulation.

FreeVibration[1] Forced displacements are released, and free vibration response is simulated by an implicit dynamic method.

DynamicWindLoad[1] Dynamic response to the fluctuating wind load components (and possibly initial displacements) is simulated by an implicit dynamic method.

[1] "FreeVibration" and "DynamicWindLoad" should not be enabled simultaneously.